UNIVERSITÀ
DEGLI STUDI
DI PADOVA

Sede Amministrativa: Università degli Studi di Padova

Dipartimento di Scienze Chimiche

CORSO DI DOTTORATO DI RICERCA IN: Scienze Molecolari
CURRICOLO: Scienze Chimiche
CICLO XXIX

MOLECULAR SYSTEMS AND INORGANIC MATERIALS FOR LIGHT-ACTIVATED APPLICATIONS

Coordinatore: Ch.mo Prof. Antonino Polimeno

Supervisore: Ch.ma Prof.ssa Lidia Armelao

Dottorando: Federica Mian

Riassunto

Il presente lavoro di tesi riguarda la sintesi, la caratterizzazione e lo studio delle proprietà attivate dalla luce (fotodegradazione, luminescenza persistente, *sensing*) di diversi materiali inorganici e di sistemi molecolari.

Nella prima parte, viene presentato lo studio di materiali bifunzionali a base di bismuto per l'adsorbimento e la fotodegradazione di coloranti organici. Vengono discusse nuove procedure per la sintesi di nanostrutture di ossicloruri (BiOCl, $Bi_{24}O_{31}Cl_{10}$, $Bi_{12}O_{17}Cl_2$) e subcarbonato di bismuto. Modulando i parametri di sintesi (temperatura, pH, surfattante) ed utilizzando diversi trattamenti (termici e irraggiamento UV) sul materiale ottenuto, è stato possibile indurre una variazione della composizione chimica e conseguentemente della fase cristallina, della morfologia e delle proprietà ottiche. Ciò ha determinato proprietà adsorbenti e attività di fotodegradazione diverse nei confronti di due coloranti modello: metilarancio e rodamina B. Le nanostrutture più promettenti, a base $(BiO)_2CO_3$, sono in grado di adsorbire entrambi i coloranti, tra il 50 e il 95 %, nell'arco di 20 minuti. Inoltre, sotto irraggiamento con luce visibile sono in grado di foto-degradare il colorante rimanente in soluzione.

La seconda parte riguarda lo studio di nanostrutture di gallato di zinco drogato con cromo ($ZnGa_2O_4:Cr^{3+}$). Questo materiale è caratterizzato da interessanti proprietà di emissione nella regione del rosso-vicino infrarosso (600-900 nm) e, in particolare, da luminescenza persistente. Mediante tecnica sol-gel e trattamenti termici compresi tra 500 e 1000 °C, sono stati preparati film sottili omogenei in termini di composizione, struttura e spessore. Essi sono stati caratterizzati mediante diffrazione a raggi X (XRD), spettroscopia fotoelettronica a raggi X (XPS), microscopia a scansione elettronica (SEM) e spettroscopia ottica (assorbimento ed emissione). In un intervallo di temperature compreso tra i -190°C e i 250 °C, si è osservata una modulazione delle proprietà di emissione, indicando la possibilità di utilizzare in futuro questi materiali per lo sviluppo di

sensori di temperatura. Per ottenere informazioni sito-specifiche e correlare le proprietà di luminescenza a quelle strutturali a corto raggio sono state impiegate tecniche avanzate di luce di sincrotrone quali X-Ray Absorption Spectroscopy (XAS) e X-Ray Excited Optical Luminescence (XEOL).
I materiali inorganici possono inoltre essere impiegati come substrati o matrici per ospitare molecole funzionali. Accanto allo sviluppo del sistema inorganico, è fondamentale uno studio preliminare del sistema molecolare stesso, in termini di stabilità cinetica e termodinamica, topologia, funzionalità e reattività. In questo contesto, la terza parte del presente lavoro descrive lo studio di due complessi antenna lantanoidei luminescenti caratterizzati da un legante macrociclico (1,4,7,10-tetraazaciclododecano-1,4,7-acido triacetico, DO3A) per il disprosio ed uno aciclico (1,4,7-triazaeptano-1,1,7,7-acido tetraacetico, DTTA) per l'europio. Il comportamento della coppia in soluzione acquosa è stato studiato in presenza di acido dipicolinico (DPA). In particolare, è stato considerato l'effetto di un agente fortemente coordinante come il DPA sulle loro proprietà di emissione e la possibilità di sviluppare un sensore raziometrico per piccole molecole come il DPA. A questo scopo, il complesso di disprosio è stato utilizzato come riferimento e quello di europio come sonda per il riconoscimento di DPA che è un noto biomarker di spore batteriche. La variazione delle proprietà di emissione (forma ed intensità delle bande) ha messo in luce la presenza di interazioni tra il complesso sonda e l'acido dipicolinico. Con l'ausilio della risonanza magnetica nucleare (NMR) e con la spettrometria di massa è stato evidenziato l'instaurarsi di una reazione di scambio di leganti, con la formazione di $[EuDPA_2]^-$. Ciò indica che leganti macrociclici, dotati di una cavità preformata in grado di ospitare lo ione metallico, assicurano una maggior stabilità rispetto a leganti aciclici caratterizzati dallo stesso numero e tipologia di siti di coordinazione.

PAROLE CHIAVE: materiali funzionali, processi di chimica soft in soluzione, adsorbimento e fotodegradazione di coloranti, materiali a luminescenza persistente, complessi antenna lantanoidei.

Abstract

The present work concerns the synthesis, the characterization and the study of the light-activated properties (photodegradation, persistent luminescence, sensing) of different inorganic materials and molecular systems.

In the first part, the realization of bismuth-based bifunctional materials for the adsorption and photodegradation of organic dyes is presented. Novel procedures for the synthesis of bismuth oxychlorides (BiOCl, $Bi_{24}O_{31}Cl_{10}$, $Bi_{12}O_{17}Cl_2$) and subcarbonate nanostructures are discussed. By modulating the synthesis parameters (temperature, pH and surfactant) and by means of different treatments (thermal and UV irradiation), a tuning of the chemical composition and consequently of the crystalline phase, morphology and optical properties was obtained. This was reflected in different absorbent properties and photo-degradation activity towards two model dyes: methyl orange and rhodamine B. The most promising nanostructures, based on $(BiO)_2CO_3$, are able to adsorb both dyes, from 50 up to 95 %, within 20 minutes. Further, under irradiation with visible light they are able to degrade the dye remained in solution.

The second part concerns the study of chromium doped zinc gallate ($ZnGa_2O_4:Cr^{3+}$) nanostructures. This material displays interesting emission properties in the red-NIR region (600-900 nm) and, especially, persistent luminescence. Adopting a sol-gel procedure and post-synthesis treatments in the range 500-1000 °C, thin films endowed with homogeneous composition, structure and thickness were obtained. These systems were characterized by means of X-ray diffraction (XRD), X-ray photoelectron spectroscopy (XPS), scanning electron microscopy (SEM) and optical spectroscopy (absorption and emission). A modulation of the emission properties was observed in a wide temperature range from -190 up to 250 °C, evidencing the possibility to employ these materials for the development of temperature sensors. Advanced synchrotron radiation techniques as X-Ray Absorption Spectroscopy (XAS) and X-Ray

Excited Optical Luminescence (XEOL) were adopted to get site-specific information and to correlate short-range order to luminescent properties.

Lastly, inorganic materials are also employed as substrates and/or hosting matrices for functional molecules. Besides the development of the inorganic system, the study of the molecular unit itself in terms of thermodynamic and kinetic stability, topology, functionality and reactivity is crucial. In this framework, the third part of the thesis describes the study of two lanthanide luminescent antenna complexes characterized by a macrocyclic ligand (1,4,7,10-tetraazacyclododecane-1,4,7-triacetic acid, DO3A) for dysprosium and an acyclic (1,4,7-triazaheptane-1,1,7,7-tetraacetic acid, DTTA) one for europium. The behavior of the couple in aqueous solution was studied in presence of dipicolinic acid (pyridine-2,6-dicarboxylic acid, DPA). In particular, it was investigated the effect of a strongly coordinating agent like DPA on their emission properties and the possibility to develop a ratiometric sensor for small molecules like DPA. To this aim, the dysprosium complex was employed as reference and the europium one as probe for the recognition of DPA which is known as a biomarker for bacterial spores. The modulation of the emission properties (band profile and relative intensity) revealed an interaction between probe complex and dipicolinic acid. NMR and mass spectrometry measurements evidenced that a ligand exchange reaction occurred, with the formation of $[EuDPA_2]^-$. This indicates that macrocyclic ligands endowed with a preformed cavity hosting the metal ion insure a better stability over acyclic ligands having the same number and typology of coordination sites. These findings provide crucial information for the future development of solid state sensors, realized by grafting suitable complexes on appropriate solid matrices.

KEYWORDS: *functional materials, soft-chemistry solution processes, adsorption and photodegradation of dyes, persistent luminescence materials, lanthanide antenna complexes*.

Index

List of Acronyms

AMW	Average Molecular Weight
BE	Binding Energy
CT	Charge Transfer
DO3A	1,4,7,10-Tetraazacyclododecane-1,4,7-Triacetic Acid
DPA	Dipicolinic Acid, Pyridine-2,6-Dicarboxylic Acid
DTTA	1,4,7-Triazaheptane-1,1,7,7-Tetraacetic Acid
FED	Field Emission Display
FE-SEM	Field Enhanced Scanning Electron Microscopy
FLY	Fluorescence Yield
JCPDS	Joint Committee on Powder Diffraction Standards
MO	Methyl Orange
NIR	Near Infrared
NMR	Nuclear Magnetic Resonance
P123	Pluronic 123
PEG	Polyethylenglycol
PFY	Partial Fluorescence Yield
RhB	Rhodamine B
SEM	Scanning Electron Microscopy
TFED	Thin Film Electroluminescent Device

TGA	Thermogravimetric Analysis
TSL	Thermally Stimulated Luminescence
XANES	X-Ray Absorption Near-Edge Spectroscopy
XAS	X-Ray Absorption Spectroscopy
XEOL	X-Ray Excited Optical Luminescence
XPS	X-Ray Photoelectron Spectroscopy
XRD	X-Ray Diffraction

Chapter 1. Molecular systems and inorganic materials for light-activated applications

1.1 Introduction

Interaction between light and matter represents one of the most powerful tools available to scientists for the study of molecular systems and materials within the broad horizon of nanoscience. Depending on the energy of the light source and the different interaction with matter, information on structure, composition, morphology and optical properties are obtained from the macro down to the nanoscale. Moreover, it is possible to achieve not only a deep knowledge on the intrinsic chemico-physical properties of the system under investigation but also information of its functional properties and its behavior towards the surrounding environment.[1-3] This paves the way to innovative studies in different fields of application including environmental remediation strategies, light conversion technologies and development of sensing tools.[4-8]

Besides, the rapid and continuous evolution of scientific progress in the last decade is directly dependent on the availability of functional materials endowed with specific properties. In different technological fields, the development of innovation processes and ever increasing demand of advanced performances rely on the possibility to design and fabricate materials with improved functional characteristics. In this regard, a great challenge is represented by the development of soft-chemistry solution processes for the realization of materials with a fine control of composition, microstructure and dispersion of functional species.[9] In this framework, three main research topics were developed in the present work concerning the study of inorganic materials and functional molecules designed for innovative light-activated applications. In the following section, the arrangement of thesis is presented and the main results are summarized.

1.2 Summary

In the first part, bismuth oxychlorides and subcarbonate-based nanostructures were investigated as potential multifunctional materials to be employed in the field of environmental remediation technologies as pollutants adsorbents endowed with photo-degradation activity under visible irradiation.

By modulating the synthesis conditions and post-synthesis thermal treatments, it was possible to obtain a tuning of chemical composition, nano and micro-structural organization and optical absorption properties. In particular, two synthesis procedures were developed which mainly differed for the pH of the precursor solution. Neutral conditions allowed to get BiOCl nanostructures and by means of successive thermal treatments $Bi_{24}O_{31}Cl_{10}$ was obtained as secondary crystalline phase. By a proper choice of annealing conditions, a composition tailoring of the BiOCl/$Bi_{24}O_{31}Cl_{10}$ composite material was achieved. On the other hand, through alkaline conditions copresence of $Bi_{12}O_{17}Cl_2$ and $(BiO)_2CO_3$ was obtained. Low temperature thermal treatments under different atmospheres and UV processing were employed to obtain a set of inorganic nanostructures, whose composition ranged from pure $Bi_{12}O_{17}Cl_2$ to $(BiO)_2CO_3$, with intermediate composites. Extended characterization by means of X-ray Diffraction (XRD), Scanning Electron Microscopy (SEM), X-ray Photoelectron Spectroscopy (XPS), absorption and Raman spectroscopy was conducted for the whole set of nanostructures. Moreover, their adsorption and photocatalytic performances were evaluated against two organic dyes: methyl orange (MO) and rhodamine B (RhB). The most promising performances were observed for $(BiO)_2CO_3$ nanostructures which were able to adsorb 50 % of RhB and 95 % of MO in 30 minutes and to catalyze the degradation of the remaining dye under visible irradiation in 180 minutes (Fig. 1.1).

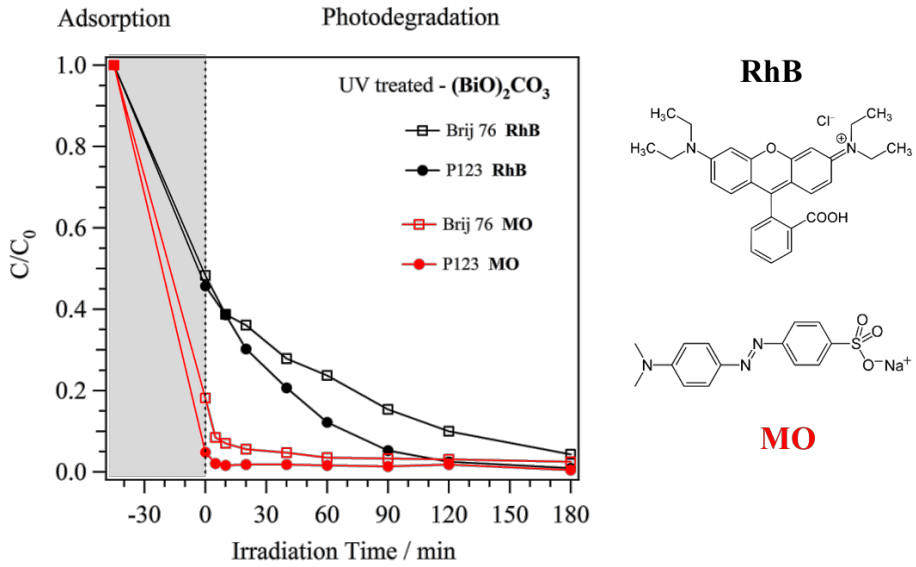

Fig. 1.1 $(BiO)_2CO_3$ nanostructures: adsorption and photocatalytic degradation of MO and RhB under visible irradiation. Note the high adsorption of MO and the complete photo-degradation of both dyes.

In the second part, the development of thin films characterized by peculiar luminescent properties was investigated. Cr^{3+} doped zinc gallate ($ZnGa_2O_4$) is a wide band gap (4.5-5 eV) semiconductor characterized by normal spinel structure. In the field of oxide-based phosphors, this material has recently grown increasing interest for its long-lasting luminescent properties, opening new opportunities for its employment in night/dark environment vision displays and for in vivo optical imaging. $ZnGa_2O_4:Cr^{3+}$ represents a promising solution to obtain a red/near-infrared persistent emission where the presence of peculiar lattice defects is fundamental to get trapped free carriers, their subsequent slow detrapping and finally their radiative recombination.[3] The present study concerned the development of $ZnGa_2O_4:Cr^{3+}$ thin films through sol-gel synthesis. Microstructural, morphological, compositional and optical properties (absorption and emission) were investigated by means of XRD, SEM, XPS and optical spectroscopy, together with synchrotron radiation techniques as X-ray Absorption Spectroscopy (XAS) and X-ray Excited Optical Luminescence (XEOL). The developed synthesis procedure allowed the formation of thin films constituted

mainly by the $ZnGa_2O_4$ crystalline phase. The films were characterized by homogeneous composition and regular thickness (Fig.1.2).

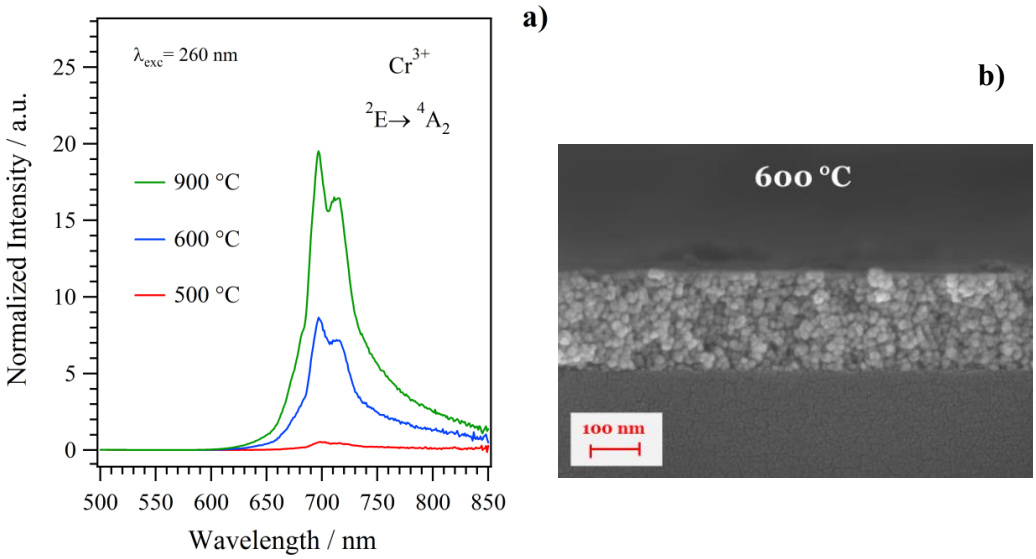

Fig. 1.2 a) Effect of thermal treatments on emission spectra; **b)** cross section SEM image of a film treated at 600 °C. Note the strong influence of the treatment temperature on emission and the homogeneous distribution of grains across the film thickness.

Thermal treatments at increasing temperature induced substantial modulation of composition, morphology and microstructure, leading to a red/NIR luminescent emission that persists up to several seconds after excitation through CT bands (Fig. 1.2). Moreover, $ZnGa_2O_4:Cr^{3+}$ thin films displayed emitting properties which were strongly influenced by temperature in a wide range of values, *i.e.* from -190 up to 250 °C. These findings point out the effectiveness of these materials to act as luminescence thermometer, thus opening further perspectives for future investigations.

Finally, inorganic materials may be also employed as substrates and/or hosting matrices for functional molecules. In this context, besides the development of the inorganic material, an essential step concerns the preliminary study and characterization of the molecular system endowed with the functionality of interest. In fact, an accurate knowledge of the nature and behaviour of the functional unit itself, in terms of thermodynamic and kinetic stability, topology, functionality and reactivity, is crucial for a complete comprehension and design of

the final composite material. In this framework, the last section concerned the study of two luminescent lanthanide antenna complexes ($Eu^{3+}\subset$**1**, $Dy^{3+}\subset$**9**) characterized by different ligand topology. Their behavior in presence of dipicolinic acid (DPA, pyridine-2,6-dicarboxylic acid) was investigated in order to study the effect of strongly coordinating agents like DPA on their emission properties. To do this, the possibility to develop a ratiometric sensor for small molecules like DPA was considered. Macrocyclic (1,4,7,10-tetraazacyclododecane-1,4,7-triacetic acid, DO3A, **9**) and acyclic (1,4,7-triazaheptane-1,1,7,7-tetraacetic acid, DTTA, **1**) ligands were selected in order to form a ratiometric pair in which $Dy^{3+}\subset$**9** acts as reference and $Eu^{3+}\subset$**1** as probe for the recognition of DPA (Fig. 1.3).

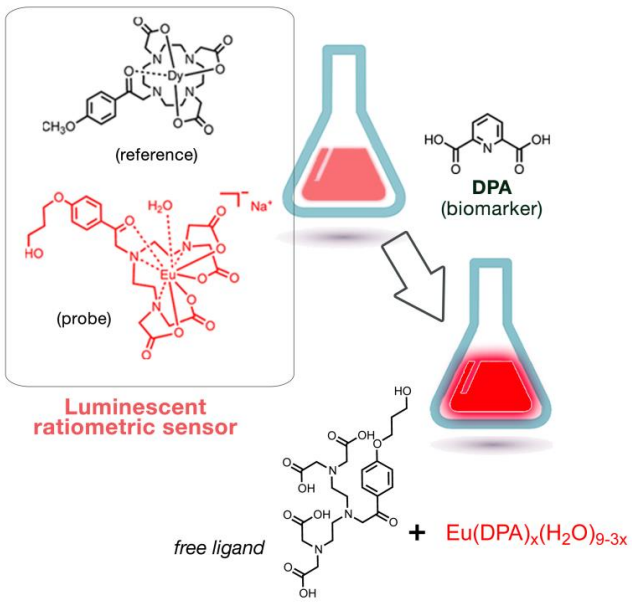

Fig. 1.3 Behavior of the ratiometric sensor $Eu^{3+}\subset$1, $Dy^{3+}\subset$9 in presence of DPA.

Dipicolinic acid is the main structural component of the protective outer layers of bacterial spores, *e.g*. *Bacillus Anthracis* (approximately 5-15% of the dry mass), and the development of fast and reliable sensor systems capable of detecting this endospores biomarker has attracted considerable interest. The change of emission intensity of Eu^{3+} indicated the occurrence of a new sensitization path for the lanthanide cation through excitation of DPA. NMR and mass spectrometry

measurements showed that this phenomenon was ascribed to a ligand exchange reaction with the formation of emitting $[EuDPA_2]^-$. These results evidenced the importance of the different topology of the employed ligands in the stability and inertness of the complexes. In particular, macrocyclic ligands that have a preformed cavity in which the metal ions can be hosted insure a better stability over acyclic ligands having the same number and typology of coordination sites.

1.3 References

(1) Rohit P., P.; Antonette J., T. *Optical techniques for Solid-State Materials Characterization*, 2011.

(2) Bléger, D.; Hecht, S. *Angewandte Chemie International Edition* **2015**, *54*, 11338.

(3) Mobilio, S.; Boscherini, F.; Meneghini, C. *Synchrotron Radiation - Basics, Methods and Applications*; Springer, 2015.

(4) Cheng, H.; Huang, B.; Dai, Y. *Nanoscale* **2014**, *6*, 2009.

(5) Huang, X.; Han, S.; Huang, W.; Liu, X. *Chemical Society Reviews* **2013**, *42*, 173.

(6) Feldmann, C.; Jüstel, T.; Ronda, C. R.; Schmidt, P. J. *Advanced Functional Materials* **2003**, *13*, 511.

(7) Zhuang, Y.; Katayama, Y.; Ueda, J.; Tanabe, S. *Optical Materials* **2014**, *36*, 1907.

(8) Butler, S. J.; Parker, D. *Chemical Society Reviews* **2013**, *42*, 1652.

(9) Danks, A. E.; Hall, S. R.; Schnepp, Z. *Materials Horizons* **2016**, *3*, 91.

Chapter 2. Bismuth oxychlorides and subcarbonate as bifunctional materials

2.1 Introduction

The interest toward multifunctional materials has continuously increased over last few years, in different fields of application. Concerning environmental remediation strategies, materials able to act simultaneously as pollutant adsorbents and to degrade contaminants are highly desirable, even though their synthesis is still challenging because of the specific and non-trivial requirements that have to be fulfilled. Among the most widespread pollutants, dyes represent a considerable portion since they are employed in different areas including textile, dyeing, paper and pulp, tannery and paint industries.[1-3] Hence, wastes of these industries as well as those from plants manufacturing dyes tend to contain such compounds in sufficient quantities. Although exact data on the amount of dyes discharged in the environment are not available, it is reported that 10–15% of employed dyes in dyeing procedures are loss through wastes.[1] They are considered an offensive type of pollutants because of their toxicity commonly due to oral ingestion and inhalation, skin and eye irritation, skin sensitization and carcinogenicity.[2,4-6] Even low amounts may impart color to water. This is not only an unpleasant phenomenon on appealing grounds but it also affects the transmission of light distressing biological metabolism processes and leading to destruction of aquatic communities present in environment.[7,8] Further, dyes have a tendency to strongly bond heavy metals and may cause microtoxicity to fish and other organisms.[8]

For these reasons, the development of strategies to rapidly remove this class of contaminants from wastewater and degrade them is still a matter of interest in the scientific community. Many approaches have been studied, however, it is very difficult to reach an efficient removal since most of dyes are resistant to traditional methods such as biological treatment,[9] chemical oxidation,[10] coagulation,[11] membrane filtration,[12] photochemical degradation,[13] flocculation and ion-

exchange.[14,15] On the contrary, adsorption has been revealed as a suitable and effective approach owing to its simplicity in processing design, easiness in working conditions, low cost, low energy necessity and insensitivity to toxic substances.[16] As adsorbents, a wide variety of materials has been tested for the removal of dyes from aqueous solutions.[3,17-19] Most of them, however, have slight adsorption capacities or require rather long adsorption contact time.

Starting from this, in order to develop effective adsorbent systems, two main objectives should be pursued to increase the efficiency of the process *i.e.* high adsorption ability and short contact time. The removal of dye may be in addition associated with its degradation by means of a sustainable procedure. As a green technology, photocatalysis represents an interesting solution and it has attracted extensive interest in the fields of water splitting and pollutant degradation.[20-22] In this regard, TiO_2 has been recognized as the most efficient photocatalyst for the degradation of organic pollutants in water and wastewater.[23-25] However, titanium oxide and conventional semiconductor photocatalysts are limited by their wide band gap and respond only to UV light which corresponds to less than 5% of sunlight energy.[26] Hence, in this context, a great challenge is represented by the development of visible light-driven photocatalysts with high efficiency, in order to better exploit the solar radiation spectrum.

An intriguing and promising solution to these challenges may be provided by bismuth oxychloride and oxycarbonate-based nanostructures, owing to their peculiar physico-chemical (structural, mechanical electrical and optical) properties and low toxicity.[27-29] Over the years, their unique properties have determined their use in different fields such as cosmetics, pharmaceuticals and pigment industry.[30-32] They have been also studied as heterogeneous catalysts for cracking of n-butane and oxidative coupling of methane.[33,34] Finally, in the last decade, they have attracted increasing interest due to their potential application as photocatalysts for solar energy conversion and degradation of organic pollutants with visible light.[35-49]

Bismuth oxyhalogenides ($Bi_wO_yX_z$: X= Cl, Br, I; w, y, z = variable integers) belong to the family of main group V-VI-VII multi-component metal oxyhalides,

a class of ternary layered compounds characterized by the coexistence of unique electrical, structural and optical properties (Fig. 2.1). These semiconductor compounds show a wide variety of Bi/O/X ratios. The simplest, BiOX, crystallizes in the tetragonal matlokite structure (PbFCl), a layered structure characterized by $[Bi_2O_2]$ positively charged sheets interleaved by double slabs of halogen atoms, to form [X-Bi-O-Bi-X] layers. Owing to the strong intra-layer bonding in $[Bi_2O_2]$ slabs and weak inter-layer interactions, BiOX is characterized by highly anisotropic structural, electrical and optical properties.[50] For example, an internal static electric field arises between $[Bi_2O_2]$ and halogen anionic layers and the weak inter-layer interactions allow the sheets to slide over each other.[39,51] Besides BiOX, further bismuth oxyhalides with different Bi/O/X ratios are possible, e.g. $Bi_{24}O_{31}X_{10}$, $Bi_{12}O_{17}X_2$, Bi_3O_4X, etc., all of them characterized by layered structures (Fig. 2.1).

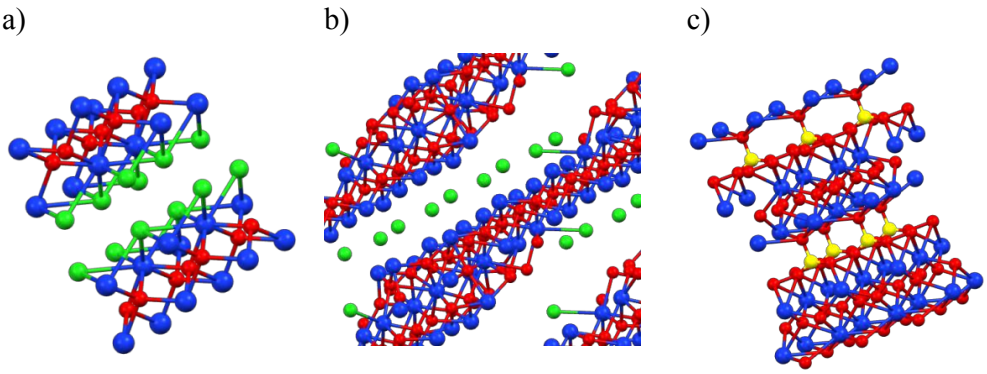

Fig. 2.1 Layered structures of **a)** BiOCl, **b)** $Bi_{24}O_{31}Cl_2$ and **c)** $(BiO)_2CO_3$. Colour code: Bi blue, O red, Cl green, C yellow.

Among them, structural differences concerning the different number and alternation of halogen and cationic slabs exist. In particular, two classes of systems can be identified. The first is constituted by compounds of the Sillèn family, expressed by $[Bi_2O_2][X_m]$ (m=1-3, e.g. BiOX and $(BiO)_2CO_3$), where metal-oxide based layers are intergrown with one to three double halogen layers. On the other hand, reverse Sillèn phase compounds present a composition regulated by the thickness of the bismuth-oxygen sheets, with an invariant single

halide layer.[34,52] $Bi_{24}O_{31}X_{10}$ and $Bi_{12}O_{17}X_2$, for example, are members of the latter family.

Bismuth oxyhalides represent an appealing solution that suits different needs since modulation of the Bi/O/X ratio allows to finely tune their properties. Optical absorption properties may be modulated in a large range of wavelengths, from UV to the entire visible. The different internal electric field between the layers is able to promote photoinduced charge separation and transfer from the bulk to the surface, enabling photocatalytic reactions on the latter.[39,53] Finally, the peculiar structural features of these compounds have been exploited to obtain a large variety of nanostructures such as nanorods and nanowires, nanoflakes and nanosheets or in flower-like 3D structures.[26,54,55] Morphologies characterized by high surface area are fundamental to guarantee high contact between adsorbent and pollutant, which is a key factor for an efficient removal of contaminants. Moreover, the same compound with a specific morphology may exhibit different adsorbent and photocatalytic properties because of the exposition of different crystal facets.[56,57] Thus, a great variety of synthesis strategies has been developed in last years to obtain nanostructures characterized by a defined chemical composition and peculiar morphological features, with the objective of improving their adsorption performances, combined to photocatalytic properties.[21,26,28,37,46,58-65] Among these, hydrothermal, solvothermal, reverse microemulsion and sonochemical synthesis have been widely employed.[26]

In this chapter, the development of soft-chemistry solution processes has been studied with the aim to obtain bismuth oxychlorides and subcarbonate-based nanostructures, as pollutant adsorbents endowed with solar light photocatalytic properties. Modulation of the synthesis conditions and different post-synthesis treatments were adopted to obtain a fine control of chemical composition, nano and micro-structural organization and optical absorption properties. An extended characterization of the obtained materials was conducted and in particular compositional, microstructural, morphological and optical properties were thoroughly investigated. Finally, adsorption and photocatalytic performances have been examined against two common organic dyes: methyl orange and rhodamine

B. RhB was employed as model for cationic dye pollutants whereas MO for anionic azo-dyes.

2.2 BiOCl and $Bi_{24}O_{31}Cl_{10}$

2.2.1 Experimental

The first optimized synthesis procedure was performed in aqueous solution, in presence of a surfactant as structure directing agent and under mild temperature conditions. Two different surfactants were tested with the aim to control growth and dimensions of the nanostructures as well to impart different morphologies to the final product. Brij 76 is constituted by an extended linear alkyl chain linked to a polyethylene glycol (PEG) portion and an average molecular weight (AMW) of 1151.56 g/mol (Fig. 2.22.2a). Pluronic 123, named P123 in the following, is a symmetric triblock copolymer with an AMW of 5800 g/mol, constituted by the succession of PEG-PPG-PEG blocks, where PPG stands for polypropylene glycol (Fig. 2.2b).

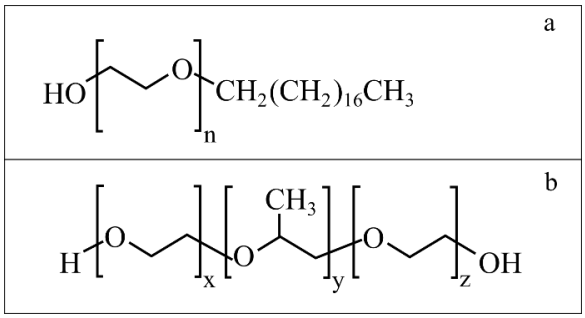

Fig. 2.2 Molecular structures of the employed structure directing agents: a) Brij 76 and b) P 123.

In aqueous solution, both of these surfactants are able to generate micellar structures, which may direct nucleation and growth processes within the reaction medium. The employed precursor, bismuth chloride ($BiCl_3$), provided both the metal and the halogen to the system, without the need of further reactants. As reported in Scheme 2.1, $BiCl_3$ was hydrolyzed under highly acidic conditions and the product was obtained by precipitation with lithium hydroxide. This first

method, named *neutral synthesis*, was conducted at 35 °C and the precipitation of BiOCl was stopped when neutral pH value was reached. Powders were collected through centrifugation and washed with water and ethanol.

Neutral synthesis

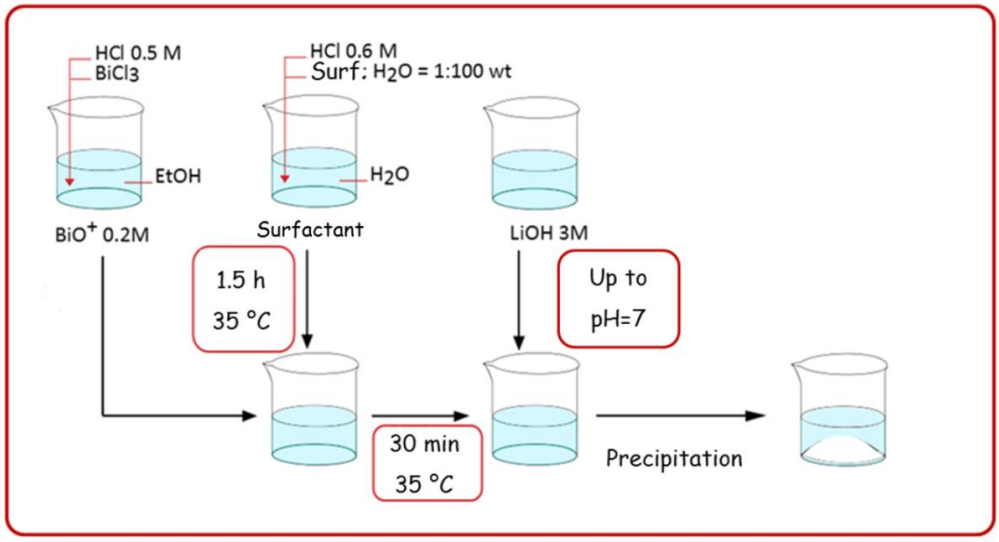

Scheme 2.1 Synthesis procedure conducted at neutral conditions.

2.2.2 Results and discussion

Thermogravimetric analysis (TGA, Fig. 2.3.3) of as prepared samples revealed the decomposition of residual surfactant (both for P123 and Brij 76) under 350 °C and a wide range of stability of the inorganic system up to 650-700 °C, where a severe loss of weight was observed.

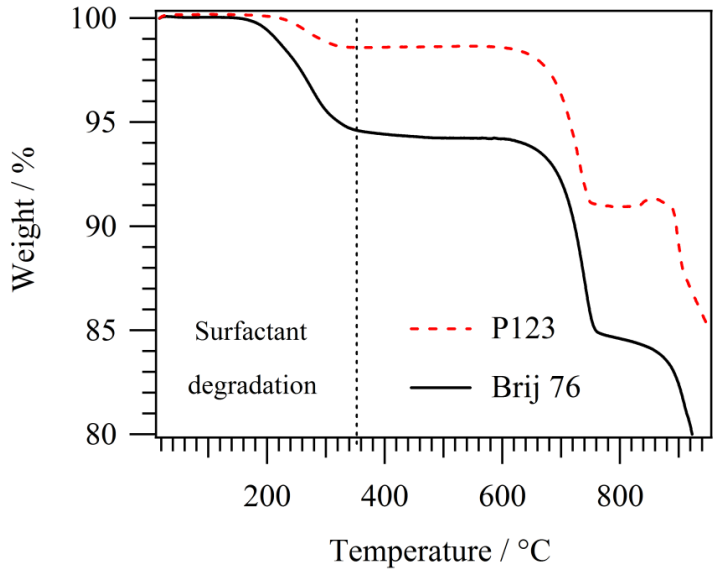

Fig. 2.3 TGA analysis: as prepared samples synthesized with P123 or Brij 76.

As prepared materials were hybrid systems containing residues of surfactant which were removed by post-synthesis annealing treatments in air, originating a pure inorganic system. Moreover, different thermal treatments were employed also to induce a controlled decomposition of the materials, thus allowing the modulation of oxygen and chlorine content in the samples. In particular, three different post-synthesis thermal treatments were selected in a region of stability and in proximity of a drop in the TGA curve: 1 and 3 hours at 600 °C and 1 hour at 700 °C. This is because bismuth oxychlorides compounds subjected to treatments at increasing temperature (and time) undergo a loss of chlorine content until reaching the stoichiometry of bismuth oxide. Hence, in this way, the

formation of defects and a shift of the optical absorption onset towards the visible are favored.

Microstructural analysis evidenced that a modulation of the phase composition was induced by means of thermal treatments. The XRD pattern of sample treated for 1 hour at 600°C showed a set of peaks in the 10-60 2θ° range which can be indexed according to the tetragonal phase of BiOCl [JCPDS 06-0249] (*- Fig. 2.4). Upon increasing time and temperature of the thermal treatments, the presence of new crystalline phases with a minor chlorine content was observed, although BiOCl remained the primary phase. In particular, $Bi_{24}O_{31}Cl_{10}$ was identified as the predominant secondary phase and its main diffraction peaks (#) were evidenced in Fig. 2.4.

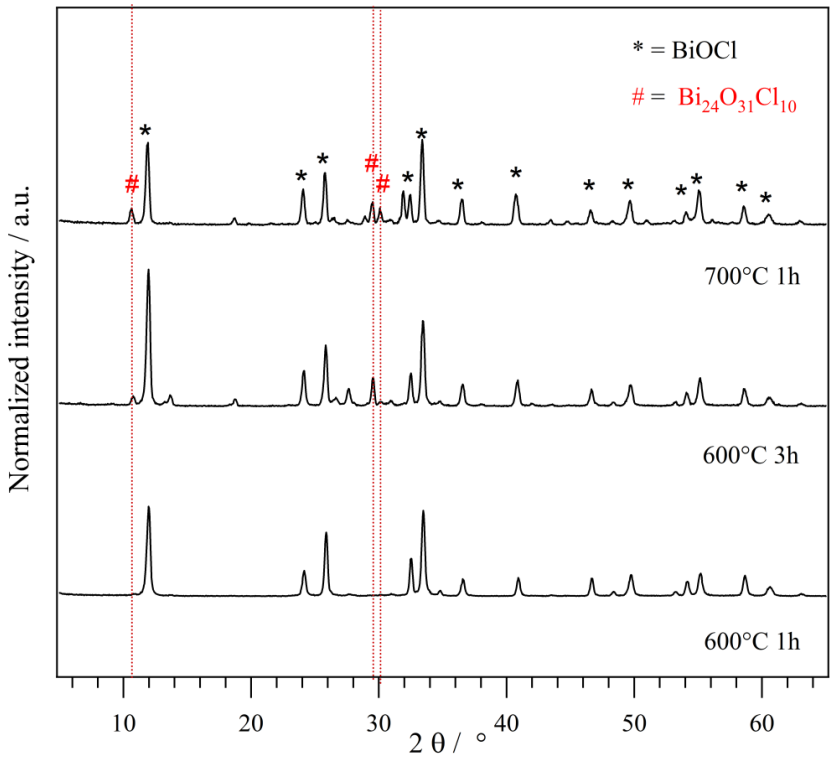

Fig. 2.4 Effect of thermal treatments for samples obtained with P123: main diffraction peaks of BiOCl (*) and $Bi_{24}O_{31}Cl_{10}$ (#).

This trend was observed for samples synthesized both with P123 and Brij 76. However, the two series differed from each other for the relative intensity of the diffraction peaks, due to the presence of possible preferential orientations or asymmetric crystallites.

Absorption spectra of as prepared samples (Fig. 2.5) presented a profile typical for a semiconductor with an absorption edge of 365 nm (bandgap = 3.4 eV), in agreement with the literature values for BiOCl.[39] After thermal treatments, an increasing absorption at higher wavelengths was observed and it was correlated to the presence of new phases with a lower content of chlorine atoms. In particular, the typical absorption edge for the Arppe's phase $Bi_{24}O_{31}Cl_{10}$ (496 nm, 2.5 eV) was compatible with the second absorption component observed in Fig. 2.5, in the 350-500 nm range.[66] Accordingly, the color of samples turned from white to light yellow.

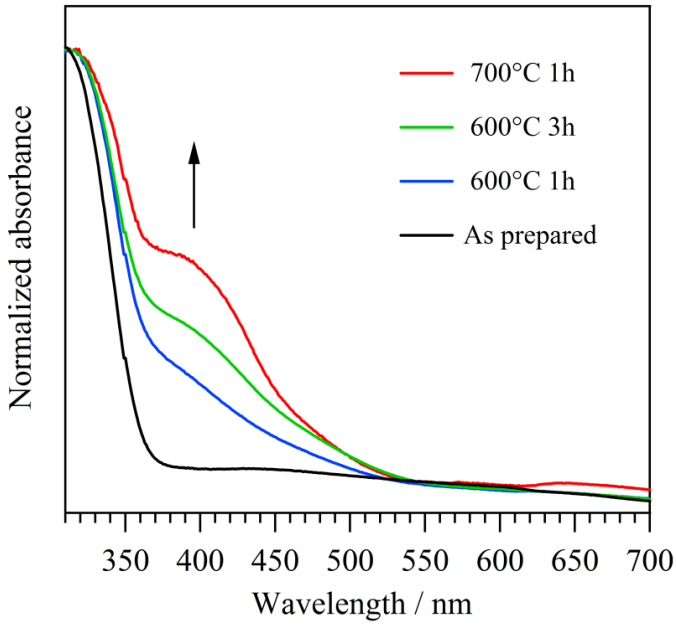

Fig. 2.5 Effect of post-synthesis annealing treatments on diffuse reflectance spectra, P123.

X-ray Photoelectron Spectroscopy (XPS) allowed to analyze the surface chemical composition of nanostructures. The extended spectrum (not shown) revealed the expected bismuth, oxygen, carbon and chlorine peaks in all samples. The Bi4f

signal displayed the distinctive $4f_{7/2}$ and $4f_{5/2}$ doublet (Δso = 5.3 eV) due to spin–orbit coupling, at binding energy (BE) values typical for Bi^{3+} species (Bi $4f_{7/2}$ = 159 eV).[67] The Cl2p signal, an unresolved doublet centered at BE~198 eV, was characteristic for Cl^- anions.[67] Both Bi4f and Cl2p signals did not change by varying the thermal treatment conditions. On the contrary, C1s and O1s signals showed substantial changes moving from as prepared to treated samples, revealing the presence of organic species likely due to the surfactant in absence of annealing. In particular, C1s peak in as prepared samples shows a broad band profile due to the presence of two component at BE values of 284.8 and 286.6 eV (I and II - Fig.). The former was attributed to adventitious carbon while the latter was due to ether residues of surfactant molecules and disappeared after thermal treatment (II - Fig.).[67]

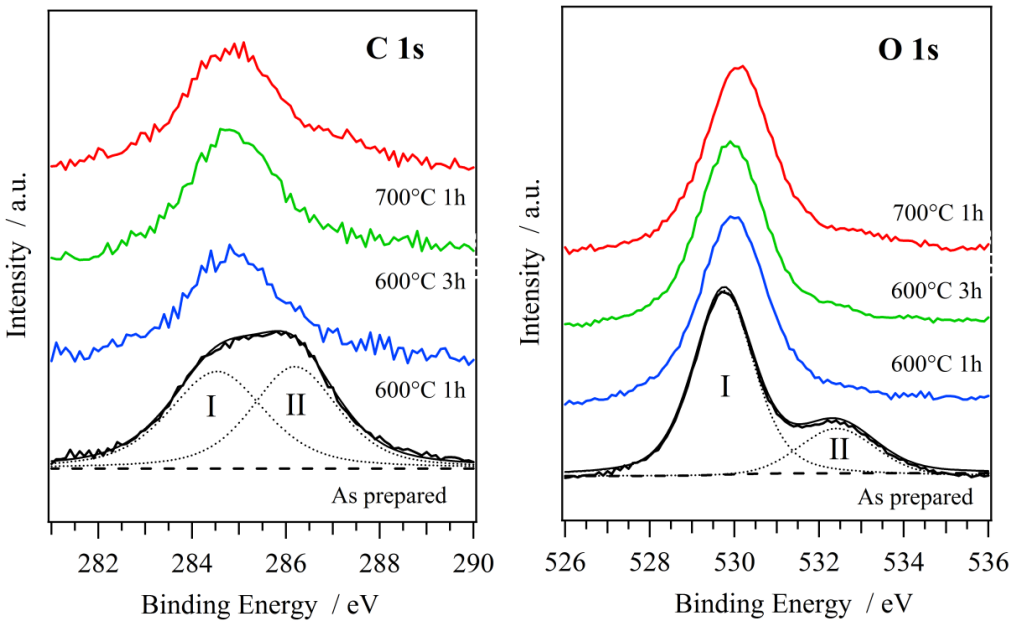

Fig. 2.6 Effect of thermal treatments on C1s and O1s peaks in XPS spectra, P123.

Similarly, O1s presented an asymmetric shape with a shoulder on the high binding energy side. While the component at low BE (~530 eV- I, Fig.) was related to lattice oxygen in a bismuth oxychloride network, the high BE contribution was ascribed to C-O residues of the surfactant and it was detected only in the as

prepared samples.[54,68] Quantitative analysis confirmed the presence of a higher content of carbon in as prepared samples. At the same time, Bi:O:Cl ratios revealed small chlorine losses after thermal treatments.

Irrespective of the diverse treatments and employed surfactants, low surface area values were obtained, all in the range of 10 m^2/g. Morphological characterization of the nanostructures was conducted through field emission scanning electron microscopy (FE-SEM). A similar evolution was observed as function of the annealing treatments, irrespective of the surfactant employed. For this reason, only samples prepared with Brij 76 will be discussed in the following. After 1h at 600 °C, the co-presence of two different morphologies was observed: flakes of various shapes (hexagonal, square, rhombohedral or irregular) as well as rods with lamellar structure (Fig. 2.7a, b, c).

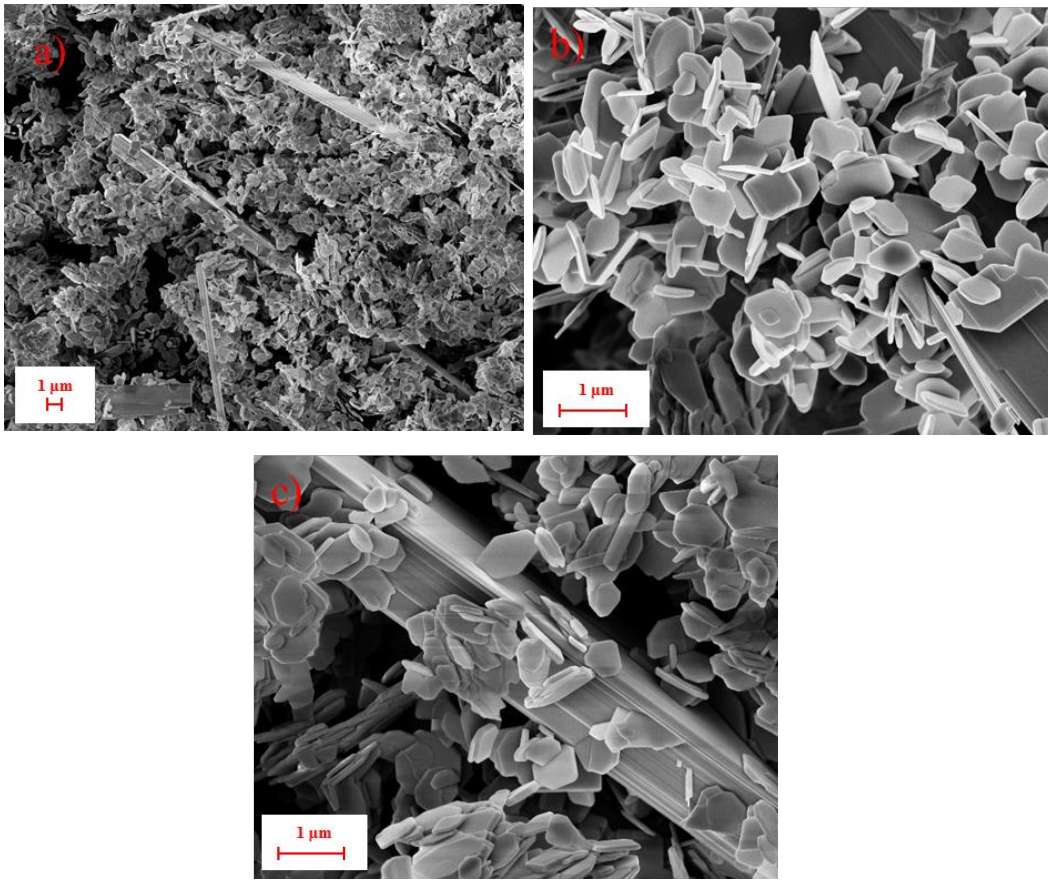

Fig. 2.7 SEM images of samples annealed 1h at 600°C, Brij 76.

By prolonging the thermal treatment (600°C, 3h), the formation of a higher number of rods and their partial coalescence were observed (Fig. 2.8a). Despite these variations, flakes were still present in the sample (Fig. a and b).

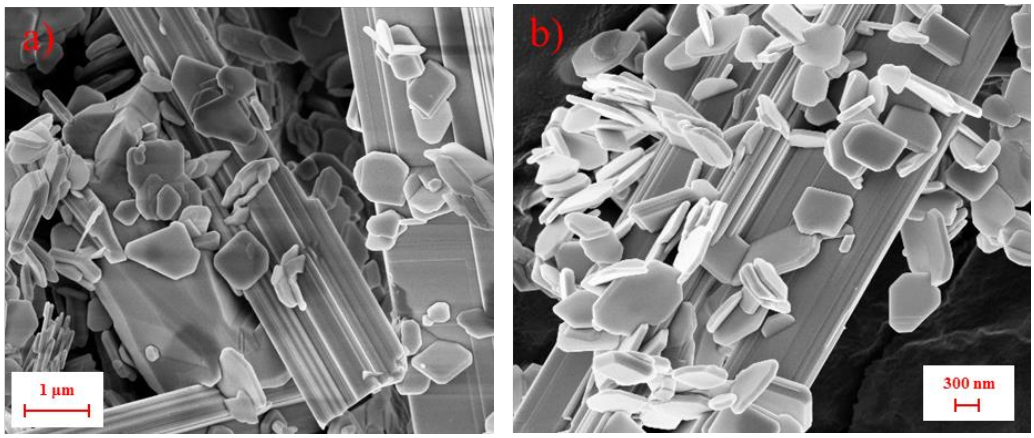

Fig. 2.8 SEM images samples annealed 3h at 600°C, Brij 76.

Finally, the highest temperature treatment (700°C 1h) caused a diffuse coalescence of rods and flakes leading to the formation of large slabs tenths of micrometer wide (Fig. 2.92.9a).

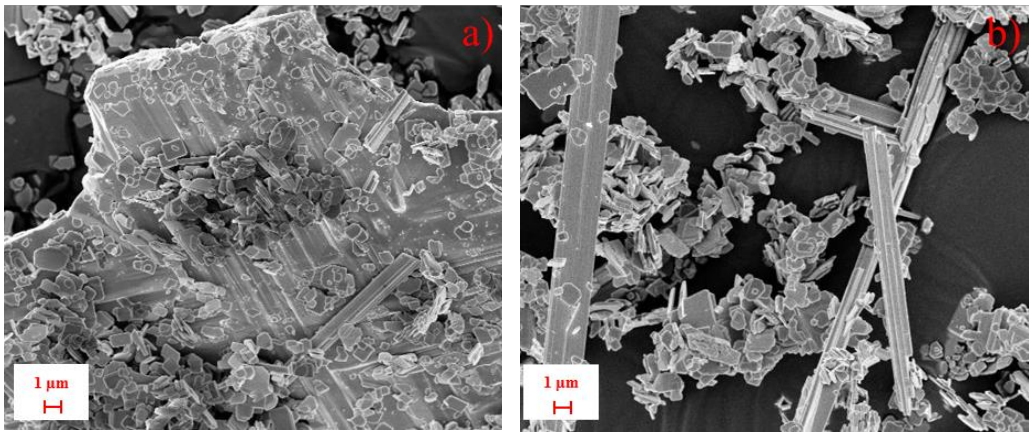

Fig. 2.9 SEM images samples annealed 1h at 700°C, Brij 76.

In general, with respect to Brij 76, samples prepared by using the P123 surfactant were characterized by flakes with slightly smaller dimensions. On the contrary

samples obtained conducting the synthesis without the employment of surfactants were characterized by flakes of higher dimensions densely packed to form a bulk material (not shown).

Adsorption and photocatalysis

Photocatalytic performances of samples synthesized with both surfactants were evaluated and MO degradation was investigated under continuous irradiation with visible light. In each experiment, 200 mg of catalyst were added to 160 mL of an aqueous solution $1.9 \cdot 10^{-5}$ M in MO. Prior to illumination, the suspension was continuously stirred in the dark for 45 min to reach the adsorption/desorption equilibrium of the dye on the surface of the photocatalyst. At given time intervals, aliquots of the suspension were withdrawn and filtered.[69] Then, by means of UV-Vis spectrophotometry, the variation of the concentration of MO was evaluated monitoring the maximum absorption band of the dye at 464 nm. The decoloration efficiency is reported in Fig. 2.10 as C/C_0, where C is the MO concentration after adsorption or photodegradation, and C_0 is the initial concentration.

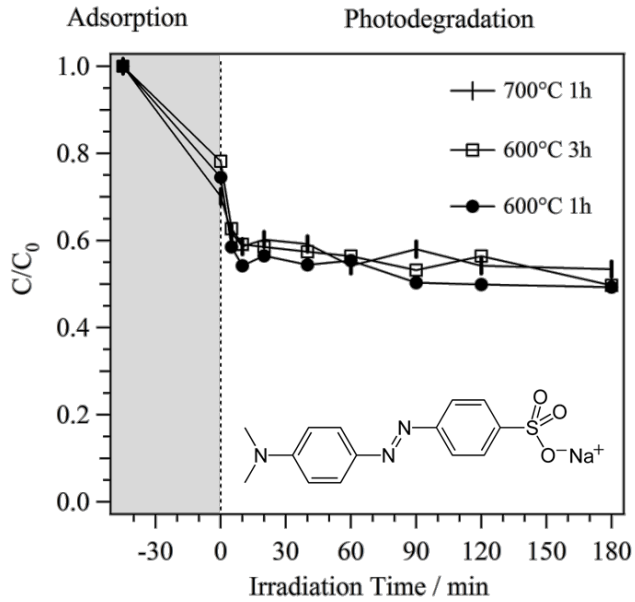

Fig. 2.10 Photocatalytic degradation tests of MO, conducted in presence of samples synthesized with P123.

Irrespective of the employed surfactant and the temperature of the thermal treatment all samples displayed a similar behavior. After 45 minutes without illumination, $BiOCl/Bi_{24}O_{31}Cl_{10}$ nanostructures showed weak adsorbent efficiency removing from 20 up to 30 % of the dye. Then, after irradiation with visible light a low catalytic activity was observed which lead to the degradation of further 30 % of the dye in 180 minutes. Hence, the global process allowed us to remove 50 % of the model contaminant in solution. In this regard, the low surface area values (<10 m^2/g) may be responsible for poor adsorption properties displayed by the whole set of samples. Moreover, these surface features may also hamper an efficient catalyst-dye interaction that is essential to allow the photocatalytic process. Finally, poor degradation under solar-like irradiation may be correlated to unsufficient absorption of the portion of visible light by catalyst. All these aspects may be improved with further synthetic efforts by pursuing two main objectives: enhanced adsorbent capacity and upgraded photocatalytic activity.

2.3 $Bi_{12}O_{17}Cl_2$ and $(BiO)_2CO_3$

In order to develop new bifunctional nanostructures for adsorption and photodegradation based on bismuth oxychlorides and derivatives, further investigation was conducted by means of a combined approach. Beside an appropriate modulation of the synthesis parameters, the employment of post-synthesis treatments represents an interesting possibility to get further tuning of the properties of raw materials. Starting from the results previously discussed, a new synthesis procedure was developed in order to obtain a material endowed with higher surface area and higher absorption in the visible range. Both these characteristics are important to give to the final material better performance as adsorbent as well as visible-light-driven photocatalyst. The synthesis was conducted at slightly higher temperatures (65 °C) with the aim of stimulating a higher action of the structure directing agents on the nucleation and growth of the nanostructures. Moreover, to improve photocatalytic properties, band gap engineering is essential either to narrow the band gap and to introduce proper defects. The new systems was obtained by operating in alkaline conditions, instead of neutral as in the previous case, in order to induce further modulation of the chemical composition, leading to bismuth oxychloride derivatives endowed with a minor chlorine content. This affected the absorption features which were shifted to higher wavelengths. Finally, different post-synthesis treatments on the raw product were also considered as an alternative tool for the modulation of its chemico-physical properties. In the following, outcomes of the developed synthesis strategy and the effect of the adopted treatments will be discussed in terms of modifications induced on microstructure, composition, morphology, optical properties and functionality.

2.3.1 Experimental

Similarly to the neutral procedure, the alkaline synthesis was conducted in aqueous solution employing Brij 76 or P123 as structure directing agent. Solution A was obtained dissolving $BiCl_3$ (0.2 M) in ethanol at room temperature and

adding the minimum amount of HCl (37%). On the contrary, solution B was prepared dissolving the surfactant (1%wt) under stirring, at 65 °C, in a HCl 0.6 M aqueous solution. After mixing solution A with B (volume ratio 1:15), the resulting mixture was aged for 5 h at 65 °C under continuous and vigorous stirring. The product was obtained by precipitation with an excess of LiOH (2 M). The resulting yellow powder was collected by centrifugation, washed with water and ethanol, and dried in air.

Alkaline synthesis

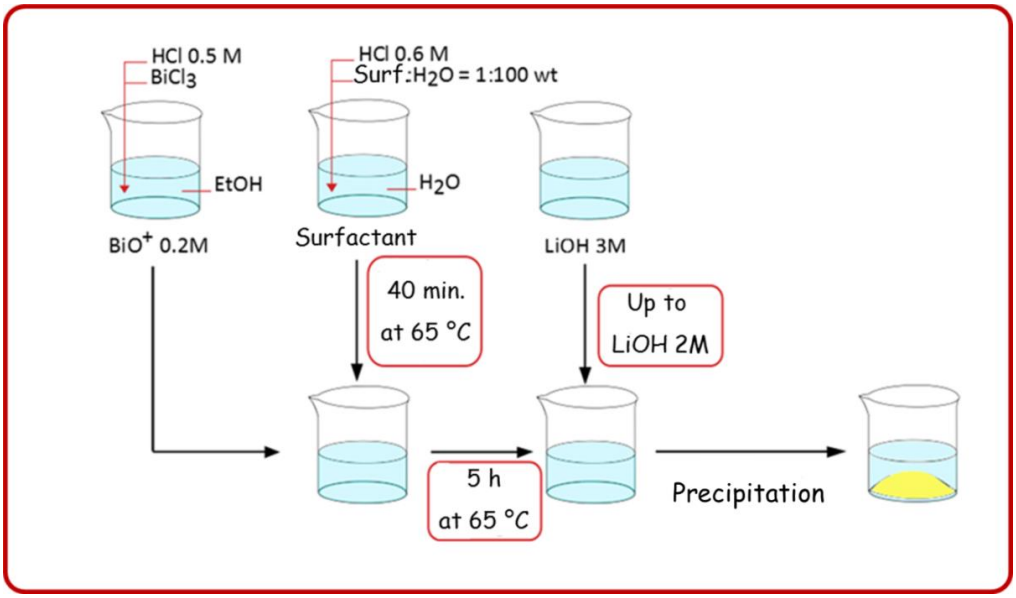

Scheme 2.2 Synthesis procedures: precipitation induced at alkaline conditions.

2.3.2 Results and discussion

Thermogravimetric analysis revealed substantial differences for as prepared samples synthesized in alkaline conditions, compared to the neutral procedure, and a similar trend irrespective of the different employed surfactant was observed. An initial loss of weight was observed at low temperature (<200 °C) that can be assigned to the removal of water adsorbed on the surface of the raw powders. Then, a further drop in the TGA curve up to 450 °C was correlated to the

degradation of the residual surfactant (both Brij 76 and P123). Finally, a wide range of stability from 450 up to 800 °C was observed (Fig. 2.12.11).

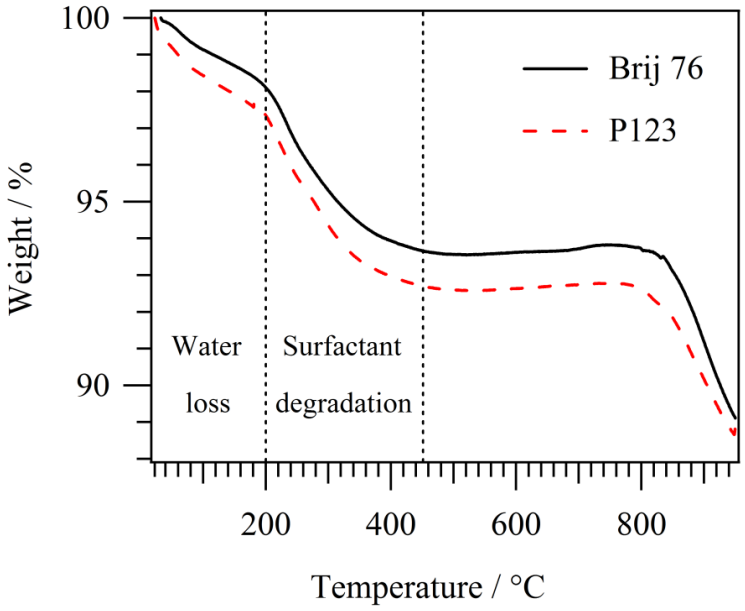

Fig. 2.11 TGA analysis of as prepared samples obtained by means of alkaline synthesis (P123 and Brij 76).

Given these observations, different post-synthesis treatments were conducted on as prepared samples, in order to obtain a pure inorganic system by removing the residual surfactant and to modulate their characteristics. Thermal treatments with different calcination conditions were employed. In particular, samples were treated: i) in O_2 (30% in Ar), 6 h at 370 °C (heating ramp 0.5 °C/min); ii) in air, 6 h at 420 °C (heating ramp 0.5 °C/min), iii) in air, 1 h at 500 °C (sample inserted and removed in temperature). The removal of surfactant was achieved also with room temperature UV treatments, dispersing the powders in aqueous solution and irradiating the mixture with a medium-pressure Hg lamp (450 W) for 14 h.

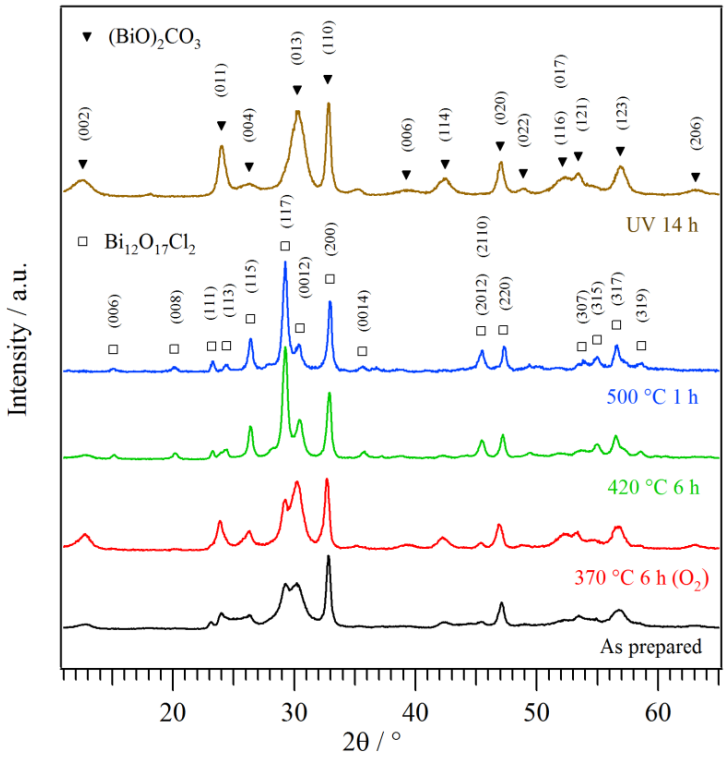

Fig. 2.12 XRD patterns of as prepared and treated samples, peculiar diffraction peaks of $(BiO)_2CO_3$ (▼) and $Bi_{12}O_{17}Cl_2$ (□) tetragonal phases are labelled.

The structure of as-prepared and treated materials was characterized by X-ray powder diffraction analysis. Despite the mild synthesis conditions employed (e.g. low temperature and ambient pressure) and the absence of any thermal treatment, as prepared samples showed a pattern with multiple diffraction peaks (Fig. 2.1). The whole set of peaks can be indexed to two different phases: $Bi_{12}O_{17}Cl_2$ (JCPDS card. no. 37-0702) and $(BiO)_2CO_3$ (JCPDS card. no. 41-1488). The main reflexes of both phases are localized in the 20-35° 2Θ range and are partially overlapped. In particular, the strong narrow peak around 33° can be indexed both as (200) of $Bi_{12}O_{17}Cl_2$ and (110) of $(BiO)_2CO_3$.

In this case, the as prepared material was thus constituted by a biphasic $Bi_{12}O_{17}Cl_2/(BiO)_2CO_3$ system. $Bi_{12}O_{17}Cl_2$ is a bismuth oxyhalogenide with low chlorine content, characterized by a tetragonal structure.[70-72] It is characterized by

the presence of single chlorine layers interleaved with metal-oxide sheets.[34] On the other hand, $(BiO)_2CO_3$, or bismutite, belongs to the family of Sillén phases. Interleaved $[Bi_2O_2]^{2+}$ and CO_3^- layers characterize its crystalline tetragonal structure where the carbonate groups are placed orthogonally to the plane of the metal-oxide layer.[73-75]

Post synthesis treatments on these samples induced a change in the phase composition of the material. In fact, samples treated 6 h at 370 °C in presence of O_2 were characterized mainly by the $(BiO)_2CO_3$ phase and the characteristic (002), (011) and (013) reflexes at 12.8°, 23.9° and 30.3° can be clearly identified (Fig. 2.1). Thus, operating in an oxygen rich atmosphere a stabilization of the bismuth subcarbonate phase at the expense of the chlorinated one was obtained. On the contrary, a thermal treatment of the same length in air at 420 °C led to the formation of $Bi_{12}O_{17}Cl_2$ as the main phase. Moreover, with a fast treatment of 1 h at higher temperature (500 °C) $Bi_{12}O_{17}Cl_2$ was obtained as single phase. Conversely, UV treatments on as prepared samples allowed the formation of a primary $(BiO)_2CO_3$ phase together with the complete disappearance of the chlorinated phase. Finally, it is noteworthy to mention that samples synthesized with different surfactants and obtained by adopting the same treatment were characterized by similar microstructural properties. For example, in Fig. 2. a comparison between the diffractograms of samples with low chlorine content phase is reported: position, intensity and FWHM of peaks of the $Bi_{12}O_{17}Cl_2$ phase [JCPDS 37-0702] did not change in presence of different surfactants.[72]

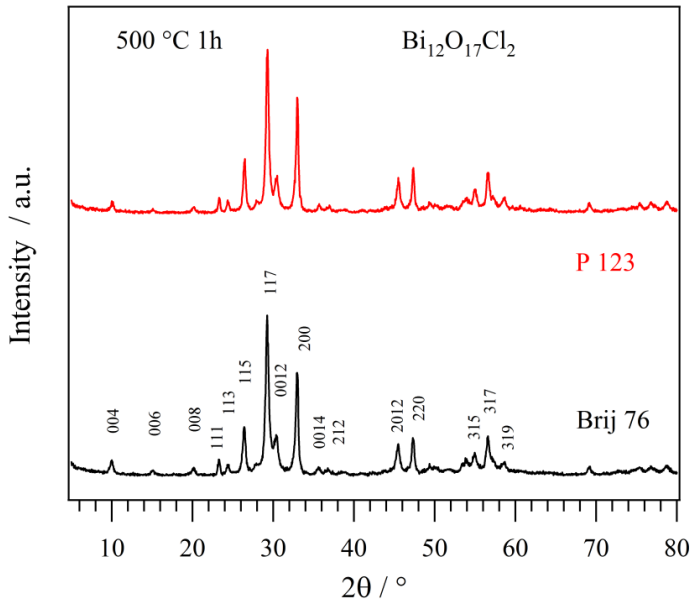

Fig. 2.13 XRD pattern of samples obtained with the alkaline procedure, P123 or Brij 76 and treated 1h at 500°C. Main reflexes of the $Bi_{12}O_{17}Cl_2$ phase are labelled.

Together with a modulation of the microstructure, thermal and UV treatments resulted in a variation of the optical properties of the nanostructures. The trend observed in the absorption spectra reported in Fig. 2.14 can be well explained by considering the different relative amount of $Bi_{12}O_{17}Cl_2$ and $(BiO)_2CO_3$, which are characterized by absorption edges localized respectively around 520 and 400 nm.[44,46,76] Accordingly, samples characterized by $Bi_{12}O_{17}Cl_2$ as the major phase presented an higher absorption in the visible region. These samples were treated at higher temperature (420 °C 6 h and 500 °C 1 h). Conversely, when the subcarbonate phase was predominant a blue shift of the absorption band was observed (Fig. 2.14).

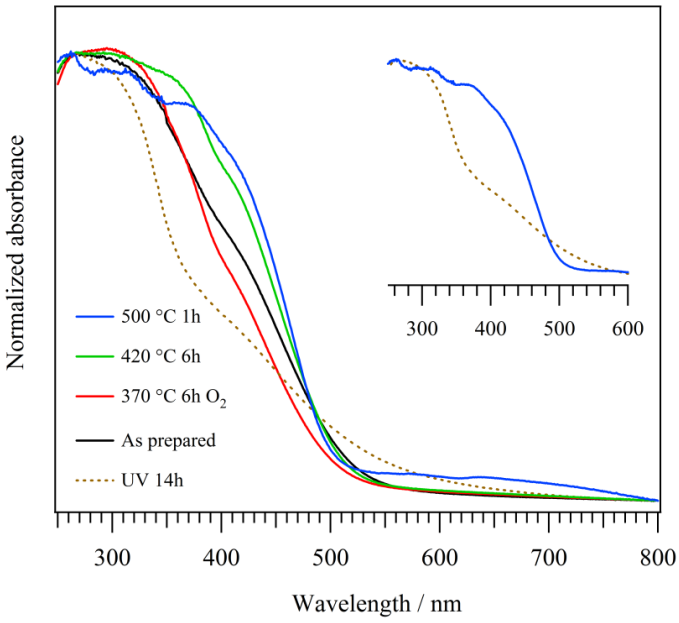

Fig. 2.14 UV-Vis diffuse reflectance spectra of as prepared and treated samples, Brij 76.

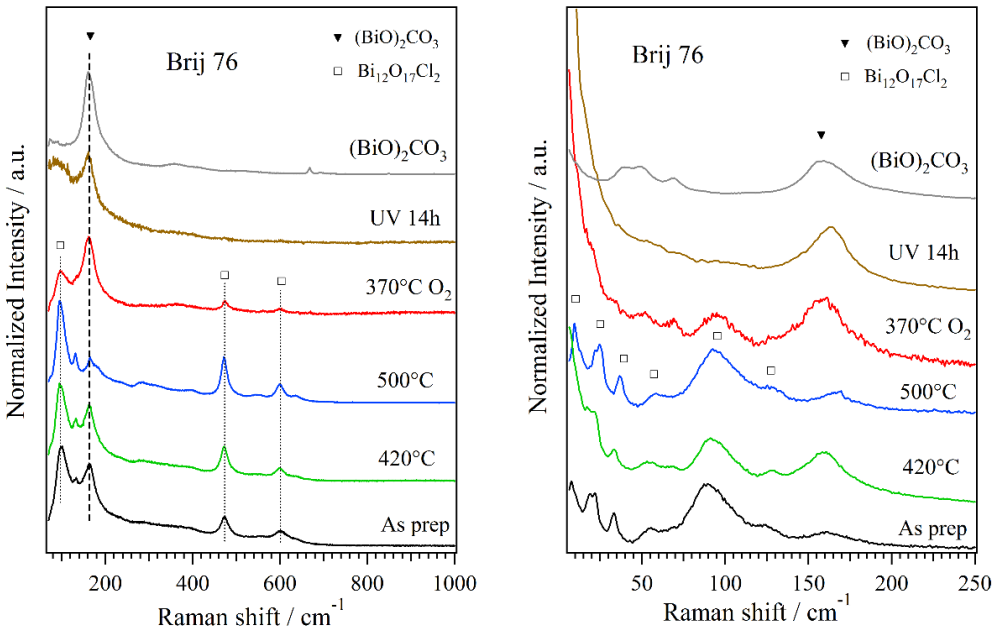

Fig. 2.15 Extended Raman spectra and magnification of the low Raman shift region.

According to XRD and absorption spectra, Raman spectra provided further evidences on the modulation of composition characterizing the different samples. As reported in Fig. , in all samples except for the one UV treated, characteristic bands appeared at 96, 474 and 600 cm^{-1} and at low Raman shift values, *i.e.* 9, 21 and 25, 37, 58 cm^{-1}. These signals were indexed with the symbol (□) and were mainly referred to the $Bi_{12}O_{17}Cl_2$ component. In fact, they gradually disappeared moving to samples in which the $Bi_{12}O_{17}Cl_2$ content was minimized in favour of $(BiO)_2CO_3$ (370 °C and UV 14h). Although assignment of these contributes was not easy because of the lack of specific references, bands between 350 and 600 cm^{-1} were correlated to "lattice vibrations", arising from the motion of oxygen atoms in $(BiO)_n^{n+}$ slabs.[75] Accordingly, in samples where subcarbonate was the predominant phase, Raman spectra were essentially characterized by a single band at 163 cm^{-1} (▼, in Fig. 2.15) which well correlated with the external vibration modes assigned to $(BiO)_2CO_3$ in literature.[47] Moreover, spectra collected for sample treated 14h at UV closely resembled the one obtained from commercial $(BiO)_2CO_3$ and reported for comparison at the top of Fig. .

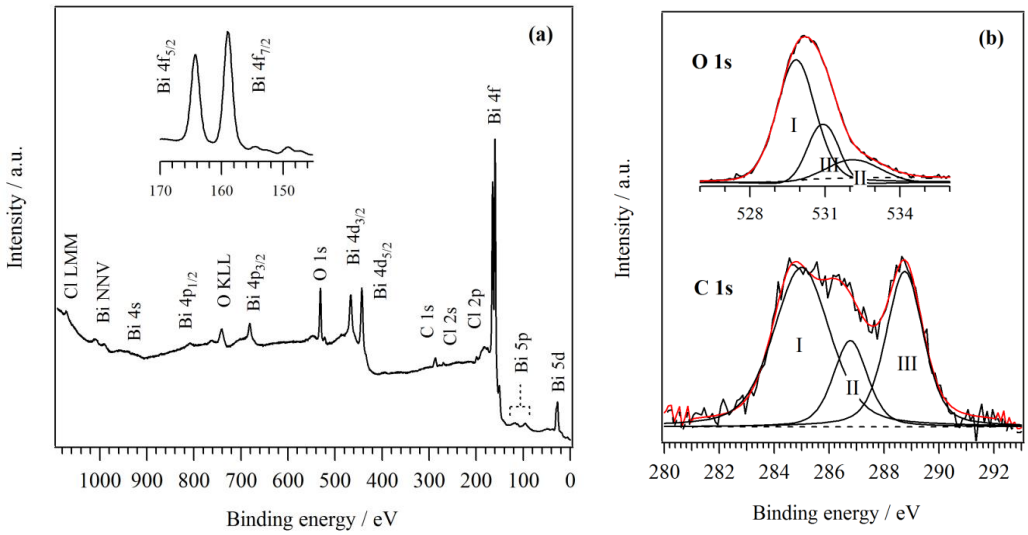

Fig. 2.16 XPS spectra of as prepared powders with Brij 76 as surfactant: (a) wide scan (survey) and high-resolution Bi 4f peak (inset); (b) high resolution spectra of O 1s and C 1s are reported.

The XPS survey spectrum of as prepared samples (in Fig. 2.16a, Brij 76) showed only the presence of Bi, O, Cl and C characteristic peaks, indicating the absence of any contamination in the raw materials, e.g. Li^+. The Bi 4f high resolution spectrum (inset Fig. 2.16a) displayed two intense peaks at BE values of 159.0 and 164.3 eV which can be assigned respectively to the j = 7/2 and 5/2 components of bismuth in the oxidation state +3.[67] In agreement with the presence of chlorine anions, in the region of the Cl 2p signal an unresolved doublet was observed at BE (Cl $2p_{3/2}$) = 199.5 eV.[67] Moreover, the C 1s photoelectron peak showed a broad profile due to the presence of multiple carbon species. The component at lower BE (I, Fig. 2.16b) can be assigned to adventitious carbon (BE = 284.8 eV) and to the aliphatic residues of the surfactant.[67,68] At higher BE other two components centered at 286.7 and 288.7 eV can be identified. The first (II, Fig. 2.162.16b) is ascribed to C-O ether groups of the residual surfactant, while the second (III) is attributed to higher oxidized species such as carbonates. In fact, the highly alkaline synthesis conditions employed can favor carbonation of the solution through the reaction with atmospheric carbon dioxide. Moreover, the O 1s peak showed an asymmetric shape with a shoulder on the high binding energy side (Fig. 2.16b). The whole signal can be well fitted by three components assigned to: i) lattice oxygen in $[Bi_2O_2]$ slabs (529.9 eV), ii) hydroxyl and carbonate groups (531.0 eV), iii) ether groups of the residual surfactant (532.3 eV) (Fig. 2.16b).[47,67]

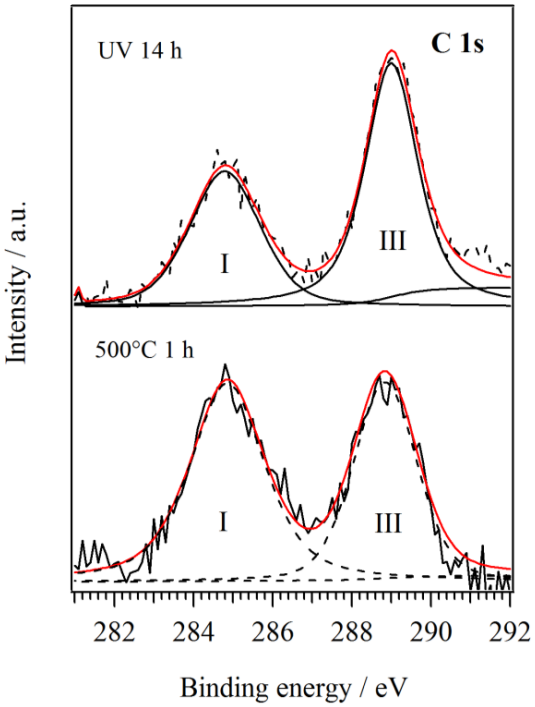

Fig. 2.17 High resolution spectra of C1s peak showing a comparison between thermal (500 °C 1 h) and UV treatments.

After thermal and UV treatments, the efficient removal of the residual surfactant from the surface was revealed. In fact, as clearly visible in Fig. 2.17, the disappearance of the component II, assigned to Brij 76, was observed in the C1s region for both types of treatments. On the contrary, components I and III, attributed respectively to adventitious carbon and carbonate ions, were still clearly distinguishable (Fig. 2.17).[45,67] The O 1s peak centered around 530.3 eV showed a symmetric shape. No variations of the position and band profile of the Bi 4f photoelectron signals were observed, and a low content (5%) of chlorine anions on the surface was detected in all the treated samples. Finally, analogous surface composition was observed for the set of samples synthesized with P 123 (not shown).

Specific surface area measurements and SEM analysis were conducted on the whole set of samples in order to study the effects of the adopted post synthesis procedures. Irrespective to the diverse treatments and employed surfactants, similar surface area values were obtained, all in the range of 10-15 m^2/g. Hence, in terms of accessible area provided by the absorbent nanostructure, conditions adopted in the alkaline procedure were not sufficient to improve the results obtained with the neutral synthesis. On the contrary, different morphologies were observed especially by employing distinct post synthesis procedures *i.e*. thermal or UV treatments. However, also in this case no substantial changes were induced by the employment of two different surfactants. These findings gave further indication that for the adopted synthesis condition both surfactants directed in a similar way nucleation and growth of the inorganic nanostructure. In particular, they allowed to control the dimensions of the particles in a similar range without imparting different shapes to the final product.

As shown in Fig. , as prepared samples (Brij 76) were characterized by the presence of small aggregates of irregular shape constituted by very thin flakes randomly orientated and with dimensions in the order of a hundred of nanometers. This morphology was observed in the whole sample, which was thus highly homogeneous.

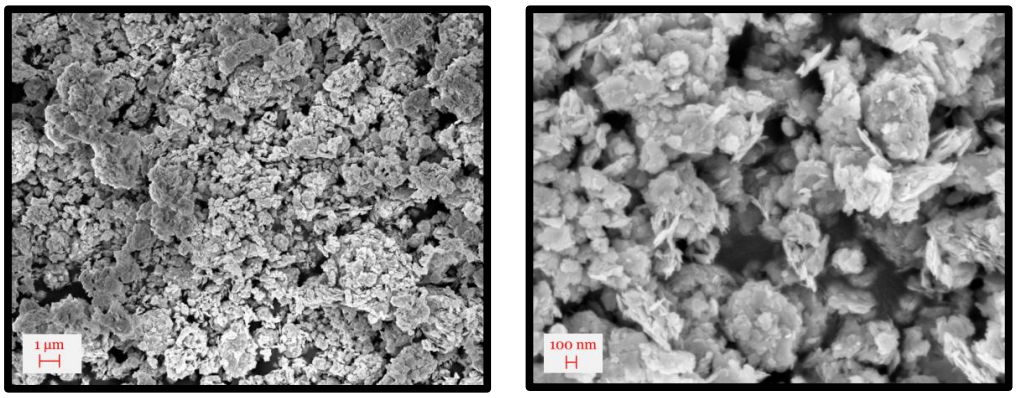

Fig. 2.18 SEM images of as prepared samples, synthesis with Brij 76.

By applying a thermal treatment at low temperature, in oxygen rich atmosphere (6 h, 370 °C (O_2)), coalescence of the thin sheets was induced and the formation of flakes of irregular shape with a broad distribution of dimensions was observed (Fig. 2.19).

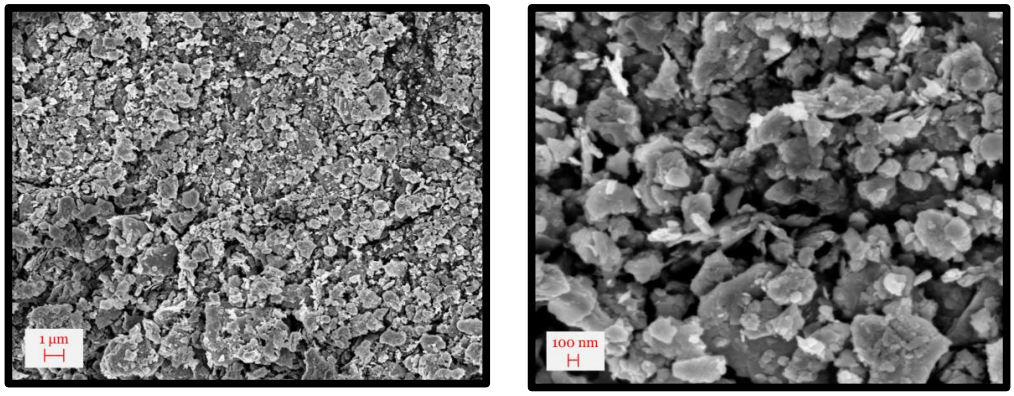

Fig. 2.19 SEM images of samples treated 6 h at 370 °C in presence of O_2, synthesis with Brij 76.

As a result of the treatment conducted at higher temperature in air (6 h at 420 °C), a similar morphology was obtained. However, in this case a less compact arrangement of the flakes was observed and, at high magnification, the stacking tendency of the initial constituents to form thicker and wider flakes can be appreciated (Fig. 2.20).

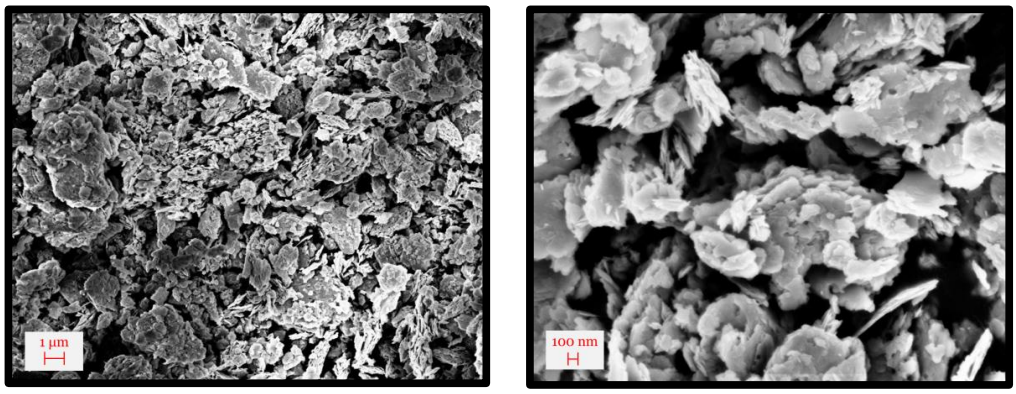

Fig. 2.20 SEM images of samples treated 6 h at 420 °C in air, synthesis with Brij 76.

A substantial change in the morphology of the nanostructures was observed after short thermal treatments at the highest temperature (1 h 500 °C), with some

differences depending on the employed surfactant. In fact, as clearly visible in Fig. 2., the use of Brij 76 led to a highly homogeneous distribution of very thin flakes of similar dimensions (a hundred of nanometers wide). Thus, contrary to the previous reported procedures, the faster thermal treatment did not induce the coalescence of the flakes. Similarly, in the sample synthesized with P123 the presence of the thin flakes was still appreciable but in this case a denser and less homogeneous distribution was observed (not shown).

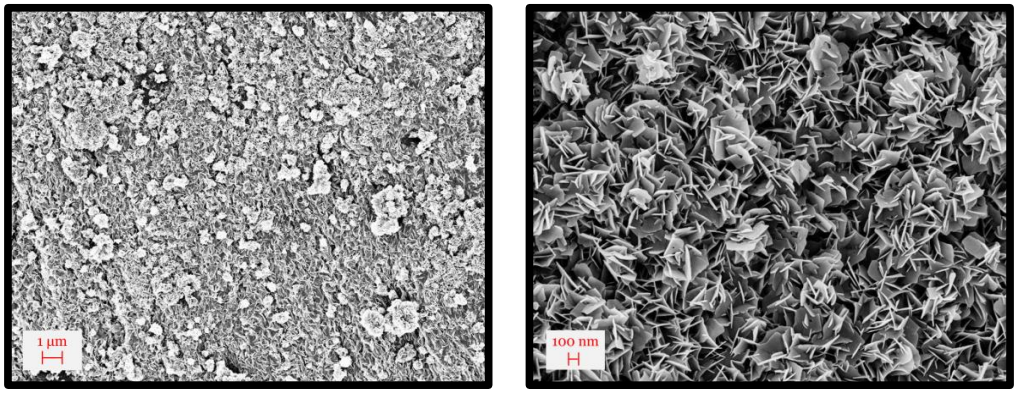

Fig. 2.21 SEM images of samples treated 1 h at 500 °C in air. Synthesis with Brij 76 (at the top) and with P 123 (at the bottom).

Finally, samples subjected to UV irradiation displayed an even more different morphology, characterized by a sponge-like texture. In Fig. , aggregates in the micrometer range, constituted by randomly orientated thin flakes can be clearly appreciated. Similar features were observed for samples synthesized with the two surfactants and, compared to those obtained with thermal treatments, an apparent higher fraction of empty space was visible.

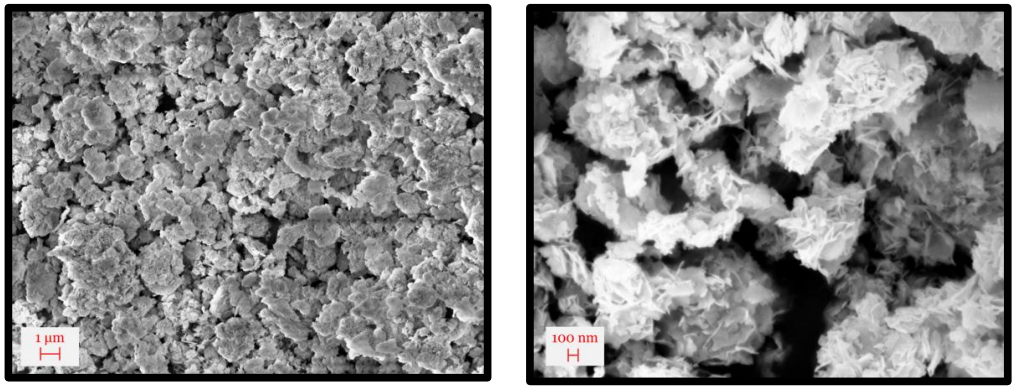

Fig. 2.22 SEM images of samples treated under UV for 14 h, synthesized with Brij 76.

These findings well underlined how post-synthesis treatments can induce not only a modulation of the composition of the starting materials but also a tuning of their morphological features.

Adsorption and photodegradation experiments

Adsorbent properties of the different materials and their photocatalytic activity under visible light were evaluated towards two dyes: RhB and MO. As previously reported, the inorganic material was dispersed in an aqueous solution of the dye. The suspension was continuously stirred in the dark for 45 minutes to reach the adsorption/desorption equilibrium of the dye on the absorbent material, before proceeding with the irradiation. Then, the degradation of the dye was evaluated by monitoring through UV-Vis spectrophotometry its maximum absorption band: at 554 nm for RhB and 464 nm for MO. The performance were examined evaluating the decoloration efficiency in the solution.

Since thermally treated samples showed a similar behavior, in the following only the activity of samples obtained with the fast procedure (500°C 1h) is discussed.

As shown in Fig. 2.23, a very different behavior was observed for samples subjected to thermal annealing or to UV irradiation, namely the materials characterized respectively by $Bi_{12}O_{17}Cl_2$ and $(BiO)_2CO_3$ as the main phase. In this regard, thermally treated samples displayed similar performances irrespective to the different employed surfactant. Both of them displayed an initial adsorption of 20 % of RhB after 45 minutes in the dark. Then, under irradiation with visible

light, the degradation of 35 % of the organic dye was observed: after a rapid drop in the first few minutes, a low photocatalytic activity was detected. Hence, in 225 minutes this set of samples was able to remove up to 55 % of the dye present in solution thanks both to their absorbent capacity and to photocatalytic activity.

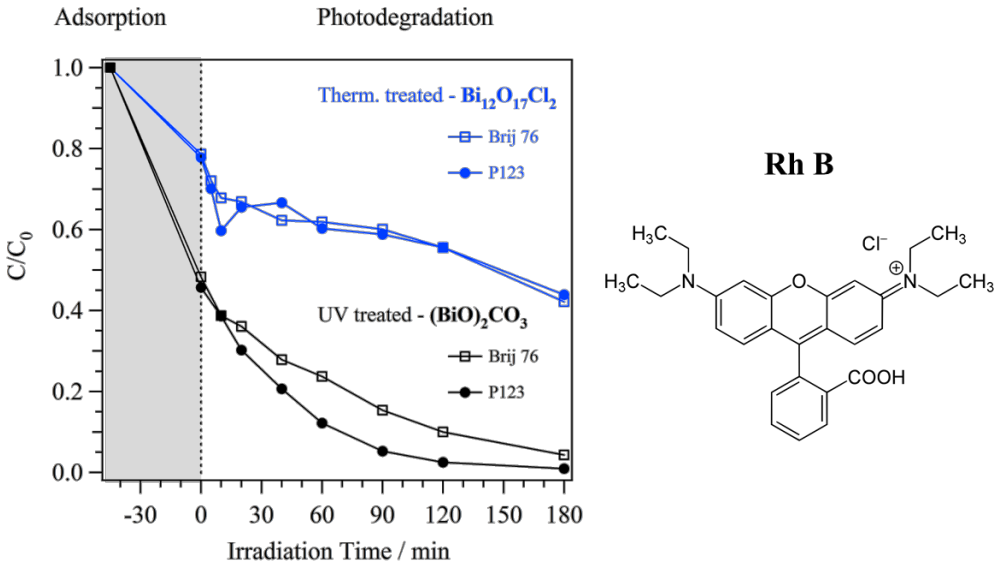

Fig. 2.23 Decoloration efficiency of samples treated 1 h at 500 °C and 14 h with UV (Brij 76 or P123) towards Rhodamine B.

On the contrary, UV treated samples showed a stronger adsorption of RhB, in the order of 50 %. In addition to this initial tendency, under irradiation they were able to degrade all the remaining rhodamine present in solution, in 180 minutes. Among these, as clearly visible in Fig. 2.23, the sample synthesized with P123 was characterized by a faster activity in the first hour of irradiation, which then slowed down for longer times. Thus, although these samples had very similar microstructural, optical properties and surface composition, they displayed a slightly different photocatalytic behavior. However, both of them promoted successfully a complete removal of the cationic dye.

In order to understand the behavior of the material during the initial step of adsorption-desorption equilibrium instauration, the kinetics of adsorption of RhB

in the dark was studied. Results for samples synthesized with Brij 76 were reported in Fig. 2.24.

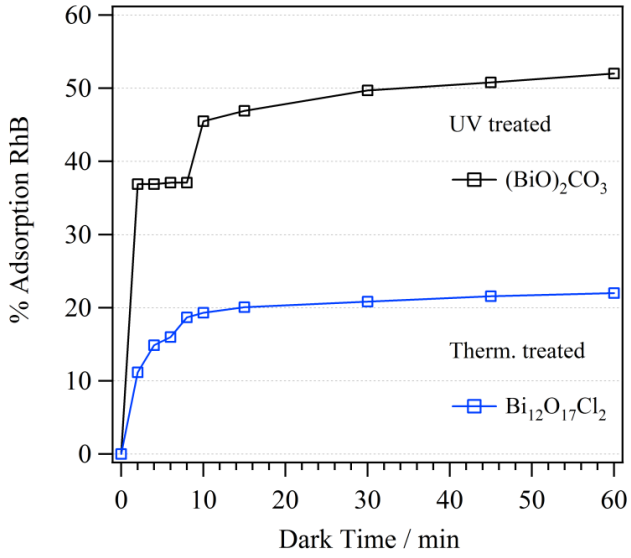

Fig. 2.24 Adsorption of RhB, in the dark, observed for samples treated 1 h at 500 °C and 14 h with UV (Brij 76).

As clearly visible, both samples adsorbed the large majority of the dye in the first ten minutes. In particular, adsorption on $(BiO)_2CO_3$ occurred instantaneously and more than 35 % was removed within two minutes. After few minutes of stabilization, the adsorption process proceeded with a further step. On the contrary, $Bi_{12}O_{17}Cl_2$ displayed a kinetics of adsorption characterized by an exponential profile and also in this case the majority of the dye was removed within 10 minutes.

To further study the interaction between bifunctional nanostructures and dye, the behavior of UV treated samples in presence of methyl orange (MO) was also investigated. MO differs from RhB mainly for its anionic nature and it was usually employed to test the efficiency of the material under investigation towards azo dyes. As shown in Fig. 2.25, this set of samples revealed an even higher tendency to adsorb MO and, depending on the surfactant, they removed from 80 up to 95 % of the dye in 45 minutes of dark. Hence, in presence of the azo dye the bifunctional material performs so efficiently as adsorbent thus limiting the occurrence of photocatalytic processes to remove completely the pollutant.

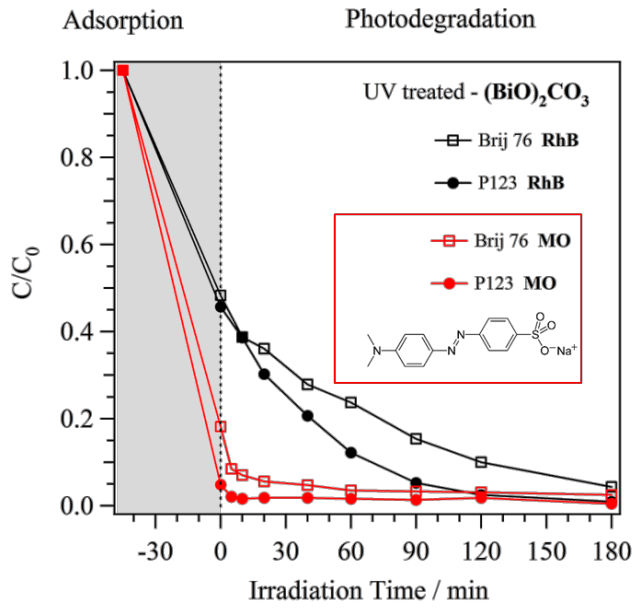

Fig. 2.25 Comparison of the behavior of samples $(BiO)_2CO_3$ towards rhodamine B (RhB) and methyl orange (MO).

By comparing the adsorption behavior of UV treated samples in presence of the two organic dyes with opposite charge, it was interesting to note how in both cases $(BiO)_2CO_3$ nanostructures were able to rapidly adsorbe the dye, with higher preference for MO (Fig. 2.26). In the last case, an exponential adsorption behavior was observed and just after 2 minutes 50 % of methyl orange was removed from the solution as well in 10 minutes over than 70 %.

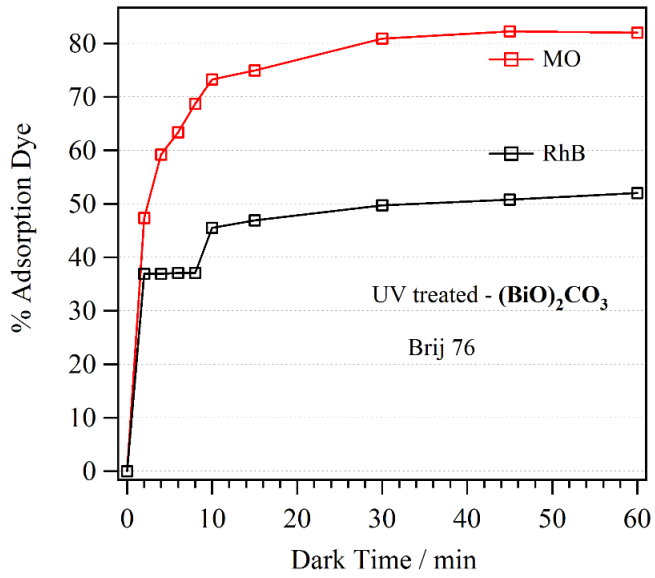

Fig. 2.26 Adsorption of RhB and MO in the dark, samples treated 14 h with UV (Brij 76).

These findings evidenced that this new set of samples displayed interesting performance even though they were characterized by low surface area as the $BiOCl/Bi_{24}O_{31}Cl_{10}$ system previously discussed. Effectively, high surface area values is only one of the desirable requisites to take into account when developing new multifunctional materials for the removal of pollutants. For example, surface charge effects can play a key role influencing the interaction between dye and adsorbent material as well as the effectiveness of the photodegradation. Hence, further investigation on these systems

2.4 Conclusions and perspectives

In summary, development of bismuth oxychloride and subcarbonate nanostructures and their use as bifunctional materials in environmental remediation for adsorption and degradation of organic pollutants under solar irradiation were investigated. Optimization of synthesis conditions (e.g. surfactant, pH and temperature) and different post-synthesis annealing treatments allowed the modulation of composition in terms of Bi/O/X ratios (X = Cl and CO_3) as well as microstructure, morphology and optical properties.

Monophasic BiOCl was obtained by employing a synthesis procedure conducted at low temperature (35 °C) and in neutral conditions. By means of thermal treatments at increasing temperature, the formation of a biphasic $BiOCl/Bi_{24}O_{31}Cl_{10}$ system was induced with a progressive shift of the absorption edge into the visible, up to 500 nm. The two employed structure directing agents, Brij 76 and P123, have led to nanostructures with similar morphology and surface area lower than 10 m^2/g. Similarly, at increasing temperatures of treatment analogous modifications of the morphological features were observed, without a significant variation of the surface area values. The performance of these systems towards adsorption of a model azo-dye (MO) and its photocatalytic degradation under visible irradiation were evaluated. All of them displayed unsufficient activity, since they allowed to remove only 55% of the contaminant in more than 3 hours and a half.

Further investigation was thus conducted in order to obtain a multifunctional material with improved performances, by pursuing two objectives: higher surface area and higher absorption in the visible range. In this regard, beside the optimization of a modified synthesis procedure, post-synthesis treatments were adopted as an additional tool to modulate chemical and physical properties of the inorganic nanostructures. By applying different thermal and UV treatments on the $Bi_2O_2CO_3/Bi_{12}O_{17}Cl_2$ starting material, it was possible to obtain nanostructures with a different relative amount of the two initial phases. Thus, a modification of the microstructural, optical and morphological properties of the materials was

attained and a change on the functional characteristics was observed. The most promising performances were observed for $(BiO)_2CO_3$ nanostructures which were able to adsorb 50 % of RhB and 100% of MO in 30 minutes, acting as highly efficient adsorbents already after few minutes of contact. Subsequently, they were also able to photocatalyze in 180 minutes the degradation of the remaining dye under visible irradiation. In future it will be interesting to clarify different aspects. In particular, the correlation between surface properties of the nanostructures and the nature of their interaction with the dye need to be investigated. Thus, for example, the presence of a different surface charge or the preferential exposition of peculiar crystalline faces in the nanostructures need to be evaluated. The possibility of improving the photocatalytic activity of the materials will be considered by modifying the synthesis procedure through material doping with other halogens and employing different surfactants, in order to obtain diverse morphologies and higher surface area values.

2.5 Instrumental details

Thermogravimetric analysis and temperature programmed oxidation experiments

TGA was performed with a TA Instruments SDT 2960 simultaneous TG/DSC system. The scans were recorded at a heating rate of 10 °C min^{-1} in a temperature range of 30–800 °C. Experiments were performed in air.
In order to verify that the UV-treatment completely remove surfactant residues, a TPO experiment was conducted after the treatment (data not show).

Raman spectroscopy

Micro-Raman experiments were carried out in backscattering geometry at room temperature using an Horiba T64000 triple spectrometer equipped with a Peltier cooled CCD detector (Horiba Synapse). The 514.5 nm line of an argon laser (Spectra Physics Stabilite 2017) was used as excitation source. The laser power at the specimen surface was always kept below 5 mW. Care was taken in order to avoid sample damage due to the interactions with the laser beam. The scattered

radiation was collected through a long working distance 50x microscope objective (Olympus LMPLFLN, 50x/0.50). The spectrograph, equipped with 2400 lines/mm gratings, was used in double subtractive configuration for the low wavenumbers region (5-250 cm^{-1}) measurements or as a single stage in the 70-1000 cm^{-1} range.

Surface area measurements

Specific surface area measurements were obtained from Brunauer, Emmett and Teller (BET) analysis of Kripton adsorption isotherms at liquid nitrogen temperature (ASAP 2020, Micromeritics).

Adsorption and photodegradation experiments

The adsorption ability is one of the important factors to be evaluated in materials for wastewater treatment and it was evaluated as described in the following. In 160 mL of a MO aqueous solution with an initial concentration (C_0) of 6 mg/L were dispersed 200 mg of material (50 mg for RhB) and the suspension was magnetically stirred in the dark. The temperature of suspensions was maintained at 20 °C. At given time intervals, 3 mL aliquots were sampled and filtered through a 0.45 μm Millipore filter, to remove the catalyst. The concentration of the dye in the filtrates was evaluated by recording the absorbance at the maximum of the UV-Vis spectrum of the target molecule (554 nm for RhB and 464 nm for MO) by using a UV–vis spectrometer (Shimadzu UV-2450).
The adsorption capacity efficiency of dyes was calculated from the following equation:

$$\text{Adsorption capacity (mg g}^{-1}) = \frac{(C_0 - C_{eq})V}{m} \qquad \text{Eq. 1}$$

where C_0 and C_{eq} (mg L^{-1}) are concentrations of the dye solution at the initial stage and at the instant t_{eq}= 45 min at which the adsorption-desorption equilibrium is reached; m (g) is the mass of sample, and V (L) is the volume of adsorbate solution.

Photocatalytic properties of the samples were investigated monitoring the degradation of organic dyes, under visible light. The description of the experimental setup is discussed in detail elsewhere[69]. In a typical experiment with MO, 200 mg of the catalyst were dispersed in an aqueous solutions of the dye (1.9 x 10^{-5} M). In the case of RhB, 50 mg of the catalyst and 1.5 x 10^{-5} M of dye were used. Prior to irradiation, the dye/catalyst suspensions were kept in dark for 45 minutes under stirring to ensure an adsorption/desorption equilibrium under ambient condition. At this stage and at increasing time intervals during the irradiation, aliquots of the suspension were withdrawn and filtered through a 0.45 μm Millipore filter to remove the catalyst. The residual dye concentrations in the filtrates were analyzed by UV–Visible spectrophotometer (VARIAN, Cary 2000) at maximum absorption wavelengths (λ_{max}) of 554 and 464 nm for RhB and MO, respectively.

The degradation efficiency of dye was calculated from the following equation:

$$\text{Degradation efficiency (\%)} = \frac{(C_0 - C_t)}{C_0} \times 100 \qquad \text{Eq. 2}$$

where C_0 and C_t (mg L^{-1}) are concentrations of the dye solution at the initial stage and at the t instant ($45 < t < 180$ min), respectively.

2.6 References

(1) Forgacs, E.; Cserháti, T.; Oros, G. *Environment International* **2004**, *30*, 953.

(2) Rai, H. S.; Bhattacharyya, M. S.; Singh, J.; Bansal, T. K.; Vats, P.; Banerjee, U. C. *Critical Reviews in Environmental Science and Technology* **2005**, *35*, 219.

(3) Gupta, V. K.; Suhas *Journal of Environmental Management* **2009**, *90*, 2313.

(4) Bae, J.-S.; Freeman, H. S. *Dyes and Pigments* **2007**, *73*, 81.

(5) Combes, R. D.; Haveland-Smith, R. B. *Mutation Research/Reviews in Genetic Toxicology* **1982**, *98*, 101.

(6) Hatch, K. L. M., Howard *Dyes as Contact Allergens: A Comprehensive Record*., 1999; Vol. 1.

(7) Kuo, W. G. *Water Research* **1992**, *26*, 881.

(8) Walsh, G. E.; Bahner, L. H.; Horning, W. B. *Environmental Pollution Series A, Ecological and Biological* **1980**, *21*, 169.

(9) Karunya, A.; Rose, C.; Valli Nachiyar, C. *World Journal of Microbiology and Biotechnology* **2014**, *30*, 915.

(10) Cheng, L.; Wei, M.; Huang, L.; Pan, F.; Xia, D.; Li, X.; Xu, A. *Industrial & Engineering Chemistry Research* **2014**, *53*, 3478.

(11) Morshedi, D.; Mohammadi, Z.; Akbar Boojar, M. M.; Aliakbari, F. *Colloids and Surfaces B: Biointerfaces* **2013**, *112*, 245.

(12) Zheng, Y.; Yao, G.; Cheng, Q.; Yu, S.; Liu, M.; Gao, C. *Desalination* **2013**, *328*, 42.

(13) You, S.-J.; Damodar, R. A.; Hou, S.-C. *Journal of Hazardous Materials* **2010**, *177*, 1112.

(14) Yue, Q. Y.; Gao, B. Y.; Wang, Y.; Zhang, H.; Sun, X.; Wang, S. G.; Gu, R. R. *Journal of Hazardous Materials* **2008**, *152*, 221.

(15) Raghu, S.; Ahmed Basha, C. *Journal of Hazardous Materials* **2007**, *149*, 324.

(16) Belessi, V.; Romanos, G.; Boukos, N.; Lambropoulou, D.; Trapalis, C. *Journal of Hazardous Materials* **2009**, *170*, 836.

(17) Asuha, S.; Zhou, X. G.; Zhao, S. *Journal of Hazardous Materials* **2010**, *181*, 204.

(18) Wu, R.; Qu, J.; He, H.; Yu, Y. *Applied Catalysis B: Environmental* **2004**, *48*, 49.

(19) Wu, R.; Qu, J.; Chen, Y. *Water Research* **2005**, *39*, 630.

(20) Park, H.; Kim, H.-i.; Moon, G.-h.; Choi, W. *Energy & Environmental Science* **2016**, *9*, 411.

(21) Chang, X.; Wang, S.; Qi, Q.; Gondal, M. A.; Rashid, S. G.; Yang, D.; Dastageer, M. A.; Shen, K.; Xu, Q.; Wang, P. *Applied Catalysis B: Environmental* **2015**, *176–177*, 201.

(22) Ye, L.; Su, Y.; Jin, X.; Xie, H.; Zhang, C. *Environmental Science: Nano* **2014**, *1*, 90.

(23) Wang, W.-K.; Chen, J.-J.; Gao, M.; Huang, Y.-X.; Zhang, X.; Yu, H.-Q. *Applied Catalysis B: Environmental* **2016**, *195*, 69.

(24) Liu, C.; Zhang, A.-Y.; Pei, D.-N.; Yu, H.-Q. *Environmental Science & Technology* **2016**, *50*, 5234.

(25) Pei, D.-N.; Gong, L.; Zhang, A.-Y.; Zhang, X.; Chen, J.-J.; Mu, Y.; Yu, H.-Q. *Nature Communications* **2015**, *6*, 8696.

(26) Cheng, H.; Huang, B.; Dai, Y. *Nanoscale* **2014**, *6*, 2009.

(27) Huang, S.-T.; Jiang, Y.-R.; Chou, S.-Y.; Dai, Y.-M.; Chen, C.-C. *Journal of Molecular Catalysis A: Chemical* **2014**, *391*, 105.

(28) Cao, J.; Li, X.; Lin, H.; Xu, B.; Chen, S.; Guan, Q. *Applied Surface Science* **2013**, *266*, 294.

(29) Mohan, R. *Nat Chem* **2010**, *2*, 336.

(30) Li, Y.; Liu, J.; Jiang, J.; Yu, J. *Dalton Transactions* **2011**, *40*, 6632.

(31) Briand, G. G.; Burford, N. *Chemical Reviews* **1999**, *99*, 2601.

(32) Maile, F. J.; Pfaff, G.; Reynders, P. *Progress in Organic Coatings* **2005**, *54*, 150.

(33) Kijima, N.; Matano, K.; Saito, M.; Oikawa, T.; Konishi, T.; Yasuda, H.; Sato, T.; Yoshimura, Y. *Applied Catalysis A: General* **2001**, *206*, 237.

(34) Ueda, W.; Isozaki, T.; Sakyu, F.; Nishiyama, S.; Morikawa, Y. *Bulletin of the Chemical Society of Japan* **1996**, *69*, 485.

(35) He, G.; Xing, C.; Xiao, X.; Hu, R.; Zuo, X.; Nan, J. *Applied Catalysis B: Environmental* **2015**, *170–171*, 1.

(36) Xiao, X.; Jiang, J.; Zhang, L. *Applied Catalysis B: Environmental* **2013**, *142–143*, 487.

(37) Chang, F.; Luo, J.; Wang, X.; Xie, Y.; Deng, B.; Hu, X. *Journal of Colloid and Interface Science* **2015**, *459*, 136.

(38) Chang, X.; Gondal, M. A.; Al-Saadi, A. A.; Ali, M. A.; Shen, H.; Zhou, Q.; Zhang, J.; Du, M.; Liu, Y.; Ji, G. *Journal of Colloid and Interface Science* **2012**, *377*, 291.

(39) Li, J.; Yu, Y.; Zhang, L. *Nanoscale* **2014**, *6*, 8473.

(40) Wang, Q.; Hui, J.; Huang, Y.; Ding, Y.; Cai, Y.; Yin, S.; Li, Z.; Su, B. *Materials Science in Semiconductor Processing* **2014**, *17*, 87.

(41) Zhang, W.; Zhang, Q.; Dong, F. *Industrial & Engineering Chemistry Research* **2013**, *52*, 6740.

(42) Chen, R.; So, M. H.; Yang, J.; Deng, F.; Che, C.-M.; Sun, H. *Chemical Communications* **2006**, 2265.

(43) Huang, H.; Tian, N.; Jin, S.; Zhang, Y.; Wang, S. *Solid State Sciences* **2014**, *30*, 1.

(44) Huang, H.; Wang, J.; Dong, F.; Guo, Y.; Tian, N.; Zhang, Y.; Zhang, T. *Crystal Growth & Design* **2015**, *15*, 534.

(45) Madhusudan, P.; Yu, J.; Wang, W.; Cheng, B.; Liu, G. *Dalton Transactions* **2012**, *41*, 14345.

(46) Zheng, Y.; Duan, F.; Chen, M.; Xie, Y. *Journal of Molecular Catalysis A: Chemical* **2010**, *317*, 34.

(47) Lu, H.; Xu, L.; Wei, B.; Zhang, M.; Gao, H.; Sun, W. *Applied Surface Science* **2014**, *303*, 360.

(48) Madhusudan, P.; Ran, J.; Zhang, J.; Yu, J.; Liu, G. *Applied Catalysis B: Environmental* **2011**, *110*, 286.

(49) Zhao, M.; Dong, L.; Zhang, Q.; Dong, H.; Li, C.; Tang, H. *Powder Diffraction* **2016**, *31*, 2.

(50) Peng, H.; Chan, C. K.; Meister, S.; Zhang, X. F.; Cui, Y. *Chemistry of Materials* **2009**, *21*, 247.

(51) Jia, Z.; Wang, F.; Xin, F.; Zhang, B. *Industrial & Engineering Chemistry Research* **2011**, *50*, 6688.

(52) Zhang, X.; Ai, Z.; Jia, F.; Zhang, L. *The Journal of Physical Chemistry C* **2008**, *112*, 747.

(53) Zhang, K.-L.; Liu, C.-M.; Huang, F.-Q.; Zheng, C.; Wang, W.-D. *Applied Catalysis B: Environmental* **2006**, *68*, 125.

(54) Armelao, L.; Bottaro, G.; Maccato, C.; Tondello, E. *Dalton Transactions* **2012**, *41*, 5480.

(55) Xia, J.; Yin, S.; Li, H.; Xu, H.; Yan, Y.; Zhang, Q. *Langmuir* **2011**, *27*, 1200.

(56) Wu, S.; Wang, C.; Cui, Y. *Applied Surface Science* **2014**, *289*, 266.

(57) Jiang, J.; Zhao, K.; Xiao, X.; Zhang, L. *Journal of the American Chemical Society* **2012**, *134*, 4473.

(58) Biswas, A.; Das, R.; Dey, C.; Banerjee, R.; Poddar, P. *Crystal Growth & Design* **2014**, *14*, 236.

(59) Ding, C.; Cao, F.; Ye, L.; Liu, K.; Xie, H.; Jin, X.; Su, Y. *Physical Chemistry Chemical Physics* **2015**, *17*, 23489.

(60) He, J.; Wang, J.; Liu, Y.; Mirza, Z. A.; Zhao, C.; Xiao, W. *Ceramics International* **2015**, *41*, 8028.

(61) Selvamani, T.; Gnana Sundara Raj, B.; Anandan, S.; Wu, J. J.; Ashokkumar, M. *Physical Chemistry Chemical Physics* **2016**, *18*, 7768.

(62) Yu, Y.; Hu, Z.; Zhang, Y.; Gao, H. *RSC Advances* **2016**, *6*, 18577.

(63) Shen, K.; Gondal, M. A.; Al-Saadi, A. A.; Li, L.; Chang, X.; Xu, Q. *Research on Chemical Intermediates* **2015**, *41*, 2753.

(64) Gondal, M. A.; Chang, X.; Ali, M. A.; Yamani, Z. H.; Zhou, Q.; Ji, G. *Applied Catalysis A: General* **2011**, *397*, 192.

(65) Kim, W. J.; Pradhan, D.; Min, B.-K.; Sohn, Y. *Applied Catalysis B: Environmental* **2014**, *147*, 711.

(66) Xiao, X.; Liu, C.; Hu, R.; Zuo, X.; Nan, J.; Li, L.; Wang, L. *Journal of Materials Chemistry* **2012**, *22*, 22840.

(67) Moulder, J. F.; Stickle, W. F.; Sobol, P. E.; Bomben, K. D. *Handbook of X-Ray Photoelectron Spectroscopy*; Perkin Elmer Corporation Eden Prairie, MN, USA, 1992.

(68) Strohmeier, B. R. *Applied Surface Science* **1991**, *47*, 225.

(69) Hameed, A.; Montini, T.; Gombac, V.; Fornasiero, P. *Journal of the American Chemical Society* **2008**, *130*, 9658.

(70) Nurgaliev, B. Z.; Popvkin, B. A.; Stefanovich, S. Y. *Russian Journal of Inorganic Chemistry* **1983**, *28*, 2207.

(71) Chen, X. Y.; Huh, H. S.; Lee, S. W. *Journal of Solid State Chemistry* **2007**, *180*, 2510.

(72) Tien, L.-C.; Lin, Y.-L.; Chen, S.-Y. *Materials Letters* **2013**, *113*, 30.

(73) Grice, J. D. *The Canadian Mineralogist* **2002**, *40*, 693.

(74) Lagercrantz, A.; Sillén, L. G. *Arkiv för kemi, mineralogi och geologi* **1947**, *A25*, 1.

(75) Taylor, P.; Sunder, S.; Lopata, V. J. *Canadian Journal of Chemistry* **1984**, *62*, 2863.

(76) Liu, Y.; Wang, Z.; Huang, B.; Yang, K.; Zhang, X.; Qin, X.; Dai, Y. *Applied Surface Science* **2010**, *257*, 172.

Chapter 3. $ZnGa_2O_4:Cr^{3+}$ thin films

3.1 Introduction

3.1.1 $ZnGa_2O_4$

Among oxide-based materials, zinc gallate ($ZnGa_2O_4$) attracted the attention of the scientific community for its versatility in different fields of application. The renewed interest towards materials based on this compound is due to the discovery of new challenging optical properties. This finding opens interesting perspectives in terms of the design of new architectures endowed with innovative luminescence properties and of the comprehension of the correlation between composition, structure, morphology and optical properties in these materials.

$ZnGa_2O_4$ is characterized by a normal spinel structure (AB_2O_4) with a unit cell belonging to the cubic space group F*d3m* in which Zn^{2+} and Ga^{3+} ions occupy respectively tetrahedral (A) and octahedral (B) coordinated sites (Fig. 3.1).[1-3] Tetrahedral sites are characterized by fully T_d symmetry, whereas Ga^{3+} sites belong to the D_{3d} point group and present a sixfold distorted octahedral coordination.[4]

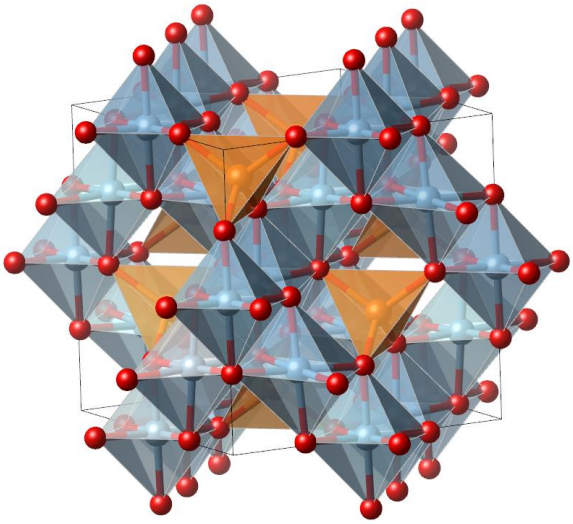

Fig. 3.1 Normal spinel structure: M^{2+} and M^{3+} ions are located in tetrahedral and octahedral coordinated sites, respectively.

As wide band gap semiconductor, zinc gallate is characterized by full transparency in the visible region and a strong absorption in the UV, owing to an optical bandgap in the range of 4.4-4.7 eV (260-280 nm).[5-7] Under excitation by ultraviolet light, a strong blue emission is obtained which arises from self-activated optical centers as octahedral Ga-O groups localized in the spinel lattice.[3,5] Similarly, blue luminescence has been obtained also after excitation by means of low voltage electrons, thus zinc gallate displayed cathodoluminescent properties.[8,9]

As a consequence of these chemico-physical properties, $ZnGa_2O_4$ has been deeply studied starting from the nineties for its possible application in different fields. Firstly, the possibility to obtain thin films has been investigated with the aim to develop electroluminescent devices (TFED), field emission (FED) and vacuum fluorescent displays (VFDs).[9-13] Remarkably, compared to common sulfide-based phosphors, zinc gallate showed better thermal and chemical stability especially under electron bombardment in high vacuum, together with the absence of undesired emission of corrosive gas species containing sulfur.[3,14] Additionally, oxide-based phosphors can be realized by means of more accessible and simple synthesis methods. Further potential applications concern transparent conductive oxides (TCOs) for optoelectronic devices, air-pollution control and gas sensing to photocatalytic degradation of organic pollutants.[5,15-21] Depending on the target application, synthesis of different structures has been developed including powders, nanopowders, films and nanowires. Regarding powders, the most common employed synthesis method consists in conventional oxide solid state reactions starting from ZnO and Ga_2O_3, and employing for several hours heat-treating cycles at temperatures higher than 1000 °C, followed by grinding procedures.[3,22-24] In order to realize nanosized phosphors, wet chemical methods have been developed, which include solution combustion method,[25] citrate-gel method,[26,27] sonochemical,[28] hydrothermal and solvothermal approaches[15,29-33] as well as hybrid (calcination followed by treatment in solution) procedures.[34] The latter, compared to solid state reaction method, allow to achieve a better control on composition and morphology of the phosphors, generally at a relative lower

synthesis temperature and in shorter times. Similarly, a great variety of strategies has been adopted to obtain zinc gallate in form of thin films ranging from sputtering processes,[9,16,35] pulsed laser ablation and deposition,[36,37] aerosol-assisted chemical vapour deposition (AACVD)[38] to hydrothermal and sol-gel methods.[17,28,39-41]

Besides the above-mentioned applications and the variety of available synthesis processes, $ZnGa_2O_4$ represents an interesting solution for the development of innovative functional materials endowed with peculiar luminescence properties. In fact, the possibility of tuning its photo- and cathodoluminescence properties by doping with transition metal or rare-earth ions has stimulated a further interest in the development of new luminescent systems based on zinc gallate. Doping with Mn^{2+} ions, which substitutes Zn^{2+} in tetrahedral sites, allows to obtain materials with bright green luminescence after excitation with UV light (or low voltage electrons), as a consequence of an efficient energy transfer from $ZnGa_2O_4$ host lattice to the doping ions.[12,13,42,43] Moreover, by increasing the dopant concentration and leading to the occupation of octahedral sites by Mn^{2+} ions, a shift of the luminescence to the red region was obtained.[44] Similarly, red phosphors based on zinc gallate were developed by doping with Eu^{3+} ions.[26] Thus, considering the achievable blue, green and red emission, attempts to realize white light emitting phosphors have been also made by means of multiple doping procedures.[28,29]

Finally, over the last few years, there has been an important breakthrough in the development of zinc gallate based materials, which arises from the employment of Cr^{3+} ions as dopant and discloses interesting perspectives for the future.

3.1.2 Development of persistent luminescent materials: state of the art

The term luminescence was first introduced by the German physicist Eilhard Wiedemann in 1888 and it refers to "all those phenomena of light which are not solely conditioned by the rise in temperature" *i.e.* aside from thermal radiation.[45] Thus, in the field of solid-state science, a luminescent material - also named

phosphor - is a solid which is able to convert a specific form of energy into electromagnetic radiation.[46] Since different energy sources may be employed to obtain emission of light, the resulting emitted radiation is consequently defined with a different terminology. In particular, sources as electromagnetic radiation, electron beam, electric voltage, mechanical energy, a chemical reaction and heat give rise to photoluminescence (fluorescence or phosphorescence), cathodoluminescence, electroluminescence, triboluminescence, chemiluminescence and thermoluminescence, respectively. For the sake of clarity, thermoluminescence does not refer to thermal excitation but to stimulation of light emission from a system which was previously excited in a different way, generally by means of electromagnetic radiation.[46] In this framework, a special case of thermoluminescence at a given temperature is represented by persistent luminescence, which in literature is also named afterglow or, in a misleading manner, long-lasting phosphorescence.[47] Persistent luminescence essentially consists in an emission of light for long time (minutes-hours) after the removal of the irradiation (or excitation) source such as gamma rays, X-rays, UV or visible light.[43,48-52] The long emission time of the phenomenon encourages to adopt the term phosphorescence although this is usually employed in the context of luminescence of organic compounds, originated from transitions involving electronic states with different spin multiplicity.[53] On the contrary, the long decay time of persistent luminescence is due to the storage of excitation energy, in the form of electrons and holes, by traps; the subsequent delayed radiative recombination is triggered by thermal energy release of the carriers. For this reason, the appropriate term to be used is thermally stimulated luminescence (TSL) but, for the sake of brevity, in the following it is called persistent luminescence.[47]

Persistent luminescence in synthetic materials is a fascinating phenomenon whose historical roots lie at the beginning of the 17th century, in Italy.[54] In 1603, in Bologna, it was reported for the first time that in absence of any external excitation source a prolonged multi-color luminescence in the dark was observed from synthetic BaS which was obtained upon reduction of mineral barite with

charcoal.[55] Given the low purity of the starting $BaSO_4$ mineral and of the reducing agent, over the years it was clear that the varying color characterizing the persistent emission of the "Bologna stone" was due to different natural impurities within the starting materials.[56] Nevertheless, the mechanism governing the observed phenomenon remained unclear up to the 21th century.[57] In spite of the initial mistrust on a sort of miraculous observation, the interest on this class of materials became concrete in the second half of the last century when they found application in different fields. In particular, sulfide-based materials as ZnS doped with Cu^{2+} and Co^{2+}, or partially substituted with Cd^{2+}, were widely employed in commercial products such as luminous paints, watch dials and glow-in-the-dark-toys.[58,59] However, despite the introduction of further co-dopants, brightness and lifetime of their persistent emission were unsatisfactory and together with a pronounced instability against humidity limited the extension of their application.

A new era started in the mid 1990s when the employment of Eu^{2+} and co-doping with rare earth (R^{3+}) ions determined a breakthrough for the development of modern persistent luminescent materials.[60-62] These findings gave new impulse also to the investigation of the mechanism lying behind the long lasting behaviour and to the research on new possible applications.[63,64] Materials endowed with higher stability and improved long lasting emission properties were obtained by employing mainly aluminates (*e.g.* $SrAl_2O_4:Eu^{2+}$, Dy^{3+}, $CaAl_2O_4:Eu^{2+}$, Nd^{3+}) and disilicates ($M_2MgSi_2O_7:Eu^{2+}$, R^{3+}; M: Ca, Sr) as matrices.[60,65-69] These new materials were commercialized as blue and green persistent phosphors while the development of red long lasting materials represented a further challenge. In fact, the requirements of both strong and long persistent luminescence and chemical stability were more difficult to be achieved for red phosphors. In this framework, moving from sulphides to oxy-sulphide hosts (Y_2O_2S: Eu^{3+}, Mg^{2+}, Ti^{4+}) an improvement of the chemical stability was first achieved but too weak and too short persistent emissions were obtained, compared to the best performing green and blue counterparts.[70,71] In particular, the challenge of combining different RGB elements to realize an efficient white emitting persistent light source seemed fairly problematic to be achieved. Nonetheless, in the last decade a great effort was

devoted to realize red emitting persistent phosphors and the study on a wide variety of hosts was conducted, involving especially silicates, phosphates and titanates.[61,72-80] Moreover, an evolution to non-Eu^{2+} based systems was observed, with a preference on Mn^{2+} and Cr^{3+} as dopant ions.[63,81] As a consequence, beside the discovery of an increasing variety of systems arising from different matrix-dopant combinations, the awareness of the possibility to join a large number of potential applications was a further stimulus to catalyze the research in this field. Indeed, persistent emitting materials may found application in traffic signs, watches, clocks, temperature sensors, emergency signage, textile printing, security ink, latent fingerprint detection, tagging and bioimaging, thus with a great impact on everyday life.[82] More recently, red-NIR persistent emitting materials have gained increasing interest especially for their potential application in night/dark environment vision displays and also for *in vivo* optical imaging.[48,81,83-86] For the former application, red light allows high levels of legibility in low-illuminated environments without affecting the viewers' levels of dark adaptation.[87,88] This could be interesting both for navigation systems, cockpit displays and monitoring instruments as well for security and emergency route signs or traffic signage. On the other hand, the main drawbacks affecting optical imaging in biological samples are related to auto-fluorescence from living tissue under UV illumination and limited optical path length due to the intrinsic absorption and scattering properties of biological media and tissues.[89,90] In order to overcome these problems, the possibility to employ probes endowed with red-NIR long lasting emitting properties represents an interesting solution which permits to operate taking advantage of the tissue transparency window in the NIR I region (650-900 nm), which ensures an increase in detection depth.[89,91,92] Moreover, optical excitation before *in vivo* local or systemic injection and long lasting afterglow allow to obtain an improvement of the signal-to-noise ratio, by limiting the effect of background emission originated from *in situ* excitation.[85] In this context, doping with Mn^{2+} and Cr^{3+} ions guarantees to satisfy the above-mentioned spectral requirements and provide promising performances for bio-imaging.[63] The majority of Mn^{2+}-doped phosphors has been developed employing calcium-

magnesium silicates as hosts ($CaMgSi_2O_6$) and divalent europium together with trivalent lanthanide ions (Eu^{2+}, Ln^{3+}) as co-dopants.[74,93] Recently, interest on Cr^{3+}-doped persistent materials has taken the priority and they have been widely explored for different kinds of applications. Concerning the matrix, $ZnGa_2O_4$ has been employed as preferential host and a dedicated discussion has been devoted in the following paragraph.

3.1.3 $ZnGa_2O_4:Cr^{3+}$

In the field of luminescent materials, Cr^{3+} (d^3) ions represent an interesting solution as dopants because of their potential ambivalent role of functional units and structural probes when embedded in solid matrices. ^4F, ^4P, ^2P, ^2G, ^2D, ^2H and ^2F terms of the isolated Cr^{3+} ion are split into a variety of levels depending on the specific coordination geometry and crystal field strength.[94] The different separation in energy of the resulting levels is reflected on specific spectroscopic features. In particular, Cr^{3+} ions are both optically active and also paramagnetic thus information on their local environment and on the surrounding host lattice can be obtained through optical (absorption and emission) spectroscopy and electron paramagnetic resonance techniques.[95] Hence, together with its peculiar emission properties, Cr^{3+} doping allows to obtain also information on the local symmetry and degree of order/disorder of the nearest-neighbors surrounding the ions itselves.

Within a spinel structure, chromium (III) ions preferentially occupy octahedral sites because of the high ligand field stabilization energy of d^3-systems in an octahedral coordination geometry. Moreover, since the effective ionic radius of Ga^{3+} (0.62 Å) is almost identical to that of Cr^{3+} (0.63 Å), $ZnGa_2O_4$ constitutes an ideal host lattice for chromium ions.[96] Although commonly considered as a normal spinel, $ZnGa_2O_4$ manifests a slight degree of inversion in the order of few percent in site occupancies of zinc and gallium. This inverse structure is characterized by defect points also known as antisite defects where Zn^{2+} ions occupy octahedral sites whereas Ga^{3+} ions occupy tetrahedral sites. According to Kröger–Vink notation, the two possible antisite defects are labelled as Zn'_{Ga} and

$Ga°_{Zn}$ and bear opposite charge.[97] These defect points seem to be fundamental to determine long lasting emitting properties in the chromium doped material, acting as traps for electron-hole pairs. [50, 51,83,98-101]

As a result of the peculiar structure of the host lattice, chromium ions may be localized at least in two sites: an ideal octahedral site surrounded by a regular spinel environment and a slightly distorted octahedral site in the proximity of anti-site defects. Moreover, chromium ions interacting with zinc vacancies or in interstitial positions and Cr^{3+}-Cr^{3+} pairs may be present. Each typology of Cr^{3+} ion contributes to the overall emission properties of the material and its emission spectrum located in the far red region (650-850 nm) presents characteristic bands correlated to the short-range order surrounding the probe ion (R and N lines, see 3.3 Results and Discussion).[102] In 2011 Bessière et al. revealed for the first time the potentiality of $ZnGa_2O_4$: Cr^{3+} as long lasting phosphor.[50] Together with subsequent studies it was observed that chromium persistent luminescence can be stimulated by X-ray, UV and visible illumination; while the emission wavelength is mainly determined by the dopant, its intensity and duration strongly depends by the presence of defects, impurities and codopants.[48,51,99] In fact, the temporary storage of excitation in the form of trapped electrons and holes, the thermal release and radiative recombination of the carriers are regulated by discrete levels due to point defects that act as traps.[51] Many efforts have been made to unravel the role of specific defects on the whole process. Among the others, co-doping with Co^{2+},[103] Al^{3+}, Bi^{3+},[104] Ge^{4+}, Sn^{4+} [43,48,99,105] have been also employed in order to better understand the mechanism governing the persistent behaviour. The optical properties of this class of materials are therefore strictly influenced and correlated to their composition and structure, thus modulation and optimization of the adopted synthesis method plays a key role on the functional properties of the final material. Regarding its potential persistent luminescent properties, chromium doped zinc gallate has been exclusively studied in the form of powder and nanopowder in view of its employment for bio-medical applications.[63,106] In this framework, beside the *ex vivo* excitation of $ZnGa_2O_4:Cr^{3+}$ nanoparticles by UV light before systemic administration, persistent luminescence has been recently

obtained also after *in vivo* visible excitation with an orange/red LED source (λ = 600-650 nm).[84] As a consequence, this finding opens up new possibilities for long-term bioimaging in living animals. Furthermore, from a general perspective, the possibility of a temporary storage of visible light discloses interesting perspectives related to solar energy utilization.[48,51] In this framework, for example, research on different strategies to achieve an enhancement of solar cells efficiency includes the possibility to convert the high energy adsorbed radiation into lower energy photons.[107] This represents a convenient solution in particular when sunlight with short wavelength (UV and blue) is converted to radiation at longer wavelengths, in correspondence of which the spectral response of the solar cell is more sensitive. Moreover, a delayed conversion due to the long lasting behaviour is potentially interesting as solution for the temporary storage of the solar radiation.

An extended study on structure, morphology, composition and optical properties, including persistence, have involved mainly nanopowders obtained by means of solid state method.[25,29,51,83,98,108] Nonetheless, different aspects need to be clarified to get a full comprehension on these systems. Further investigation on different nanostructured systems represents an additional chance to improve the knowledge on this class of materials as well to open up to new potential applications.

To this regard, we developed a soft-chemistry solution method to obtain chromium doped zinc gallate in form of thin films with controlled composition, structure and morphology. An extended characterization was carried on in terms of structural, morphological and compositional properties with a particular focus on their correlation with optical characteristics. This study represents a background research with the aim of exploring the potentiality of chromium doped zinc gallate as luminescent persistent materials in the form of thin films.

3.2 Synthesis

Regarding the realization of oxide-based materials in which luminescence properties arise from a dopant ion, the synthesis by means of a sol-gel process

represents a suitable choice to obtain a good control on the uniform dispersion of the dopant (Appendix A.1).

After an initial screening on precursor and synthesis parameters, the following procedure was adopted. $Ga(NO_3)_3 \cdot xH_2O$ (Sigma Aldrich 99.999%), $Zn(OAc)_2 \cdot 2H_2O$ (Sigma Aldrich 99.999%) and $Cr(NO_3)_3 \cdot 9H_2O$ (Fluka 99.99 %) were employed as metal precursors and used without any further purification. The synthesis was conducted by dissolving the precursors in ethanol:2-methoxyethanol solution 80:20 (V/V) to obtain a total oxide concentration of 40 g/L. Chromium concentration was 0.5 mol % compared to the total M^{3+} content and 0.1 mol% considering the stoichiometry of zinc gallate. The order in which the metal precursors were dissolved was crucial to obtain a stable solution, preventing the rapid precipitation of insoluble zinc oxide/hydroxide products. In fact, when gallium (III) nitrate was firstly dissolved it generated acidic conditions in solution. In this context, the subsequent dissolution of zinc acetate was mediated by partial protonation of acetate groups and, finally, chromium nitrate was added. All precursors contribute to the hydrolysis step bearing crystallization water molecules. At the same time, the employment of 2-methoxyethanol facilitates the dissolution of carboxylate precursors and, taking part to alcohol exchange reactions, it was crucial to slow down the cascade of hydrolysis reactions and prevent early precipitation.[109]

The aging of the solution under stirring at room temperature for 15 h allowed to obtain good wettability towards both silica slides and silicon substrates (100) p-type. The deposition of the films was obtained through spin coating (SCS P6700 Spin-Coater) by means of three successive depositions, with a treatment in air at 130 °C for 10 minutes in between. This step was adopted to induce desorption of water and solvent molecules and with the aim of preserving the deposited layer from the subsequent deposition. After the final deposition, the as prepared films were treated in air for 1h between 400 and 1000°C, and for 5h at 800 °C. These thermal treatments were adopted to consolidate the final material and to promote a transition from the amorphous to a crystalline system.

3.3 Results and Discussion

3.3.1 Microstructure, morphology and composition

Starting from amorphous as prepared thin films, X-ray diffraction analysis (XRD) showed the formation of a crystalline phase after one hour thermal treatment at 500 °C (Fig. 3.2).

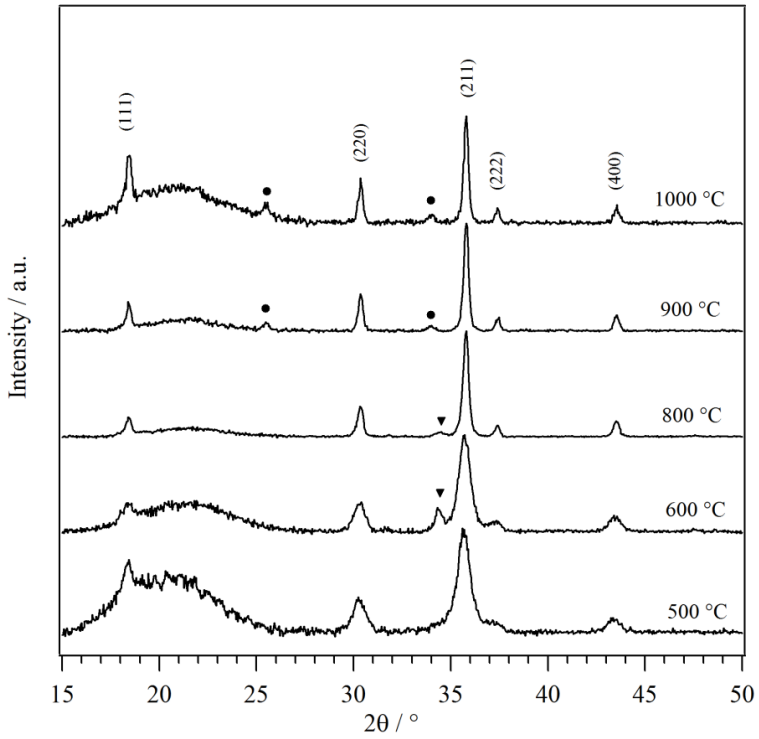

Fig. 3.2 XRD patterns of thin films treated 1h between 500 and 1000°C. Reflexes of the $ZnGa_2O_4$ phase are indexed; ▼ (002) peak of ZnO wurtzite, • silicates.

The visible peaks can be indexed as (111), (220), (211), (222), (400) reflexes of the $ZnGa_2O_4$ phase (JCPDS card. no. 38-1240).[26,31] The peak centered around 34°, observed in samples treated at intermediate temperature (from 600 up to 5h at 800 °C), is compatible with the (002) reflex of ZnO in the wurtzite phase (JCPDS card. no. 79-2205 - ▼ in Fig. 3.2).[110] Upon increasing the treatment temperature in this range, the content of the ZnO secondary phase decreases from 12.6 to 5.6 %, while at temperatures higher than 900 °C wurtzite related peaks are no longer

detectable. Phase compositions were calculated by means of the reference intensity ratio as reported in Appendix (A.2.2). On the contrary, at higher temperature, the formation of silicates is observed due to reactions occurring at the interface between the deposited film and the silica substrate (• in Fig. 3.2). By increasing the treatment temperature, a decrease of the FWHM of zinc gallate peaks was clearly visible pointing out an increase of the crystallites size. An estimation of their average dimensions by means of the Scherrer equation, employing the (211) reflex, indicated a growth from ~20 up to ~50 nm going from samples treated at 500 °C to 1000 °C. Conversely, the duration of the thermal treatment did not induce strong modifications on crystallite dimensions (800 °C 5h, not shown).

Information on the morphology of thin films was obtained by SEM analysis and the effect of the thermal treatments can be well appreciated by the cross section images reported in Fig. 3.3.

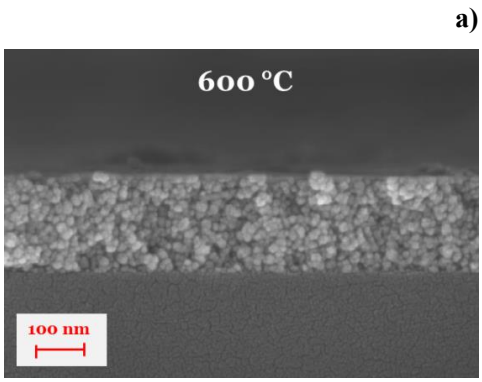

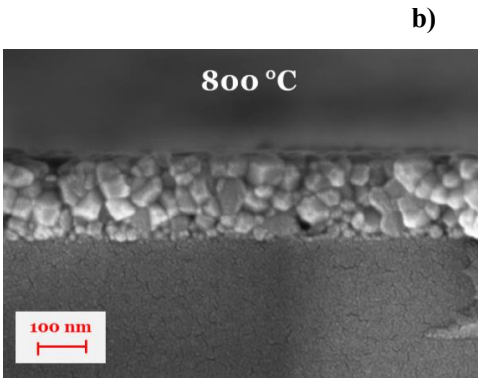

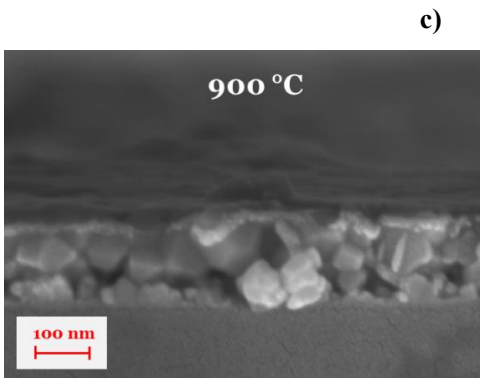

d)

Treatment/°C	As prep	600	800	900
Estimated film thickness / nm	450	220	180	160

Fig. 3.3 a), b) and **c)**: cross section SEM images of films treated 1h at 600 - 900 °C. Estimated film thickness from SEM images as a function of thermal treatments are reported in panel **d)**.

As prepared films were compact and homogeneous and no peculiar morphology was observed by SEM images. On the contrary, thermal annealing induced the formation of grains which were regularly disseminated in the compact layer, characterized by intact homogeneous thickness. The increase of treatment temperatures led to a progressive growth of the mean dimensions of the grains. As clearly visible in Fig. 3.3, samples treated at 600 °C where characterized by the presence of a homogeneous distribution of grains, few tens of nanometers in diameter. Upon increasing the temperature at 800 and 900 °C, the formation of grains with a diameter up to 80 nm was detected. A modification of the grain shape, that became irregular and characterized by a clear exposition of edges, was also observed. Moreover, an increase of the length of the treatment at 800 °C (from 1h to 5h) induced a slight increment of the grain dimensions together with a more compact structure. Finally, by applying treatments at increasing temperature a decrease of the film thickness was also observed: from 450 nm in the as prepared down to 160 nm for the sample treated at 900 °C (see Fig. 3.3, panel d).

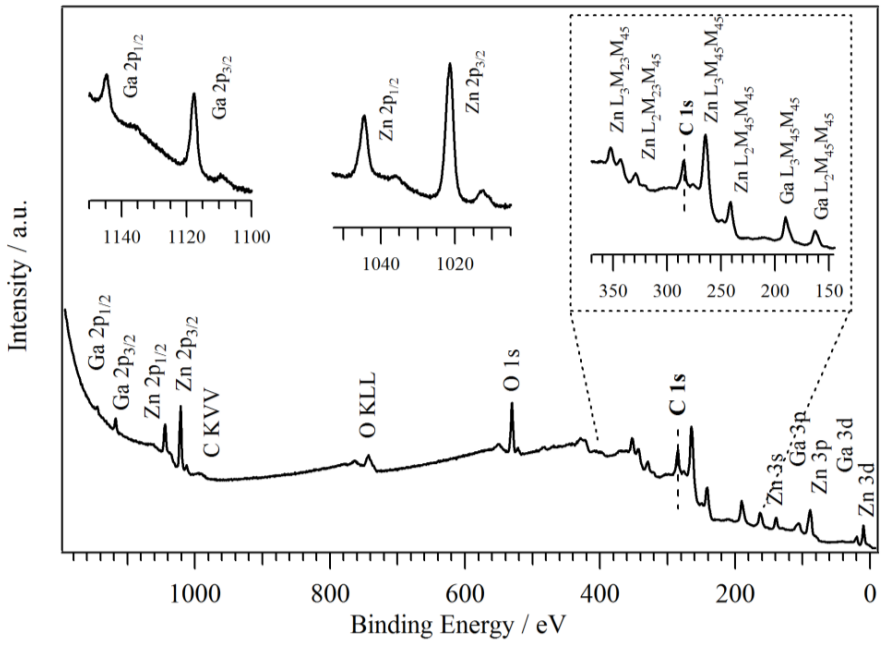

Fig. 3.4 Survey spectrum of the sample treated at 800 °C 1h. In the insets: Ga 2p, Zn 2p, Ga LMM and Zn LMM Auger regions.

The chemical composition of the thin films was investigated by XPS. Independently of the thermal treatment, the extended (survey) spectrum of each sample showed the characteristic Zn, O, Ga and C peaks (as an example, in Fig. 3.4, sample 800°C 1h is reported). Weak signals related to chromium peaks were detected due to the low nominal concentration of this element (~ 0.1 at%) and to its possible segregation. Surface composition actually may differ from that of the underlying layers, thus its comparison with the one of precursor solution is not . In the as prepared samples traces of nitrogen ascribable to the adopted gallium precursor were observed. These signals were no longer detectable after thermal treatments. In detail, in all treated samples the Ga2p signal displayed the typical $2p_{3/2}$ (1117.8 eV) and $2p_{1/2}$ doublet (Δ_{so} = 26.8 eV). Band position and shape were in agreement with the presence of Ga^{3+} species in an oxide matrix (Fig. 3.4 - inset).[111]

Similarly, the Zn2p photoelectron peak showed a doublet (Δ_{so} = 22.9 eV) with the j = 3/2 component centered at a BE value of 1021.7 eV. This was in accordance with the literature values reported for Zn (II) in an oxide environment.[111] In the BE region from 380 to 150 eV, Ga LMM and Zn LMM Auger peaks can be identified together with the C1s peak ascribable to adventitious carbon (BE = 284.8 eV).[111] Finally, the O1s photoelectron peak was centered at 530.3 eV with a shoulder at higher binding energy values (531.8 eV); the two components were attributed to lattice oxygen and residual hydroxyl groups or O^{2-} ions in the surface region, respectively.[16]

Quantitative analysis showed a Ga/Zn ratio well below the nominal value expected for $ZnGa_2O_4$ already in the as prepared sample, which was subjected only to a short low temperature treatment (20 minutes at 130 °C). This feature was observed also in the annealed samples although the Ga/Zn ratio increased from 0.2 at 600 °C up to 1 at 900 °C.

Further information on elemental distribution were obtained by XPS depth profile analysis, reported in Fig. 3.5.

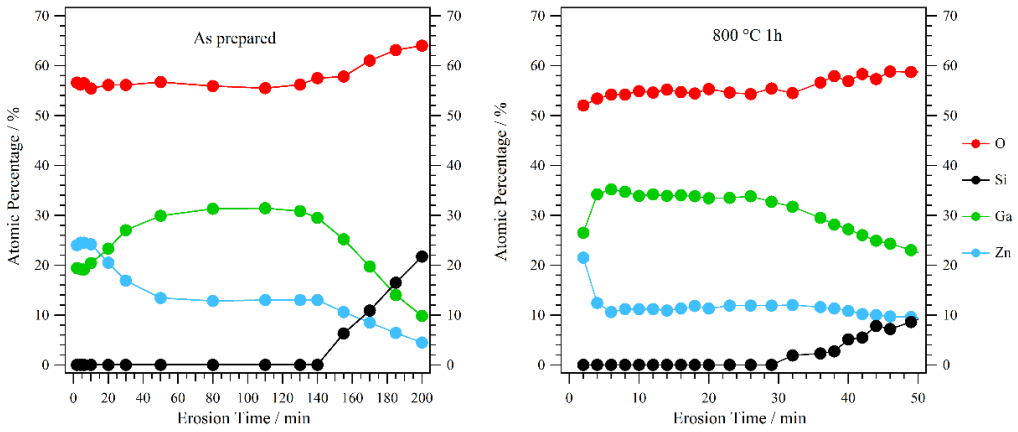

Fig. 3.5 XPS depth profiles of as prepared and annealed samples at 800 °C for 1 h.

Both as prepared and treated samples displayed a rather homogeneous elemental distribution, except in the outermost layers where an excess of zinc content was observed, if compared to the zinc gallate stoichiometry. Zinc, gallium and oxygen related signals were detected in the whole film thickness and their composition was in good agreement with the expected one, *i.e.* Zn 14%, Ga 28% and O 58%.[22] For treatments at increasing temperature, a shorter erosion time was required to reveal silicon signals, in accordance with the lower film thickness observed from SEM analysis. In samples treated at the highest treatment temperatures no silicon signals were observed along the film thickness. Hence, it is reasonable to assume that the crystallized silicates were localized at the interface between film and silica substrate. In conclusion, the observed XPS depth profile distribution suggested a surface segregation of zinc compounds in the first few nanometers likely as zinc oxide.

3.3.2 Optical properties

3.3.2.1 Absorption

Optical absorption and emission properties of specimens were strictly correlated to composition and structural features discussed above.

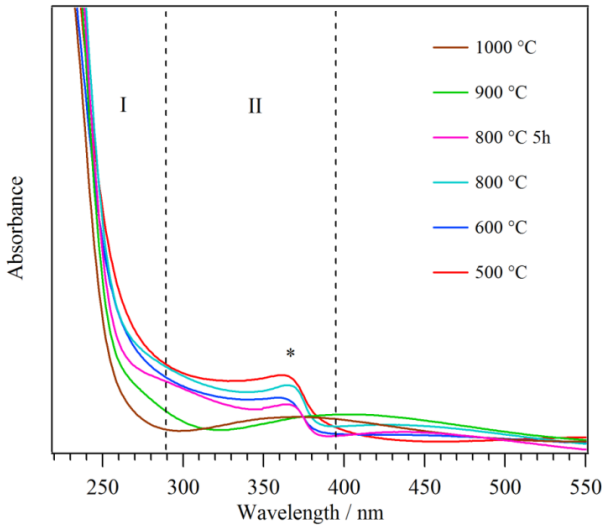

Fig. 3.6 UV-Vis absorption spectra of thin films treated 1h at 600-1000 °C and 5h at 800°C. In evidence (*), the absorption component due to ZnO.

UV-Vis spectra are dominated by the distinctive features of the inorganic matrix. In particular, all annealed samples are characterized by a strong absorption below 280 nm compatible with the optical bandgap (4.4 eV) reported for $ZnGa_2O_4$ (region I - Fig. 3.6).[3,112] Moreover, for samples subjected to thermal treatments at temperature lower than 900 °C a second absorption component is identified at higher wavelengths (region II – Fig. 3.6). This band is well correlated with the presence of ZnO whose band gap is ~ 3.2 eV *i.e.* 388 nm.[113,114] It should be noted that this contribute is observed also in samples treated at the lowest temperature, where crystalline zinc oxide is not detected and XPS analysis evidences a zinc excess at the surface. Intra-shell d-d transitions of Cr^{3+} ions were not detected likely due to its low concentration. These are expected around 300, 420 and 500 nm and correspond to $^4A_2$ (^4F) → $^4T_1$ (^4P), $^4A_2$ (^4F) → $^4T_1$ (^4F) and $^4A_2$ (^4F) → $^4T_2$

(^4F) transitions, respectively.[83] All samples showed high transparency at wavelengths higher than 400 nm. However, interference fringes were detected especially in the spectra of the two specimens annealed at higher temperature, due to characteristic values of the film thickness.

3.3.2.2 Emission

While absorption properties were affected by the characteristic features of the inorganic matrix, the emission spectra were dominated by the peculiar luminescence of the dopant, localized in the red/near-infrared region. In particular, the ^2E (^2G) $\rightarrow$ $^4A_2$ (^4F) transition of Cr^{3+} (d^3 ion) in an octahedral crystal field give rise to a broad emission band ranging from 600 up to 850 nm.[51] The band profile is determined by the overlap of different components which derive from Cr^{3+} ions, within the spinel host lattice, surrounded by an ideal short-range order or located in perturbed coordination sites.[50,51] Thus, doping with Cr^{3+} ions allows to obtain an emission in an interesting spectral window that is influenced by structural changes of the surrounding oxide matrix. Moreover, when the different components of its emission are discernible, Cr^{3+} may be employed as an optical probe (cfr. Paragraph 3.3.2.3).

The structural and morphological modifications induced by thermal treatments at increasing temperature determined remarkable effects on the emission properties of the thin films. As clearly visible in Fig. 3.7a, by exciting charge transfer (CT) bands at 260 nm the chromium emission is scarcely appreciable in samples treated at low temperature (500 °C) while becomes evident at 600 °C. This indicates that, to get an effective emissive contribute of the dopant ion, the formation of a well crystallized matrix and the correlated structural rearrangements were fundamental. Moreover, for treatments at temperature higher than 800 °C a substantial increase of the emission intensity was detected. Hence, the modifications induced by thermal treatments at increasing temperatures resulted in a more efficient energy transfer from the matrix to the dopant ion and favored the prevalence of radiative decay over non-radiative deactivation processes. It is reasonable to suppose that the increment of the average dimensions of the crystalline domains in the zinc

gallate phase may reduce the presence of impurities, defects and grain boundaries which act as killer centers for luminescence. The emission band profile was dominated by the component at lower wavelengths and no apparent changes of its shape were revealed in the different samples.

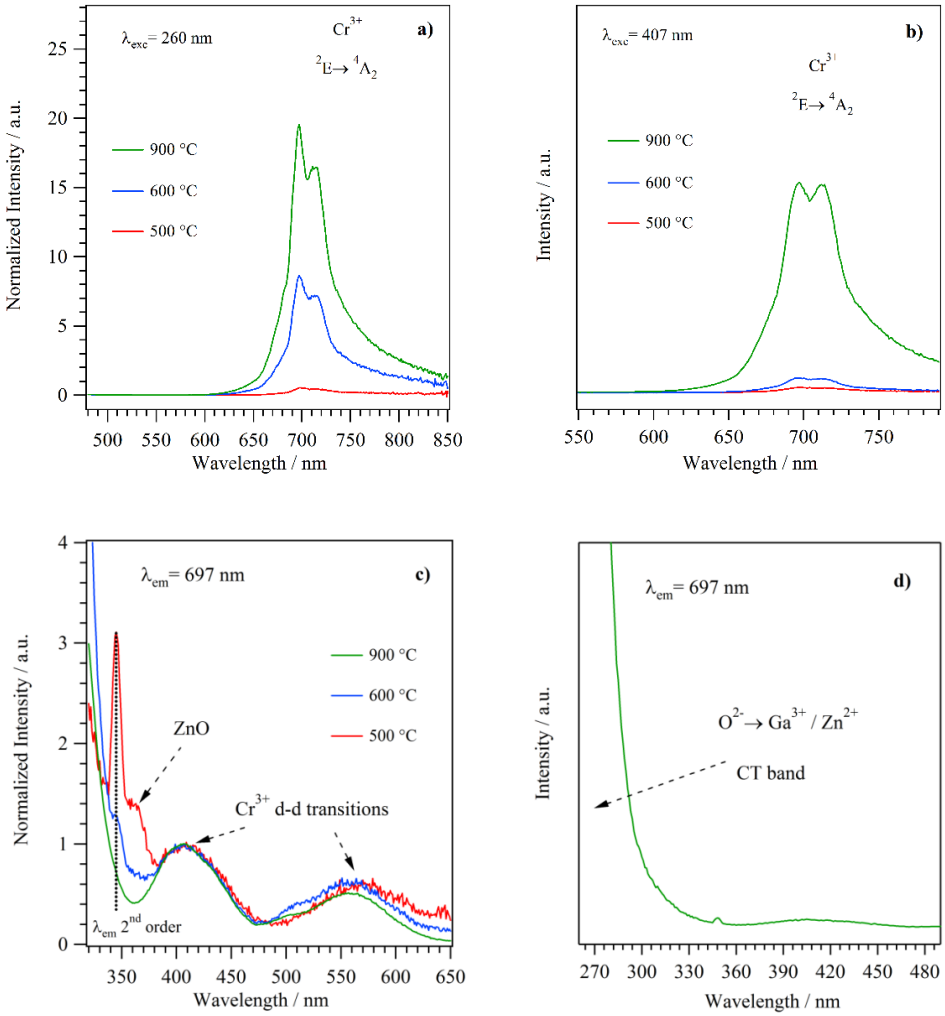

Fig. 3.7 a) and **b)** Emission spectra of treated samples excited at 260 (CT matrix band) and 407 nm (Cr^{3+} transition); **c)** and **d)** excitation spectra obtained monitoring Cr^{3+} emission at λ_{em} = 697 nm.

As a function of the treatment temperature, an analogous trend was observed by exciting directly the Cr^{3+} ion (λ_{exc} = 407 nm), with a more pronounced enhancement of intensity from 600 to 900 °C (Fig. 3.7b). This well documented

the intrinsic sensitivity of Cr^{3+} emission towards the local environment, which was more evident when directly excited. Moreover, it should be noted that, after excitation of Cr^{3+} d-d transitions, the shape of the emission band differs from the one obtained by exciting the matrix. In particular, the component at lower wavelength values decreased becoming comparable to the one at higher wavelength. Hence, a tuning of the excitation wavelength entailed different population of the emitting level of the dopant, depending on the peculiarities of its coordination site.

The excitation spectra obtained monitoring the Cr^{3+} emission at 697 nm are reported in Fig. 3.7c and d. Similar features were observed for the emission component at 715 nm. For all treated samples three main excitation pathways were identified in a wide spectral window ranging from UV to the visible. In the visible range two broad bands associated with the d-d Cr^{3+} transitions, $^4A_2$ (^4F) $\rightarrow$ $^4T_1$ (^4F) and $^4A_2$ (^4F) $\rightarrow$ $^4T_2$ (^4F), and centered at 407 and 550 nm were clearly discernible.[51,108] On the contrary, around 300 nm the Cr^{3+} $^4A_2$ (^4F) $\rightarrow$ $^4T_1$ (^4P) transition was not observed because it was overlapped with the tail of the intense CT bands.[51,105] The latter, whose profile at lower wavelengths ($\lambda < 300$ nm) is reported in Fig. 3.7d, corresponds to the O^{2-} (2p) $\rightarrow$ Ga^{3+}, Zn^{2+} (4s, 4p) transitions. Finally, a further excitation band (366 nm) attributed to ZnO was observed for samples treated at temperature lower than 900 °C. The peculiar emission features connected to this component are evidenced in Fig. 3.8. Upon excitation at 366 nm a broad band centered in the yellow-orange region was observed, which was attributed to different defect related transitions in ZnO. The yellow component is commonly ascribed to interstitial oxygen and residual OH groups whereas the origin of the orange-red emission is likely related to excess oxygen.[115-117] The profile of the excitation spectra obtained by monitoring the emission at 605 nm reflected the component assigned to zinc oxide in the absorption spectra previously discussed (Fig. 3.8). Moreover, for treatments at temperatures higher than 900 °C these features disappeared. The above-mentioned findings were therefore in good agreement with the presence of zinc oxide in samples treated at intermediated temperature, evidenced both by absorption

spectra and XRD analysis (Fig. 3.2 and Fig. 3.6). In addition, it should be noted how optical characterization allowed to detect the presence of zinc oxide in sample treated at low temperatures, although not revealed by microstructural analysis.

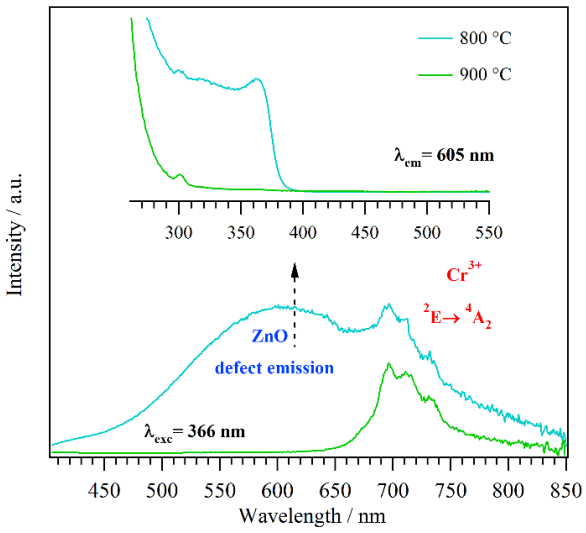

Fig. 3.8 Emission (λ_{exc} = 366 nm) and excitation spectra (λ_{em} = 605 nm).

Further interesting information on modulation of optical properties correlated to microstructural, compositional and morphological modifications was obtained by lifetime measurements of chromium emission. In particular, the different dynamics of the emission upon selective excitation of the matrix (260 nm) or Cr^{3+} (407 nm) was investigated. In both cases, a similar trend was observed as a function of the different thermal treatments: at increasing temperatures more prolonged emissions were observed. This is clearly visible in Fig. 3.9a and b where samples treated at 600 and 900 °C are reported, for λ_{exc} = 260 nm. All the decay curves were fitted with multicomponent exponential functions indicating that, as expected, different emitting Cr^{3+} sites contributed to the overall emission. The decay curve of samples treated at lower temperature reached the background level in less than 400 ms. On the contrary, in samples treated at temperatures

higher than 800 °C the emission decay persists for seconds after the excitation (in Fig. 3.9, 900 °C).

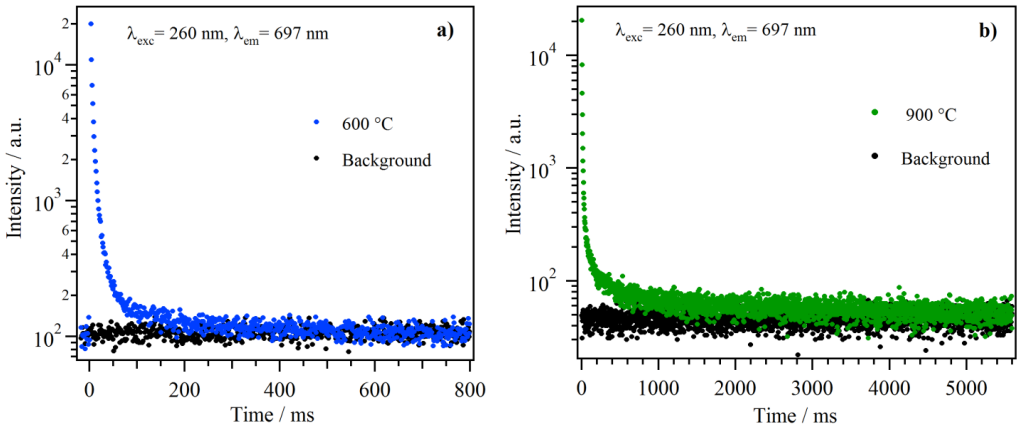

Fig. 3.9 Effect of thermal treatments on lifetime emission. Decay curves of Cr^{3+} emission excited through CT bands (λ_{exc} = 260 nm, λ_{em} = 697 nm) in samples treated at **a)** 600 °C and 900 °C **b)**.

It is therefore interesting to note that samples treated at high temperatures displayed not only the most intense but also the longer red-NIR emission. Hence, the overall optical properties were strictly correlated to the modifications induced by thermal treatments. In particular, microstructural and morphological reorganization may contribute to reduce the presence of killer centers and create local defects which favor the radiative deactivation of the excited states. In this framework, the presence of silicates at the highest treatment temperatures did not apparently affect chromium emission dynamics, since a similar behaviour was observed for samples treated at T ≥ 800 °C. Finally, considering a sample treated at a given temperature, strong differences in the emission dynamics were observed depending on the employed excitation pathway, *i.e.* the matrix or the dopant. In fact, after the direct excitation of d-d Cr^{3+} transitions (λ_{exc} = 407 nm) an emission decay in a shorter time scale compared to the one achieved through CT excitation was obtained (Fig. 3.10). In particular, for the sample treated at 900 °C only few hundreds of milliseconds were required for the end of the decay upon excitation at 407 nm.

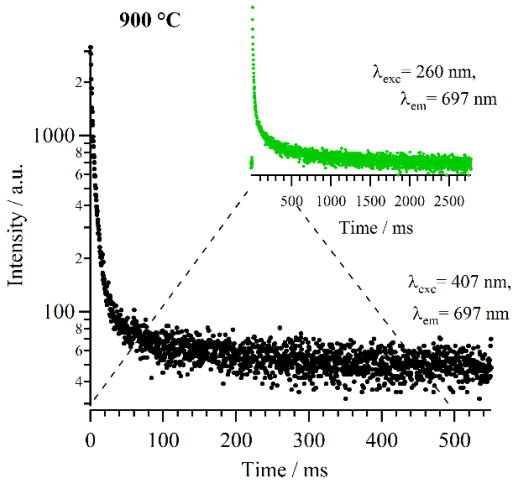

Fig. 3.10 Effect of different excitation wavelengths on excited state lifetime for sample treated at 900 °C. Decay curves for the Cr^{3+} emission excited through CT bands (λ_{exc} = 260 nm) and Cr^{3+} d-d transitions (λ_{exc} = 407 nm).

A similar trend was observed in all samples, thus besides a diverse band profile, the selective excitation of the matrix or the dopant gave rise to different long lasting emitting properties. In particular, excitation through matrix CT bands seems to promote a long-lived chromium emission. This could be correlated to the population of the emitting levels of Cr^{3+} ions in proximity of antisite-defects, as indicated by the peculiar profile of the corresponding emission band.

3.3.2.3 Cr^{3+} emission as temperature probe

As already mentioned, the band profile of Cr^{3+} emission is formed by the convolution of signals arising from chromium ions located in different coordination sites. In particular, R-lines are related to Cr^{3+} ions in unperturbed octahedral sites while N-lines derive from chromium cations surrounded by impurities or host lattice imperfections and they are also known as "structure dependent" N-lines.[102,118,119] Among the latter, N2 lines are specifically correlated to Cr^{3+} ions in coordination sites with neighboring antisite defects, *i.e.* Zn^{2+} ions at Ga^{3+} sites or vice versa. R-lines are characterized by a zero phonon component (R), Stokes (S-PSB) and anti-Stokes phonon side bands (AS-PSB) located

respectively around 690, 708-715 and 660-690 nm (Fig. 3.11a).[50,51,108] The zero phonon line of the N2 transition is located around ~ 696 nm and this component has been recently correlated with charge trapping and recombination processes associated to the long-lasting luminescent properties of this class of materials.[50]

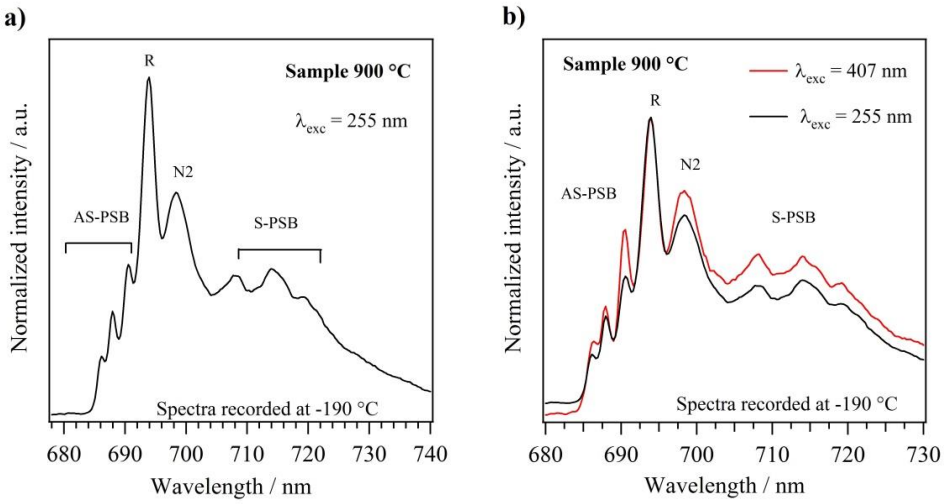

Fig. 3.11 a) Emission spectra at T = -190 °C of sample treated at 900 °C, excited at 255 nm; **b)** comparison with spectra obtained exciting directly the d-d Cr^{3+} transitions (407 nm).

Usually these components are note easily discernible at room temperature as observed in photoluminescence spectra reported in section 3.3.2.2. On the contrary, by recording emission spectra at low temperature it was possible to clearly distinguish the single components. As shown in Fig. 3.11b, at -190 °C all these components were clearly detected upon excitation of both CT bands (at 255 nm) and Cr^{3+} d-d transitions (407 nm). It is worth to note that, in correspondence of a distinct excitation pathway, different relative intensities were observed. In particular, spectra obtained upon excitation of CT were dominated by the R component. Conversely, upon Cr^{3+} direct excitation, AS-PSB, N2 and S-PSB contributes have intensities comparable to those of the zero phonon R-line.

Moreover, by recording emission spectra at increasing operating temperatures, *i.e.* from -190 °C to 250 °C, a strong modification of the Cr^{3+} emission bands was observed. Upon increasing the temperature, a broadening of the whole band was

observed together with a change in the relative intensity of the different components (Fig. 3.12).

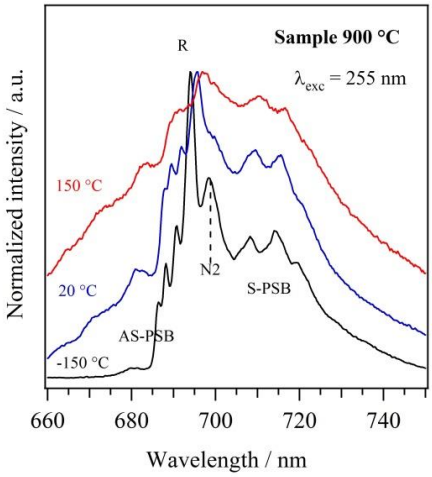

Fig. 3.12 Spectra recorded at increasing temperature showed a different effect on Cr^{3+} emission excited at 255 nm (sample obtained after treatment at 900 °C).

A similar behaviour as a function of temperature was observed in spectra recorded upon excitation of the matrix (CT) and of Cr^{3+} d-d transitions (Fig. 3.13).

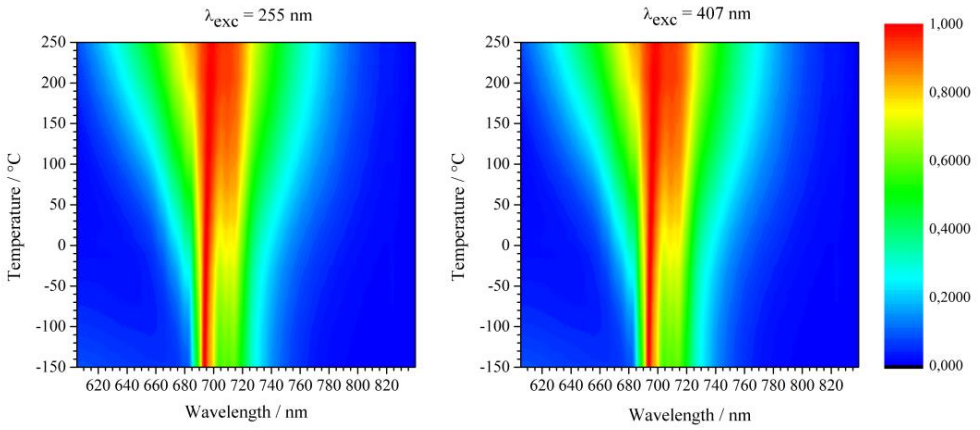

Fig. 3.13 Maps summarizing the trend of Cr^{3+} emission intensity as a function of temperature, excited at 255 nm and 407 nm.

In particular, in Fig. 3.13 are reported two maps obtained by monitoring the emission intensity as a function of both emission wavelength and temperature,

which evidence the behaviour of Cr^{3+} emission in the whole studied temperature range.

Given these evidences on the influence of temperature on chromium emission properties, the possibility to employ this material as a temperature sensor was investigated. In particular, the ratio between the two components (R and S-PSB) of the emission band was defined as the ratiometric parameter (RP) and its variation as a function of the sample temperature was studied.

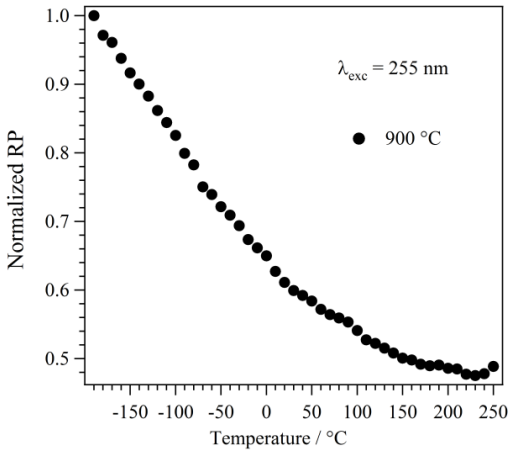

Fig. 3.14 Calibration curve (λ_{exc} = 255 nm) for Cr^{3+}- based luminescence thermometer: variation of the ratiometric parameter (RP) in the range -190÷250 °C for sample treated at 900 °C.

As clearly visible in Fig. 3.14, a continuous decrease of the ratiometric parameter was observed in whole range of investigated temperatures, from -190 up to 250 °C. This trend evidenced the capability of $ZnGa_2O_4:Cr^{3+}$ films to act as luminescence thermometers over a 400 °C temperature range, thus opening new potential applications. It is worth to note that this is a quite wide range for a luminescence thermometer and similar results were obtained for the whole set of samples treated from 600 °C up to 1000 °C.

3.3.3 Local atomic and electronic structure properties: XANES measurements[120-124]

Further information on structural and electronic properties of the system have been obtained by means of X-Ray Near Edge Absorption Spectroscopy (XANES

– Appendix A.6), which provided data complementary to traditional X-Ray diffraction and conventional spectroscopy. In particular, this technique represents a unique local probe, which is chemically selective and insensitive to long range order. It is thus particularly suitable to analyze the local structural organization and its correlation with the functional properties. In fact, near-edge features are sensitive to the specific chemical and structural characteristics of the absorber and therefore they allow to evidence even weak changes of fundamental parameters such as oxidation state, coordination chemistry, local organization and ligand symmetry. Differences between the un-doped and doped sets of samples were also investigated in order to consider the eventual modifications induced on the local structure by the addition of the dopant.

Ga L-edge

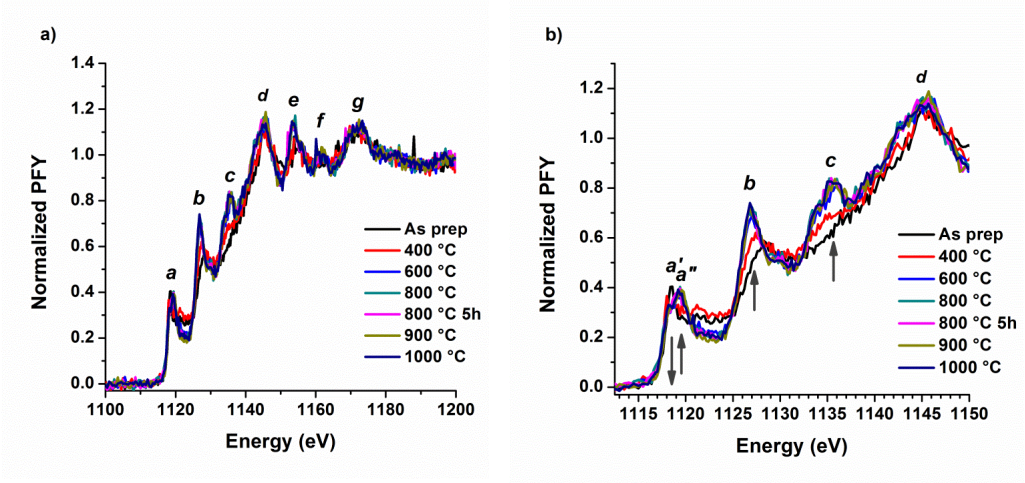

Fig. 3.15 Effect of thermal treatments on PFY at Ga $L_{3,2}$-edge in $ZnGa_2O_4$ samples: **a)** extended spectra, **b)** low energy spectra.

Ga L-edge XANES spectra of un-doped samples are reported in Fig. 3.15 and show the Ga 2p→(4s,4d) dipole transition.[123] Bulk sensitive partial fluorescence yield (PFY) measurements at this edge evidenced signals compatible with gallium in oxidation state +3 and, in nearly all samples, seven clearly discernible peaks in

the 1117-1180 eV energy region (Fig. 3.15a). The main differences pertain the first peaks of the post-edge region, indexed as **a-d** and reported in Fig. 3.15b.

By moving from as prepared samples to specimens treated at temperature higher than 600 °C, peaks at 1127 and 1135 eV (**b** and **c**) become discernible and more intense. In particular, **b** increases with temperature and shifts to lower energies while **c**, clearly visible starting from 600 °C, shows a shoulder at temperatures higher than 800 °C. Moreover, in as prepared samples the lowest energy peak presents a broad shape with a maximum of intensity at 1118 eV (**a′**). After thermal treatments at T > 400 °C, it acquires a narrow shape with the most intense component (**a″**) shifted to higher energy values. Finally, at temperatures higher than 800 °C intensity and band profiles of **a-d** did not change. These observations clearly indicated that after thermal treatments the local structure of gallium undergo substantial modifications from its initial organization in as prepared samples. In particular, the profile of the peak at lower energy (**a′**) in as prepared and 400 °C is similar to the one observed in β-Ga_2O_3 which is characterized by a defect spinel structure where Ga^{3+} ions occupy both tetrahedral and octahedral sites.[121] On the other side, after treatments at 600 °C the peak profile is comparable to that of α-Ga_2O_3 where Ga^{3+} is present only in octahedral coordination.[121] Hence, after treatments at 600 °C gallium ions achieved a local order compatible with the one expected for this element in a regular spinel structure; higher processing temperatures did not perturb this coordination. However, the presence of residual ions in tetrahedral coordination, *i.e.* a slight degree of inversion in the spinel structure, can not be excluded.

Interestingly, the introduction of the dopant did not affect the local environment of gallium and an analogous trend was observed in doped samples as a function of the treatment temperature (Fig.A.2 – Appendix A.6). In this case, the intensity of features **a-d** became constant at temperatures higher than 600 °C, thus starting from a lower temperature compared to undoped samples. These spectra indicated that the employed doping percentage of chromium, which is an ideal substituent of Ga^{3+} in octahedral coordination, does not perturb the local structure of the

majority of gallium ions, suggesting at the same time a homogeneous dispersion of the dopant.

Zn L-edge

In Fig. 3.16 were reported $L_{3,2}$-edge XANES spectra of Zn, which probed electron transitions from Zn 2p to the conduction band of (4s,4d) character.[125] As noted above for gallium, as prepared and 400°C treated samples displayed at the Zn L-edge strongly different features compared to those observed at higher treatment temperatures (Fig. 3.16a). Starting from the as prepared specimen, only two components (**a** and **c**) were clearly visible in the low energy tail of the post-edge region, at 1022 and 1031 eV (Fig. 3.16b). After annealing at 400 °C an intensity decrease of these components was observed, in particular in correspondence of band **a**, together with a shift to lower energy. At the same time, two new components raised up around 1025 and 1034 eV, which were indexed as components **b** and **d**. By increasing the treatment temperature from 600 to 1000 °C, an increment of the intensity of all **a-g** features were observed, with component **a** resulting as a shoulder of the intense component **b**, that along with **e** dominated the whole Zn L-edge XANES spectra (Fig. 3.16a).

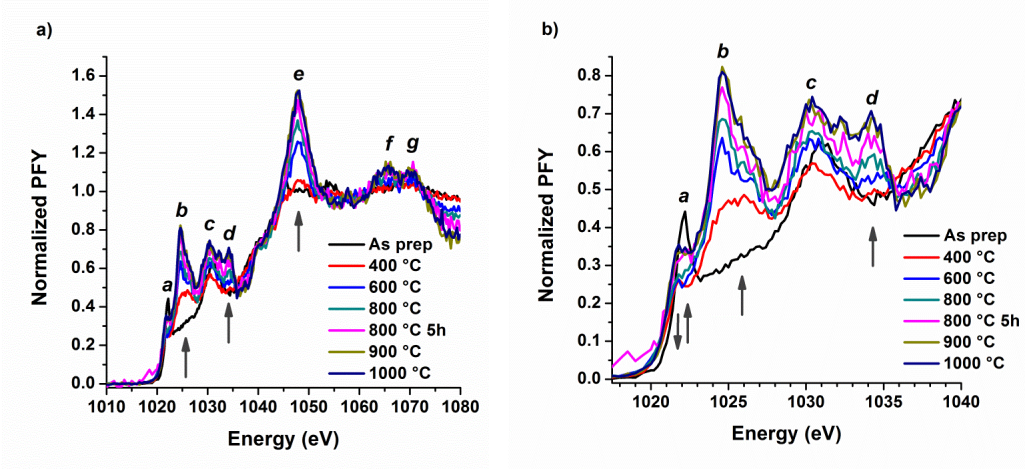

Fig. 3.16 Effect of thermal treatments on PFY at the Zn $L_{3,2}$-edge in $ZnGa_2O_4$ samples: **a)** extended spectra, **b)** low energy spectra.

Hence, contrary to what observed for gallium, zinc local organization underwent modifications in the whole range of adopted temperatures although no substantial differences were observed at 900 °C and 1000 °C. It is interesting to note that these findings can be correlated with the information obtained by microstructural and optical characterizations previously discussed. By moving from untreated to 600 °C samples, XRD evidenced the conversion from an amorphous system to a fully crystallized zinc gallate matrix together with the formation of a minor phase of ZnO. These modifications determined a significant rearrangement of the local zinc surrounding as observed in XANES spectra. Moreover, by increasing the treatment temperature and time, the gradual disappearance of ZnO, evidenced by XRD and by absorption and photoluminescence spectra, led to the presence of Zn^{2+} ions located only in the cubic spinel structure of zinc gallate. Effectively, the near edge part of XANES spectra at T > 600 °C was similar to that of $ZnAl_2O_4$, a regular spinel in which zinc occupies tetrahedral sites as in $ZnGa_2O_4$. However, a distinction between characteristic features of ZnO and $ZnGa_2O_4$ was difficult because of the similar tetrahedral coordination of zinc (II) in both compounds and the bulk sensitivity of the adopted detection mode.

When comparing XANES spectra of doped samples to undoped ones at Zn L-egde, a behaviour analogous to that at Ga L-edge was observed. In fact, chromium doped zinc gallate showed the same trend as $ZnGa_2O_4$ when increasing the treatment temperature, that is, a similar modification of the position and intensity of the different signals. Thus, also the local zinc coordination was not substantially modified by the doping procedure. However, in doped samples minor intensity changes were observed moving from 600 to 1000 °C (Fig. 3.16b and Fig.A.3-Appendix A.6) as compared to undoped specimens.

O K-edge

As for zinc and gallium $L_{3,2}$-edges, also O K-edge spectra, related to the oxygen $1s \rightarrow 2p$ dipole transition, displayed substantial differences when comparing as prepared and low temperature (T = 400 °C) treated samples to those annealed at higher temperature (Fig. 3.17).

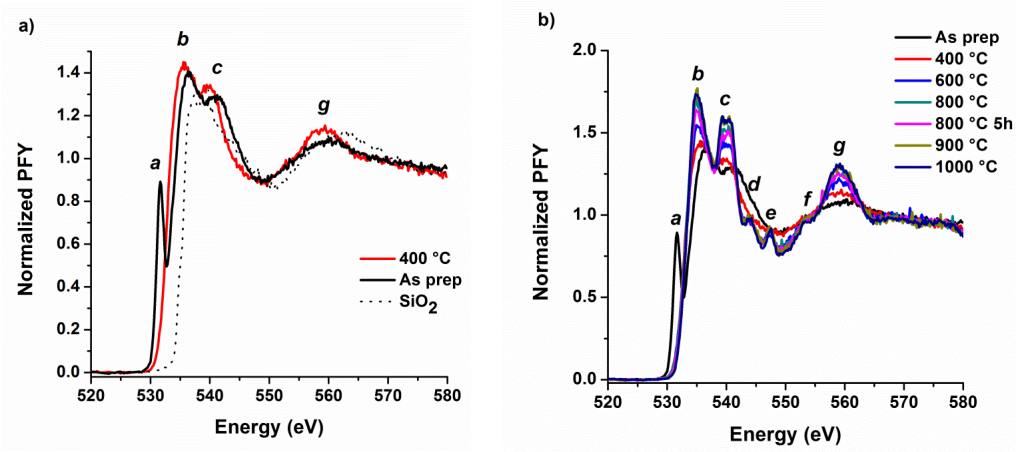

Fig. 3.17 Effect of thermal treatments on PFY at the O K-edge in $ZnGa_2O_4$ samples: **a)** low energy spectra for substrate, as prepared and 400 °C sample and **b)** extended spectra.

In particular, see Fig. 3.17a, as prepared spectra showed a peculiar sharp feature labelled as **a** in proximity of the edge at 531.6 eV and other two peaks at 536.5 and 541 eV (**b** and **c**). The broad feature at higher energy values was instead correlated to a contribute of the silica substrate. After thermal treatment at 400 °C, feature **a**, which may be originated from holes at the O sites, disappeared, peaks **b** and **c** shifted to lower energies and a new peak **g** was detected at 559 eV.[122] These findings indicated the formation of a local environment which closely resemble the one observed in gallium oxide although further features related to oxygen with a coordination geometry similar to zinc oxide may be overlapped and not clearly distinguishable.[122] Upon increasing the treatment temperature from 600 °C to 1000 °C, an intensity increment in peaks **b**, **c** and **g** was observed together with the appearance of three new components **d**, **e** and **f** at 544, 547.5 and 553 eV, which were likely characteristic features of the local organization in zinc gallate. As for zinc and gallium $L_{3,2}$-edges, also in O K-edge spectra no distinction between 900 and 1000 °C treatments was possible and no further peaks correlated to the formation of silicates were distinguishable.

Similarly to what observed at the edges of other elements, doped samples displayed an analogous trend compared to the undoped ones (Fig. 3.18).

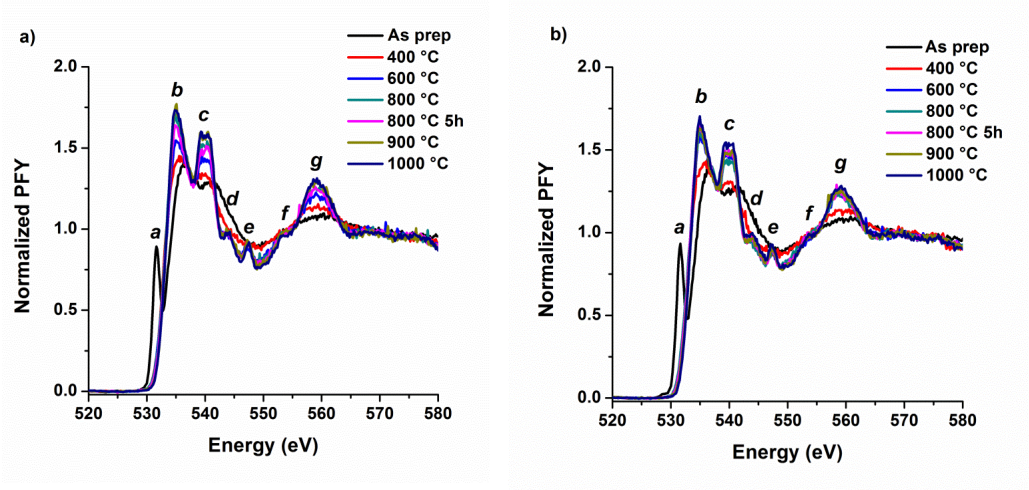

Fig. 3.18 Effect of thermal treatments on PFY at the O K-edge: comparison between $ZnGa_2O_4$ **a)** undoped and **b)** Cr^{3+} doped samples.

In particular, by examining Fig. 3.18a and b, also in this case doped samples showed a minor variation of intensity from 600 °C up to 1000 °C samples. Therefore, in doped samples a local organization similar to the one present at the highest temperature of treatment was obtained already at 600 °C, indicating that the presence of chromium may favour a certain degree of local order.

Cr K-edge

Remarkable information were obtained from analysis of XANES spectra at the Cr K-edge. These data were compared to those reported in literature for chromium located in $ZnGa_2O_4$ powders and in other spinel structures endowed with different percentage of site inversion. In particular, $MgGa_2O_4$ was taken as reference being a near inverse spinel while $ZnAl_2O_4$ as a perfect normal spinel.[126] Interestingly, with the exception of as prepared samples, all spectra of thin films under examination displayed features in good accordance with those reported for chromium K-edge in $ZnGa_2O_4$ powders. In particular, features **b**, **c** and **d** in Fig. 3.19a are located at 6009, 6024 and 6033 eV and well correlated to the 1s→4p dipole transition of chromium (III).[127] For two sets of treatments, 400-600 °C and 800°C (5h)-1000 °C, spectra superimposable were obtained, while the sample

treated at 800 °C showed a different trend. This evidence is in good accordance with spectra at Zn and Ga edges, and it indicates also for chromium a higher degree of organization in correspondence of treatments at the highest temperature values. In this framework, for chromium K-edge, an exception is represented by sample treated at 800 °C which is characterized by lower intensity.

Finally, unlike all the others, as prepared samples displayed also a pre-edge peak around 5993 eV (Fig. 3.19b), which gradually disappeared upon increasing the treatment temperature. This feature was assigned to transitions from 1s to a bound state mainly of 3d character and it was correlated with the presence of chromium (III) hydroxide species and irregular-distorted coordination sites, in agreement with the presence of an amorphous matrix obtained by a solution process.[127-129]

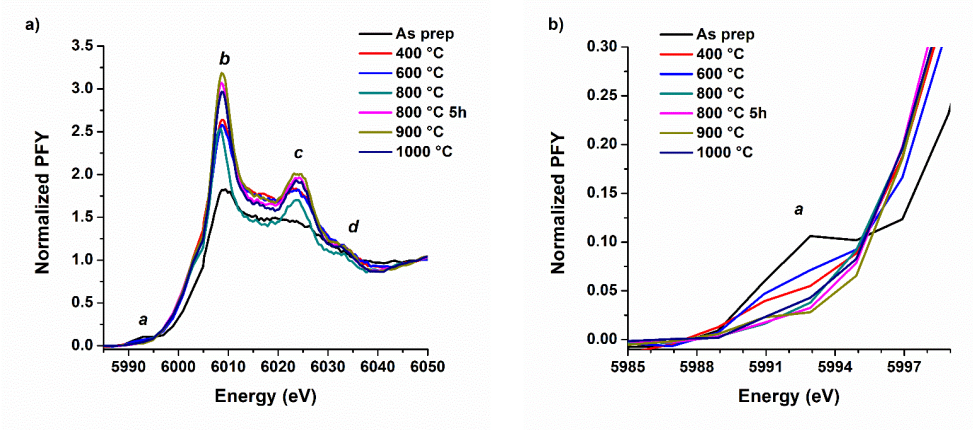

Fig. 3.19 Effect of thermal treatments in $ZnGa_2O_4:Cr^{3+}$ samples on PFY at Cr K-edge: **a)** extended spectra, **b)** low energy spectra.

In summary, XANES spectra indicated that phase-structure transition occurs during the annealing process and samples can be divided mainly into three groups with different local arrangements: i) an initial phase for as prepared samples; ii) an intermediate phase at 400 °C and iii) a final phase at temperature ≥ 600 °C. The intensity of some features in the PFY increased with the annealing temperature when T ≥ 600 °C, indicating a more ordered crystal structure at higher annealing temperatures.

Moreover, although chromium doping was crucial to endow $ZnGa_2O_4$ films with peculiar luminescence properties, it did not change zinc gallate electronic structure at least at this doping amount. In fact, the PFY spectra of chromium doped films showed the same trend at Zn L-edge, Ga L-edge and O K-edge as a function of the treatment temperature.

3.3.4 *Local atomic structure and luminescent properties: XEOL measurements*

X-Ray Excited Optical Luminescence (XEOL) measurements represented a powerful tool to study the correlation between structural and functional properties of luminescent materials. This technique allowed to monitor the emission of optical photons, *i.e*. optical luminescence, after excitation by means of X-Ray radiation. A proper modulation of the excitation source across the absorption edge enabled to excite a specific core level of a certain element; after energy transfer through a cascade of secondary processes, the detected optical emission derived by radiative recombination of electron-hole pairs. The point of strength and, at the same time, the complexity of the technique reside in the fact that different parameters influence the energy conversion of X-rays to optical photons. In particular, de-excitation pathways and dynamics of the whole process are influenced and modulated by the specific composition, structure, morphology, size, crystallinity and defects of the material under study. In this regard, XANES measurements discussed previously supplied preparatory information for the realization and comprehension of the XEOL experiments.

Substrate silica and as prepared samples: O K-edge

In order to discriminate any XEOL contribute originated by the substrate, O-K edge of bare silica slide was examined. As reported in Fig. 3.20, silica substrates displayed two weak emission bands in the visible range: the first centered at 450 nm and the second at 650 nm, correlated to bulk and surface oxygen atoms, respectively.[130] These measurements constituted a blank which was particularly useful to analyse samples treated at low temperature. Effectively, as

prepared samples showed signals which completely matched characteristic features of the substrate and they are not reported in the following. On the contrary, after treatments at 400 °C, emission bands due to the deposited film were also detected.

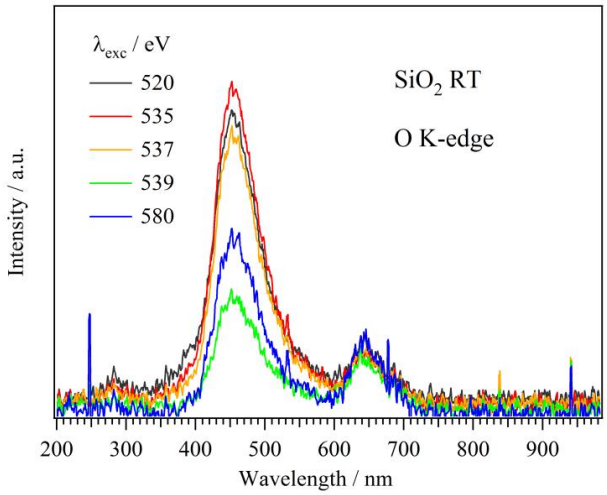

Fig. 3.20 O K-edge XEOL spectra of the bare silica substrate.

$ZnGa_2O_4:Cr^{3+}$ treatment at 400 °C

XEOL spectra were obtained for all treated samples upon excitation across Zn and Ga L-edges as well as O and Cr K-edges. The characteristic features of sample treated at 400 °C are reported in Fig. 3.21. Irrespective of the adopted excitation edges and wavelengths along with the component around 450 nm related to the glass substrate, a further emission band peaked at 696 nm was observed. This feature was compatible with the optical luminescence expected from chromium (III) ions even though no distinct or peculiar components were identified. Upon excitation across O K-edge, the ratio between the red-NIR emission and the band arising from the substrate was higher than the one observed by exciting at Ga and Zn L-edges. In fact, by changing the excitation edge, a different sampling depth was achieved which resulted in a minor or major contribution from the substrate. At O K-edge a shorter sampling depth was expected compared to Zn and Ga (L) excitation because of the lower excitation energy. A minor portion of silica

substrate was thus excited at the oxygen edge. Moreover, considering the XEOL spectra at O-K edge, the significant change in intensity observed for the band arising from the substrate suggested that the film thickness was of the order of magnitude of the penetration depth of soft X-rays at the O K-edge for $ZnGa_2O_4$ (~130 nm).[131]

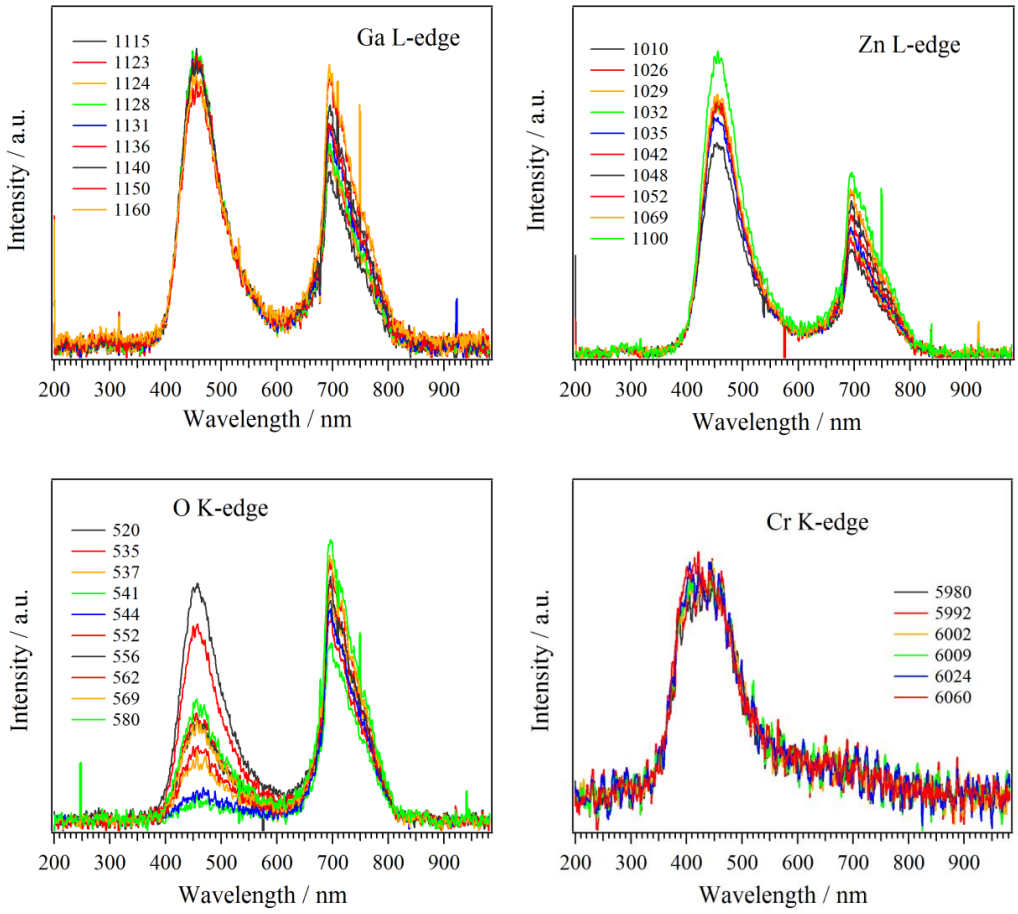

Fig. 3.21 XEOL of $ZnGa_2O_4:Cr^{3+}$ treated at 400 °C: λ_{exc} tuned across Ga and Zn L-edges and O and Cr K-edge.

It is interesting to note how the selective excitation at all elements edges gave rise to the red/NIR emission of chromium, whose emitting levels were hence populated in presence of a not fully crystallized matrix. This represented a substantial difference if compared to the trend observed for UV-excited emission properties, where the characteristic Cr^{3+} luminescence was clearly detected only

starting for treatments at 600 °C. On the contrary, as observed after direct excitation of d-d transition, excitation at Cr K-edge did not give rise to any luminescence, with the exception of the component intrinsic to the silica substrate. Hence, at lower treatment temperatures non radiative de-excitation pathways prevailed when the dopant was excited directly.

$ZnGa_2O_4:Cr^{3+}$ treatment at 600 °C

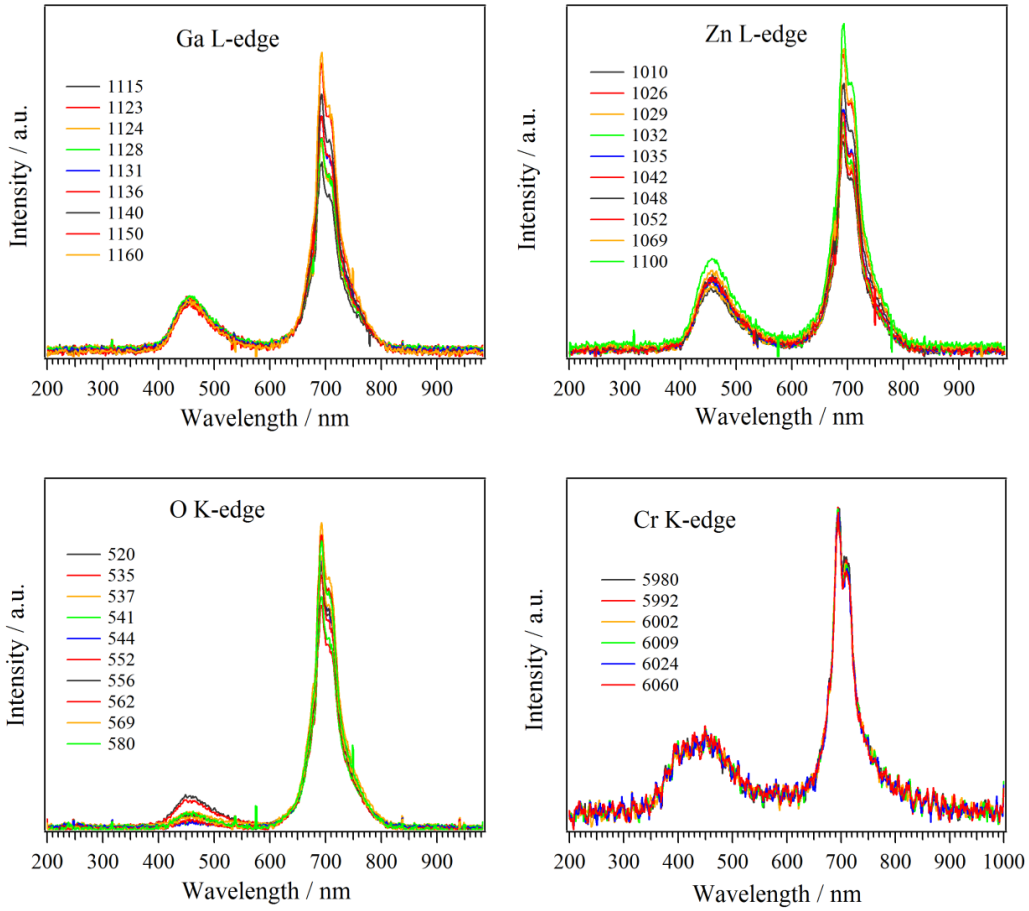

Fig. 3.22 XEOL of $ZnGa_2O_4:Cr^{3+}$ treated at 600 °C: λ_{exc} tuned across Ga and Zn L-edges and O and Cr K-edge.

As previously discussed, an increase of the treatment temperature to 600 °C induced the crystallization of the material leading to higher structural order at the short and the long range. XEOL spectra displayed a rise of the emission intensity

upon increasing the treatment temperature, similarly to what observed upon excitation of charge transfer (CT) bands in the UV range. Unlike for XEOL spectra at 400 °C, the band profile of the chromium emission at 600 °C was characterized by a sharp peak with a maximum at 694 nm and a shoulder at higher wavelengths (Fig. 3.22). In addition, the contribution of the silica substrate became less evident and it was clear that after excitation at Ga, Zn (L) and O (K) edges conversion of X-Rays to optical photons became more efficient. Lastly, at this treatment temperature, the characteristic Cr^{3+} luminescence was detected also upon excitation of the dopant K-edge.

$ZnGa_2O_4:Cr^{3+}$ treatment at 800 °C

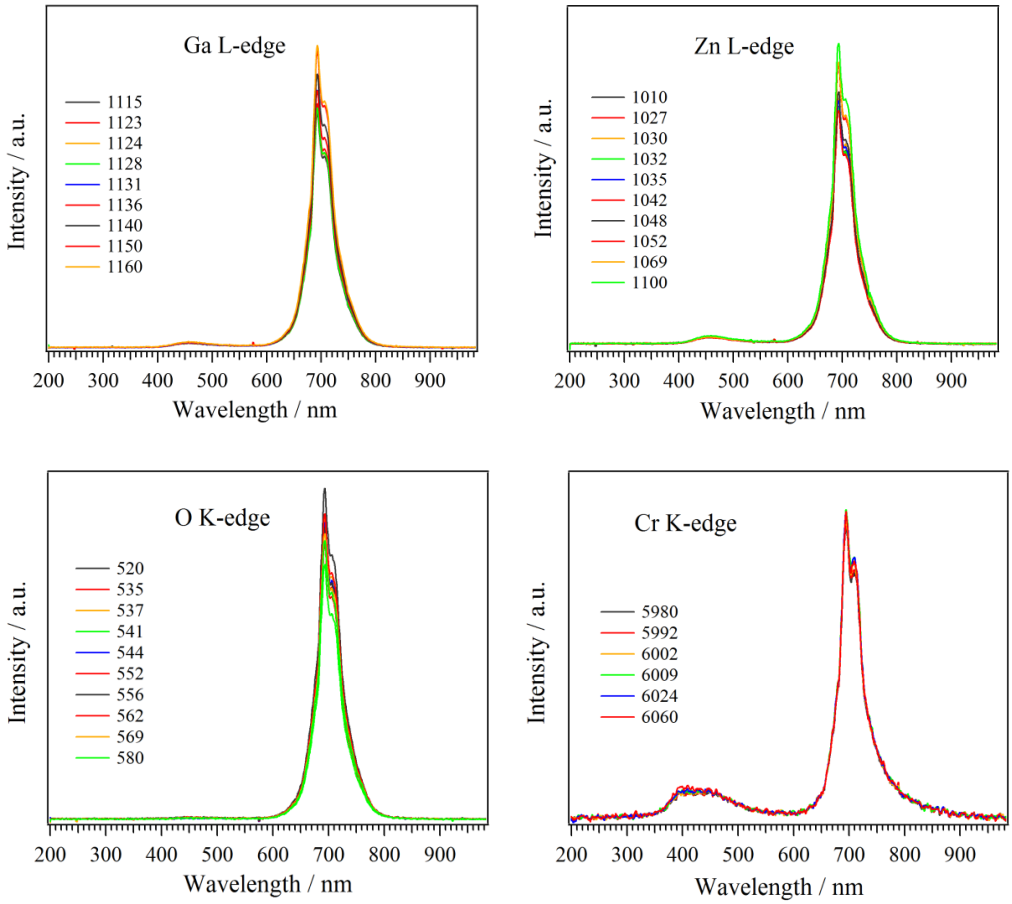

Fig. 3.23 XEOL of $ZnGa_2O_4:Cr^{3+}$ treated at 800 °C: λ_{exc} tuned across Ga and Zn L-edges and O K-edge.

In samples treated at 800 °C, an improvement of the red/NIR emission intensity was observed in XEOL spectra obtained upon excitation at all elements edges (Fig. 3.23). As a consequence, for these specimens the substrate contribution became less visible. Irrespective of the employed excitation wavelength, similar band profiles were observed for chromium emission, which did not differ from those detected for samples treated at 600 °C. It is worth to note that nor the previous sample (600 °C) neither the 800 °C treated one displayed any characteristic feature of ZnO, although its presence in these samples was evidenced by previous characterization (XRD, conventional absorption and emission, XPS). XEOL spectra of ZnO may present a sharp UV peak around 380 nm (band-gap emission) and a broad emission located in the visible region which is correlated to the radiative recombination of electrons and holes located in different bulk and surface defects such as oxygen and zinc vacancies.[115,132,133] The presence of these two components and their relative intensity are strongly correlated to morphology, composition and existence of peculiar defects.[116,132] Spectra reported in Fig. 3.23 were instead dominated by chromium emission and none of zinc oxide bands were visible, even upon magnification of the region of interest. This is explained taking into account that zinc oxide was present in a small amount and mainly localized in the outermost surface region of the specimen and that fluorescence is bulk sensitive.

$ZnGa_2O_4:Cr^{3+}$ treatments at 900 and 1000 °C

Band profile and intensity of chromium emission displayed no substantial differences at the highest treatment temperatures compared to spectra of samples treated at 800 °C. The only exception was related to the contribution of the substrate which became more visible likely due to the reduction of the film thickness. These differences were more easily appreciable in samples treated at 1000 °C, see Fig. 3.24. Moreover, beside the substrate emission band, a further component at lower wavelength values (350 nm) was detected. This component was slightly visible also at 900 °C, it became evident in samples treated at 1000 °C and it may be correlated to the presence of zinc-gallium silicates generated by

the reaction of the deposited film with the substrate. On the contrary, this band was not visible in XEOL spectra obtained upon excitation across Cr K-edge.

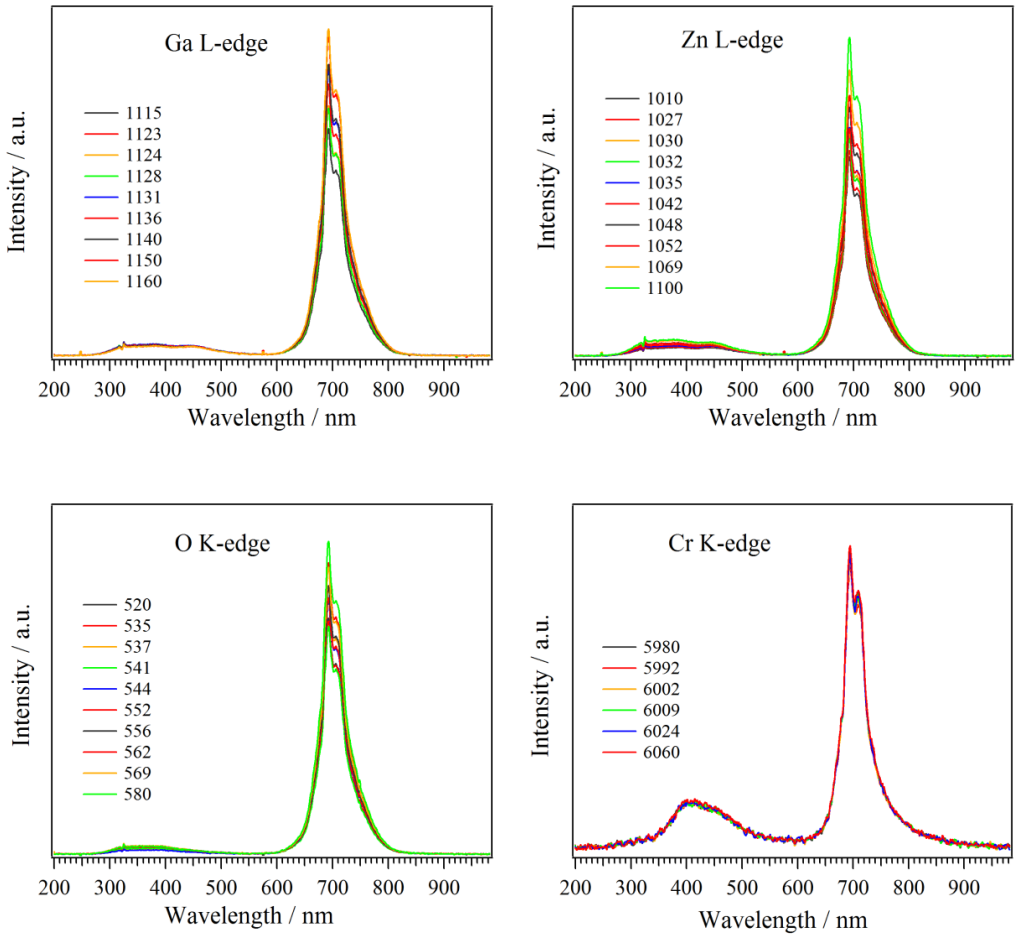

Fig. 3.24 XEOL of $ZnGa_2O_4:Cr^{3+}$ treated at 1000 °C: λ_{exc} tuned across Ga and Zn L-edges and O K-edge.

In summary, upon excitation at Zn L, Ga L and O K-edges, $ZnGa_2O_4:Cr^{3+}$ samples annealed at T ≥ 400 °C were characterized by XEOL signals located in the red-NIR region. On the contrary, excitation across Cr K-edge gave rise to the characteristic Cr^{3+} luminescence only starting from samples annealed at 600 °C. In both cases, an increment of the annealing temperature led to an increase of the emission intensity, evidencing an enhancement of the efficiency of X-rays to optical photons conversion, in correspondence of the formation of a better

crystallized matrix. When the annealing temperature reached 900 °C, a new peak appeared at 360 nm in zinc, gallium and oxygen edges, which is likely correlated to the presence of zinc-gallium silicates.

It is worth to note that the discussion of these data was partly limited by the absence of specific literature references for XEOL in zinc gallate based materials.

3.4 Conclusions and Perspectives

Development of red/NIR long persistence luminescent materials in the form of thin films by means of soft-chemistry solution processes represents nowadays a challenge from different points of view. Firstly, the possibility to realize this class of materials through a sol-gel method allows to obtain a fine tuning on composition, morphology and microstructure, which represents a crucial requirement for the design of materials with controlled functional properties. Secondly, a comprehensive study of optical, compositional, microstructural and morphological properties of chromium doped zinc gallate thin films constitutes a further step towards the understanding of the influence of parameters and factors that governs the mechanism at the basis of long lasting luminescence, providing crucial information for the future development of systems with improved performances. Finally, the realization of red-NIR persistent phosphors in the form of thin films potentially leads to an enlargement of the scope of their application, allowing their deposition on substrates of different nature and form, in which long lasting emission may be improved or integrated by the intrinsic properties of the support.

In this framework, the developed synthesis procedure allowed the formation of thin films constituted mainly by the $ZnGa_2O_4$ crystalline phase and characterized by a highly homogeneous thickness. Thermal treatments at increasing temperature induced substantial modulation of their composition, morphology and microstructure, leading to a red/NIR luminescent emission that persists up to several seconds after excitation through CT bands. Moreover, in correspondence of intermediate treatments, a minor phase of ZnO was detected, which was essentially localized on the surface of the specimens. In particular, it will be

interesting to clarify if zinc oxide may act as protective layer, thus subtracting the underlying zinc-gallate film to the contact of impurities, defects and grain boundaries characteristic of the surface, which generally act as luminescence killer centers. Preliminary results showed that, by employing a defective initial concentration of the zinc acetate precursor (10 % lower than the nominal required), single phase $ZnGa_2O_4$ was obtained and no other phases were observed for analogous thermal treatments in the range of 600-900 °C.

Interestingly, $ZnGa_2O_4:Cr^{3+}$ thin films displayed emitting properties which were strongly influenced by temperature. These findings point out the effectiveness of these materials to act as temperature sensors thus opening further perspectives for future investigations.

Finally, additional study on composition and correlation between microstructure and functional properties will be conducted also taking into account the possibility to employ co-dopants. This will allow to achieve a better comprehension on the different parameters that govern the mechanism of long lasting luminescence and to design materials with improved performances.

3.5 References

(1) Wells, A. F. *Structural Inorganic Chemistry* London, 1975.

(2) Zhang, W.; Zhang, J.; Li, Y.; Chen, Z.; Wang, T. *Appl. Surf. Sci.* **2010**, *256*, 4702.

(3) Jeong, I.-K.; Park, H. L.; Mho, S.-i. *Solid State Commun.* **1998**, *105*, 179.

(4) Xu, L.; Su, Y.; Zhou, Q.; Li, S.; Chen, Y.; Feng, Y. *Cryst. Growth Des.* **2007**, *7*, 810.

(5) Omata, T.; Ueda, N.; Ueda, K.; Kawazoe, H. *Appl. Phys. Lett.* **1994**, *64*, 1077.

(6) Yi, S. S.; Kim, I. W.; Park, H. L.; Bae, J. S.; Moon, B. K.; Jeong, J. H. *J. Cryst. Growth* **2003**, *247*, 213.

(7) Lee, Y. E.; Norton, D. P.; Park, C.; Rouleau, C. M. *J. Appl. Phys.* **2001**, *89*, 1653.

(8) Itoh, S.; Toki, H.; Sato, Y.; Morimoto, K.; Kishino, T. *J. Electrochem. Soc.* **1991**, *138*, 1509.

(9) Hsieh, I. J.; Chu, K. T.; Yu, C. F.; Feng, M. S. *J. Appl. Phys.* **1994**, *76*, 3735.

(10) Minami, T.; Kuroi, Y.; Takata, S. *J. Vac. Sci. Technol., A* **1996**, *14*, 1736.

(11) Minami, T.; Maeno, T.; Kuroi, Y.; Takata, S. *Jpn. J. Appl. Phys.* **1995**, *34*, L684.

(12) Shea, L. E.; Datta, R. K.; Brown, J. J. *J. Electrochem. Soc.* **1994**, *141*, 2198.

(13) Tran, T. K.; Park, W.; Tomm, J. W.; Wagner, B. K.; Jacobsen, S. M.; Summers, C. J.; Yocom, P. N.; McClelland, S. K. *J. Appl. Phys.* **1995**, *78*, 5691.

(14) Vecht, A.; Smith, D. W.; Chadha, S. S.; Gibbons, C. S.; Koh, J.; Morton, D. *J. Vac. Sci. Technol., B* **1994**, *12*, 781.

(15) Liu, L.; Huang, J.; Cao, L.; Wu, J.; Fei, J.; Ouyang, H.; Yao, C. *Ceram. Int.* **2013**, *39*, 3165.

(16) Zhong, Z. Y.; Yang, C. Y.; Gu, J. H. *Appl. Mech. Mater.* **2012**, *143-144*, 199.

(17) Zhang, W.; Zhang, J.; Chen, Z.; Wang, T. *Catal. Commun.* **2009**, *10*, 1781.

(18) Zhang, R.; Villanueva, A.; Alamdari, H.; Kaliaguine, S. *Catal. Commun.* **2008**, *9*, 111.

(19) Chen, C.; Li, G.; Liu, Y. *Powder Technol.* **2015**, *281*, 7.

(20) Chen, X.; Xue, H.; Li, Z.; Wu, L.; Wang, X.; Fu, X. *J. Phys. Chem. C* **2008**, *112*, 20393.

(21) Yan, S. C.; Ouyang, S. X.; Gao, J.; Yang, M.; Feng, J. Y.; Fan, X. X.; Wan, L. J.; Li, Z. S.; Ye, J. H.; Zhou, Y.; Zou, Z. G. *Angew. Chem. Int. Ed.* **2010**, *49*, 6400.

(22) Phani, A. R.; Santucci, S.; Di Nardo, S.; Lozzi, L.; Passacantando, M.; Picozzi, P.; Cantalini, C. *J. Mater. Sci.* **1998**, *33*, 3969.

(23) Kim, J. S.; Kang, H. I.; Kim, W. N.; Kim, J. I.; Choi, J. C.; Park, H. L.; Kim, G. C.; Kim, T. W.; Hwang, Y. H.; Mho, S. I.; Jung, M.-C.; Han, M. *Appl. Phys. Lett.* **2003**, *82*, 2029.

(24) Palmer, G. B.; Poeppelmeier, K. R. *Solid State Sciences* **2002**, *4*, 317.

(25) Lee, J.-H.; Park, H.-J.; Yoo, K.; Kim, B.-W.; Lee, J. C.; Park, S. *J. Eur. Ceram. Soc.* **2007**, *27*, 965.

(26) Yu, M.; Lin, J.; Zhou, Y. H.; Wang, S. B. *Mater. Lett.* **2002**, *56*, 1007.

(27) Wu, S.-h.; Cheng , H.-C. *J. Electrochem. Soc.* **2004**, *151*, H159.

(28) Dutta, D. P.; Ghildiyal, R.; Tyagi, A. K. *J. Phys. Chem. C* **2009**, *113*, 16954.

(29) Zhang, Y.; Wu, Z.; Geng, D.; Kang, X.; Shang, M.; Li, X.; Lian, H.; Cheng, Z.; Lin, J. *Adv. Funct. Mater.* **2014**, *24*, 6581.

(30) Lu, M.; Ouyan, X.; Wu, S.; Ge, R.; Xu, R. *Appl. Surf. Sci.* **2016**, *364*, 775.

(31) Yuan, Y.; Du, W.; Qian, X. *J. Mater. Chem.* **2012**, *22*, 653.

(32) Hirano, M.; Imai, M.; Inagaki, M. *J. Am. Ceram. Soc.* **2000**, *83*, 977.

(33) Hirano, M. *J. Mater. Chem.* **2000**, *10*, 469.

(34) Zou, L.; Xiang, X.; Wei, M.; Li, F.; Evans, D. G. *Inorg. Chem.* **2008**, *47*, 1361.

(35) Kim, Y. J.; Jeong, Y. H.; Kim, K. D.; Kang, S. G.; Lee, K. G.; Han, J. I.; Park, Y. K.; Cho, K. I. *J. Vac. Sci. Technol., B* **1998**, *16*, 1239.

(36) Shi, Q.; Wang, C.; Zhang, D.; Li, S.; Zhang, L.; Wang, W.; Zhang, J. *Thin Solid Films* **2012**, *520*, 6845.

(37) Mini Krishna, K.; Nisha, M.; Reshmi, R.; Manoj, R.; Asha, A. S.; Javaraj, M. K. *Mater. Forum* **2005**, *29*, 243.

(38) Knapp, C. E.; Manzi, J. A.; Kafizas, A.; Parkin, I. P.; Carmalt, C. J. *ChemPlusChem* **2014**, *79*, 1024.

(39) Kurz, A.; Aegerter, M. A. *Thin Solid Films* **2008**, *516*, 4513.

(40) Sei, T.; Nomura, Y.; Tsuchiya, T. *J. Non-Cryst. Solids* **1997**, *218*, 135.

(41) Park, K.-W.; Yun, Y.-H.; Choi, S.-C. *J. Electroceram.* **2006**, *17*, 263.

(42) Shea, L. E.; Datta, R. K.; Brown, J. J. *J. Electrochem. Soc.* **1994**, *141*, 1950.

(43) Abdukayum, A.; Chen, J.-T.; Zhao, Q.; Yan, X.-P. *J. Am. Chem. Soc.* **2013**, *135*, 14125.

(44) Liu, J.; Duan, X.; Zhang, Y.; Jiang, H. *J. Phys. Chem. Solids* **2015**, *81*, 15.

(45) Wieldmann, E. *Annalen der Physik* **1888**, *34*, 446.

(46) Blasse, G.; Grabmaier, B. C. *Luminescent Materials*; Springer-Verlag: Berlin, 1994.

(47) Brito, H. F.; Hölsä, J.; Laamanen, T.; Lastusaari, M.; Malkamäki, M.; Rodrigues, L. C. V. *Opt. Mater. Express* **2012**, *2*, 371.

(48) Pan, Z.; Lu, Y.-Y.; Liu, F. *Nat. Mater.* **2012**, *11*, 58.

(49) Chenu, S.; Veron, E.; Genevois, C.; Garcia, A.; Matzen, G.; Allix, M. *J. Mater. Chem. C* **2014**, *2*, 10002.

(50) Bessière, A.; Jacquart, S.; Priolkar, K.; Lecointre, A.; Viana, B.; Gourier, D. *Opt. Express* **2011**, *19*, 10131.

(51) Bessière, A.; Sharma, S. K.; Basavaraju, N.; Priolkar, K. R.; Binet, L.; Viana, B.; Bos, A. J. J.; Maldiney, T.; Richard, C.; Scherman, D.; Gourier, D. *Chem. Mater.* **2014**, *26*, 1365.

(52) Srivastava, B. B.; Kuang, A.; Mao, Y. *Chem. Commun.* **2015**, *51*, 7372.

(53) Lakowicz, J. R. *Principles of Fluorescence Spectroscopy*; Springer, 1983.

(54) Newton Harvey, E. *A History of Luminescence: From the Earliest Times until 1900*; Am. Phil. Soc.: Philadelphia, 1957.

(55) Licetus, F. *Litheosphorus Sive de Lapide Bononiensi*; Università di Bologna: Bologna, 1640.

(56) Hölsä, J. *Electrochem. Soc. Interface* **2009**, *18*, 42.

(57) Lastusaari, M.; Laamanen, T.; Malkamäki, M.; Eskola, K. O.; Kotlov, A.; Carlson, S.; Welter, E.; Brito, H. F.; Bettinelli, M.; Jungner, H.; Hölsä, J. *Eur. J. Mineral.* **2012**, *24*, 885.

(58) Feldmann, C.; Jüstel, T.; Ronda, C. R.; Schmidt, P. J. *Adv. Funct. Mater.* **2003**, *13*, 511.

(59) Smet, P. F.; Moreels, I.; Hens, Z.; Poelman, D. *Materials* **2010**, *3*, 2834.

(60) Matsuzawa, T.; Aoki, Y.; Takeuchi, N.; Murayama, Y. *J. Electrochem. Soc.* **1996**, *143*, 2670.

(61) Van den Eeckhout, K.; Smet, P. F.; Poelman, D. *Materials* **2010**, *3*, 2536.

(62) Aitasalo, T.; Dereń, P.; Hölsä, J.; Jungner, H.; Krupa, J. C.; Lastusaari, M.; Legendziewicz, J.; Niittykoski, J.; Stręk, W. *J. Solid State Chem.* **2003**, *171*, 114.

(63) Singh, S. K. *RSC Adv.* **2014**, *4*, 58674.

(64) Liu, Y.; Tu, D.; Zhu, H.; Chen, X. *Chem. Soc. Rev.* **2013**, *42*, 6924.

(65) Lin, Y.; Tang, Z.; Zhang, Z.; Wang, X.; Zhang, J. *J. Mater. Sci. Lett.* **2001**, *20*, 1505.

(66) Dorenbos, P. *J. Electrochem. Soc.* **2005**, *152*, H107.

(67) Yamamoto, H.; Matsuzawa, T. *J. Lumin.* **1997**, *72*, 287.

(68) Lin, Y.; Nan, C.-W.; Zhou, X.; Wu, J.; Wang, H.; Chen, D.; Xu, S. *Mater. Chem. Phys.* **2003**, *82*, 860.

(69) Liu, B.; Shi, C.; Yin, M.; Dong, L.; Xiao, Z. *J. Alloys Compd*. **2005**, *387*, 65.

(70) Wang, X.; Zhang, Z.; Tang, Z.; Lin, Y. *Mater. Chem. Phys*. **2003**, *80*, 1.

(71) Hong, Z.; Zhang, P.; Fan, X.; Wang, M. *J. Lumin*. **2007**, *124*, 127.

(72) Wang, X.-J.; Jia, D.; Yen, W. M. *J. Lumin*. **2003**, *102–103*, 34.

(73) Abreu, C. M.; Silva, R. S.; Valerio, M. E. G.; Macedo, Z. S. *J. Solid State Chem*. **2013**, *200*, 54.

(74) Bessière, A.; Lecointre, A.; Priolkar, K. R.; Gourier, D. *J. Mater. Chem*. **2012**, *22*, 19039.

(75) Gong, Y.; Wang, Y.; Xu, X.; Li, Y.; Xin, S.; Shi, L. *Opt. Mater*. **2011**, *33*, 1781.

(76) Wang, J.; Wang, S.; Su, Q. *J. Mater. Chem*. **2004**, *14*, 2569.

(77) Lecointre, A.; Bessière, A.; Bos, A. J. J.; Dorenbos, P.; Viana, B.; Jacquart, S. *J. Phys. Chem. C* **2011**, *115*, 4217.

(78) Bessiere, A.; Lecointre, A.; Benhamou, R. A.; Suard, E.; Wallez, G.; Viana, B. *J. Mater. Chem. C* **2013**, *1*, 1252.

(79) Jia, W.; Jia, D.; Rodriguez, T.; Evans, D. R.; Meltzer, R. S.; Yen, W. M. *J. Lumin*. **2006**, *119–120*, 13.

(80) Lian, S.; Qi, Y.; Rong, C.; Yu, L.; Zhu, A.; Yin, D.; Liu, S. *J. Phys. Chem. C* **2010**, *114*, 7196.

(81) Zhuang, Y.; Katayama, Y.; Ueda, J.; Tanabe, S. *Opt. Mater*. **2014**, *36*, 1907.

(82) Liu, Y.; Lei, B. In *Phosphors, Up Conversion Nano Particles, Quantum Dots and Their Applications*Liu, R.-S., Ed.; Springer: 2016; Vol. 2.

(83) Sharma, S. K.; Bessière, A.; Basavaraju, N.; Priolkar, K. R.; Binet, L.; Viana, B.; Gourier, D. *J. Lumin*. **2014**, *155*, 251.

(84) Maldiney, T.; Bessière, A.; Seguin, J.; Teston, E.; Sharma, S. K.; Viana, B.; Bos, A. J. J.; Dorenbos, P.; Bessodes, M.; Gourier, D.; Scherman, D.; Richard, C. *Nat. Mater*. **2014**, *13*, 418.

(85) le Masne de Chermont, Q.; Chanéac, C.; Seguin, J.; Pellé, F.; Maîtrejean, S.; Jolivet, J.-P.; Gourier, D.; Bessodes, M.; Scherman, D. *Proceedings of the National Academy of Sciences* **2007**, *104*, 9266.

(86) Liang, Y.-J.; Liu, F.; Chen, Y.-F.; Wang, X.-J.; Sun, K.-N.; Pan, Z. *Light Sci Appl*. **2016**, *5*, e16124.

(87) Mantiuk, R.; Rempel, A. G.; Heidrich, W. *Proceedings of the 6th Symposium on Applied Perception in Graphics and Visualization (ACM APGV)* **2009**, 53.

(88) Allan G. Rempel, R. M., Wolfgang Heidrich *19th Color and Imaging Conferences Final Program and Proceedings* **2011**, 191.

(89) Bashkatov, A. N.; Genina, E. A.; Kochubey, V. I.; Tuchin, V. V. *J. Phys. D: Appl. Phys.* **2005**, *38*, 2543.

(90) Frangioni, J. V. *Curr. Opin. Chem. Biol.* **2003**, *7*, 626.

(91) Smith, A. M.; Mancini, M. C.; Nie, S. *Nat Nano* **2009**, *4*, 710.

(92) Weissleder, R. *Nat Biotech* **2001**, *19*, 316.

(93) Maldiney, T.; Lecointre, A.; Viana, B.; Bessière, A.; Bessodes, M.; Gourier, D.; Richard, C.; Scherman, D. *J. Am. Chem. Soc.* **2011**, *133*, 11810.

(94) Sugano, S.; Tanabe, Y.; Kamimura, H. *Multiplets of Transition-Metal Ions in Crystals* London, 1970.

(95) Kahan, H. M.; Macfarlane, R. M. *J. Chem. Phys.* **1971**, *54*, 5197.

(96) Shannon, R. D.; Prewitt, C. T. *Acta Crystallogr. Sect. B: Struct. Sci.* **1969**, *25*, 925.

(97) Kröger, F. A.; Vink, H. J. In *Solid State Physics*; Frederick, S., David, T., Eds.; Academic Press: 1956; Vol. Volume 3, p 307.

(98) Gourier, D.; Bessière, A.; Sharma, S. K.; Binet, L.; Viana, B.; Basavaraju, N.; Priolkar, K. R. *J. Phys. Chem. Solids* **2014**, *75*, 826.

(99) Allix, M.; Chenu, S.; Véron, E.; Poumeyrol, T.; Kouadri-Boudjelthia, E. A.; Alahraché, S.; Porcher, F.; Massiot, D.; Fayon, F. *Chem. Mater.* **2013**, *25*, 1600.

(100) Basavaraju, N.; Priolkar, K. R.; Gourier, D.; Sharma, S. K.; Bessière, A.; Viana, B. *PCCP* **2015**, *17*, 1790.

(101) Hill, R. J.; Craig, J. R.; Gibbs, G. V. *Phys. Chem. Miner.* **1979**, *4*, 317.

(102) Mikenda, W.; Preisinger, A. *J. Lumin.* **1981**, *26*, 53.

(103) Duan, X.; Liu, J.; Wu, Y.; Yu, F.; Wang, X. *J. Lumin.* **2014**, *153*, 361.

(104) Zhuang, Y.; Ueda, J.; Tanabe, S. *J. Mater. Chem. C* **2013**, *1*, 7849.

(105) Yang, J.; Liu, Y.; Yan, D.; Zhu, H.; Liu, C.; Xu, C.; Ma, L.; Wang, X. *Dalton Trans.* **2016**, *45*, 1364.

(106) Sharma, S. K.; Gourier, D.; Teston, E.; Scherman, D.; Richard, C.; Viana, B. *Opt. Mater.* **2016**.

(107) Huang, X.; Han, S.; Huang, W.; Liu, X. *Chem. Soc. Rev.* **2013**, *42*, 173.

(108) Bordun, O. M.; Bihday, V. G.; Kukharskyy, I. Y. *J. Appl. Spectrosc.* **2014**, *81*, 43.

(109) Riedel, R.; Chen, I.-W. *Ceramics Science and Technology. Volume 1: Structures*Wiley, 2008; Vol. Volume 1.

(110) Chen, Z.; Gao, L. *Cryst. Growth Des.* **2008**, *8*, 460.

(111) Moulder, J. F.; Stickle, W. F.; Sobol, P. E.; Bomben, K. D. *Handbook of X-Ray Photoelectron Spectroscopy*; Perkin Elmer Corporation Eden Prairie, MN, USA, 1992.

(112) Shi, Q.; Zhang, J.; Cai, C.; Cong, L.; Wang, T. *Mater. Sci. Eng., B* **2008**, *149*, 82.

(113) Talam, S.; Karumuri, S. R.; Gunnam, N. *ISRN Nanotechnology* **2012**, *2012*, 6.

(114) Zhang, J.; Gao, D.; Yang, G.; Zhu, Z.; Zhang, J.; Shi, Z. *Int. J. Mater. Mech. Eng.* **2012**, *1*, 38.

(115) Djurišić, A. B.; Ng, A. M. C.; Chen, X. Y. *Prog. Quant. Electron.* **2010**, *34*, 191.

(116) Djurišić, A. B.; Leung, Y. H. *Small* **2006**, *2*, 944.

(117) Djurišić, A. B.; Leung, Y. H.; Tam, K. H.; Ding, L.; Ge, W. K.; Chen, H. Y.; Gwo, S. *Appl. Phys. Lett.* **2006**, *88*, 103107.

(118) Mikenda, W.; Preisinger, A. *J. Lumin.* **1981**, *26*, 67.

(119) Mikenda, W. *J*. *Lumin*. **1981**, *26*, 85.

(120) Ward, M. J.; Han, W.-Q.; Sham, T.-K. *J*. *Phys*. *Chem*. *C* **2011**, *115*, 20507.

(121) Shimizu, K.-i.; Takamatsu, M.; Nishi, K.; Yoshida, H.; Satsuma, A.; Hattori, T. *Chem*. *Commun*. **1996**, 1827.

(122) Chen, H.; Wen, W.; Wang, Q.; Hanson, J. C.; Muckerman, J. T.; Fujita, E.; Frenkel, A. I.; Rodriguez, J. A. *J*. *Phys*. *Chem*. *C* **2009**, *113*, 3650.

(123) Han, W.-Q.; Ward, M. J.; Sham, T. *J*. *Phys*. *Chem*. *C* **2011**, *115*, 3962.

(124) Bazin, D.; Rehr, J. *Catal*. *Lett*. **2003**, *87*, 85.

(125) David, H.; Maud, J.; Fabien, C.; Jean-François, P.; Joakim, A.; José Luis, E. *J*. *Phys*. *D: Appl*. *Phys*. **2010**, *43*, 132003.

(126) Basavaraju, N.; Priolkar, K. R.; Gourier, D.; Bessière, A.; Viana, B. *PCCP* **2015**, *17*, 10993.

(127) Grunes, L. A. *Phys*. *Rev*. *B* **1983**, *27*, 2111.

(128) Rozsályi, E.; Verger, L.; Cabaret, D.; Juhin, A. *Journal of Physics: Conference Series* **2016**, *712*, 012011.

(129) Pinakidou, F.; Kaprara, E.; Katsikini, M.; Paloura, E. C.; Simeonidis, K.; Mitrakas, M. *Journal of Physics: Conference Series* **2016**, *712*, 012082.

(130) Trukhin, A. N.; Goldberg, M.; Jansons, J.; Fitting, H. J.; Tale, I. A. *J*. *Non-Cryst*. *Solids* **1998**, *223*, 114.

(131) http://cxro.lbl.gov/.

(132) Armelao, L.; Heigl, F.; Brunet, S.; Sammynaiken, R.; Regier, T.; Blyth, R. I. R.; Zuin, L.; Sankari, R.; Vogt, J.; Sham, T.-K. *ChemPhysChem* **2010**, *11*, 3625.

(133) Djurišić, A. B.; Leung, Y. H.; Tam, K. H.; Hsu, Y. F.; Ding, L.; Ge, W. K.; Zhong, Y. C.; Wong, K. S.; Chan, W. K.; Tam, H. L.; Cheah, K. W.; Kwok, W. M.; Phillips, D. L. *Nanotechnology* **2007**, *18*, 095702.

Chapter 4. Lanthanide luminescent antenna complexes: role of ligand topology in the decomplexation by dipicolinic acid

4.1 Introduction

Inorganic materials are also employed as substrates and/or hosting matrices for functional molecules. In this context, besides the development of the inorganic material, an essential step concerns the preliminary study and characterization of the molecular system endowed with the functionality of interest. In fact, an accurate knowledge of the nature and behaviour of the functional unit itself, in terms of thermodynamic and kinetic stability, topology, functionality and reactivity, is crucial for a complete comprehension of the final composite system. This section concerned the study of two luminescent lanthanide antenna complexes ($Eu^{3+}\subset$**1**, $Dy^{3+}\subset$**9**, Fig. 4.1) characterized by different ligand topology.

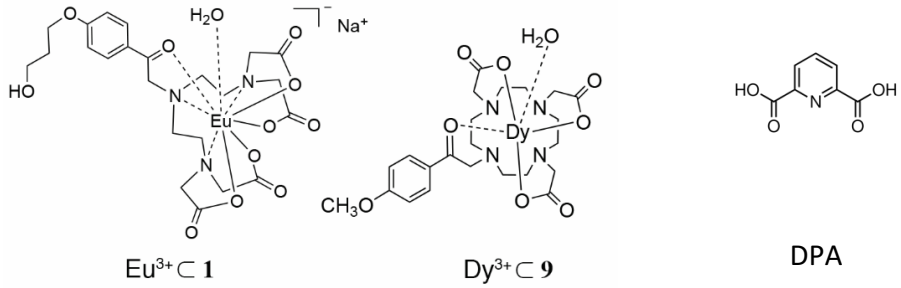

Fig. 4.1 Structure of $Eu^{3+}\subset$ **1** and $Dy^{3+}\subset$ **9** complexes and dipicolinic acid (DPA).

Their behaviour in presence of dipicolinic acid (pyridine-2,6-dicarboxylic acid, DPA) was investigated in order to study the effect of strongly coordinating agents like DPA on their emission properties. To do this, the possibility to develop a

ratiometric sensor for small molecules like DPA in aqueous solution was considered.

Among the great variety of optically active molecules that can be integrated into inorganic materials, luminescent complexes are molecular systems which find application in many fields of technological interest. In this framework, the effectiveness of luminescent lanthanide complexes in analytical and therapeutic applications is nothing new.[1,2] The history of this success is based on the particular electronic configuration of trivalent lanthanide ions, that is, shielded optically active 4f electrons,[3] in combination with the high stability and kinetic inertness of lanthanide complexes prepared from polyaminopolycarboxylic ligands. Initially studied and employed for the development of gadolinium based contrast agents (CA) for Magnetic Resonance Imaging (MRI),[4] acyclic diethylenetriaminepentaacetic acid (DTPA) and macrocyclic 1,4,7,10-tetraazacyclododecane-1,4,7,10-tetraacetic acid (DOTA) have become quite soon also the cornerstones in the preparation of luminescent lanthanide complexes. Over the years many studies were then directed toward the structural modification of the ligands by introduction of appropriate chromophoric groups that are able to promote the indirect sensitization of lanthanide cations ("antenna effect") and, at the same time, to prevent deactivation processes induced by solvent molecules in the first coordination sphere of the metal.

Both polydentate acyclic and cyclic ligands have been considered able to form complexes characterized by high thermodynamic stability and high kinetic inertness. However, particular attention must be given regarding their functionalization since the replacement of even one carboxylate arm may decrease the values of stability constants of several orders of magnitude.[4,5] The formation rates of the complexes with acyclic polydentate ligands (DTPA, DTTA and their derivatives) are high but they have a limited kinetic inertness. Spontaneous and proton assisted decomplexations have been also reported but are considered to be limited at physiological pH.[4-8] Conversely, complexes formed with the macrocyclic DOTA derivatives are kinetically extremely inert.[8]

Among the wide variety of available sensitizers for lanthanide emission, dipicolinic acid plays a particular role. The presence of DPA as the main structural component of the protective outer layers of bacterial spores, *e.g.* *Bacillus Anthracis* (approximately 5-15% of the dry mass), has aroused the interest of many researchers in the development of fast and reliable sensor systems capable of detecting this endospore biomarker.[9-13] In the past years, several analytical approaches have been adopted for the determination of dipicolinic acid mainly based on biochemical,[14-16] electrochemical[17,18] or spectroscopic methods (Photoluminescence, Raman and Surface Enhanced Raman).[10-12,19-25] To this regard, luminescence-based techniques have the edge over the others because, in general, they do not require laborious pretreatment of the sample such as extraction and/or concentration of dipicolinic acid. The most common approach involved the formation of $Ln(DPA)_x(H_2O)_{9-3x}$ complexes (where x = 1, 2 or 3) starting from inorganic lanthanide salts, typically $TbCl_3$. More recently some authors have suggested that the use of preformed complexes of lanthanides, in which the number of coordination sites available for DPA binding is reduced, may overcome the analytical complications due to the presence of complexes with different stoichiometry and luminescent properties.[10,11,19-28]

For these reasons, the behavior of a pair of luminescent complexes with a different ligand topology (Fig. 4.1, $Eu^{3+} \subset$ **1** *probe* and $Dy^{3+} \subset$ **9** *reference*) has been studied in presence of a strong coordinating ligand as DPA and its capability to work as a ratiometric luminescence sensor has been investigated. In both compounds we adopted acetophenone as light harvesting unit since the favourable energy of the excited triplet state (~ 25000 cm^{-1})[29,30] makes it suitable for the sensitization of dysprosium ($^4F_{9/2}$ = 21280 cm^{-1}) and europium ions ($^5D_0$ = 17250 cm^{-1}).[31,32] In $Dy^{3+} \subset$ **9** acetophenone is bonded through a short and flexible spacer to the 1,4,7,10-tetraazacyclododecane-1,4,7-triacetic acid (DO3A),[29,33,34] while as coordination site for the probe complex $Eu^{3+} \subset$ **1** we employed the 1,4,7-triazaheptane-1,1,7,7-tetraacetic acid (DTTA) unit. The ligand produces a

negatively charged complex with europium and is expected to be flexible enough to allow the interaction of the Ln^{3+} sites with polydentate anions.[19,35]

The temporal stability of both luminescent complexes can be easily checked by recording their emission spectra at subsequent time intervals. This represents a practical and important quality control for the sensor system that would not be possible for sensing probes in which luminescence is activated by interaction of the lanthanide ions with the analytes.

The reaction between $Eu^{3+} \subset$ **1** / $Dy^{3+} \subset$ **9** ratiometric pair and DPA has been followed by photoluminescence (PL), NMR spectroscopy and mass spectrometry (MS). PL measurements of the ratiometric mixture upon addition of DPA evidenced the modulation of the emission of $Eu^{3+} \subset$ **1**, while the spectroscopic properties of $Dy^{3+} \subset$ **9** resulted unaffected by the presence of DPA in solution evidencing the high stability and inertness of this complex. The calibration curve of the sensor obtained by emission spectra allowed the quantitative determination of DPA with very good approximation in a range of concentrations 10-40 μM; NMR titration experiments and MS spectrometry allowed us to identify the formation of free ligand **1** and $[EuDPA_2]^-$ complex. The observed changes in PL spectra are therefore due to the formation of other emissive species rather than to the interaction of DPA with $Eu^{3+} \subset$ **1**.

4.2 Results and Discussion

4.2.1 Synthesis of complexes

The synthesis of $Eu^{3+} \subset$ **1** and $Dy^{3+} \subset$ **9** was carried out in collaboration with ISTM-CNR in Milan.[29,36] Both complexes were full characterized by means of NMR spectroscopy, mass spectrometry and elemental analysis.

4.2.2 Optical properties and interaction with DPA

Absorption spectra of $Eu^{3+} \subset$ **1** and $Dy^{3+} \subset$ **9** consist in a single band with maximum at 310 nm due to ligand centred transitions which are overlapped with those of DPA in the 250 -290 nm region. In absence of DPA, the absorption and photoluminescence excitation spectra of the two complexes are superimposed. The emission spectrum of $Eu^{3+} \subset$ **1** in water solution excited in the maximum of the excitation spectrum is composed of several bands associated with the Eu^{3+} $^5D_0 \rightarrow {}^7F_J$ transitions (J = 0 - 4); the higher the J value, the lower the transition energy (red line in Fig. 4.2b).[37] The polydentate acyclic ligand is able to saturate eight of the nine europium coordination sites. The last is occupied by a water molecule, as indicated by the remarkable increase of $^5D_0 \rightarrow {}^7F_J$ lifetimes (Table 1) determined in D_2O.[38]

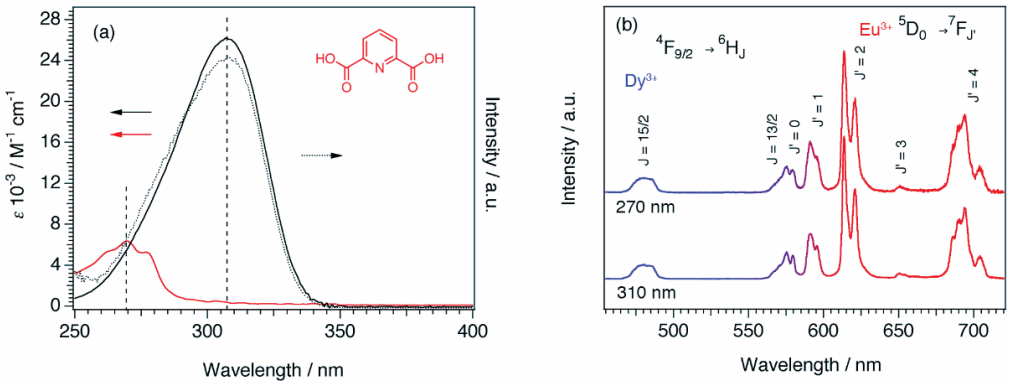

Fig. 4.2 a) Absorption spectra of dipicolinic acid (red curve) and $Eu^{3+} \subset$ **1** (black curve; $Dy^{3+} \subset$ **9** has the same absorption spectra). The excitation spectrum of the lanthanide complexes is reported as a black dotted curve. The vertical dashed lines evidence the excitation wavelengths. b) Emission spectra of the ratiometric pair excited at 310 nm (absorption maximum of acetophenone) and at 270 nm (absorption maximum of DPA).

Concerning Dy^{3+} complex, the macrocyclic ligand **9** is able to saturate eight coordination sites and also in this case one water molecule saturates the lanthanide coordination demand.[29] The Dy^{3+} bands $^4F_{9/2} \rightarrow {}^6H_{15/2}$ and $^4F_{9/2} \rightarrow {}^6H_{13/2}$ are clearly visible in the emission spectra (blue line in Fig. 4.2b). While the latter is partially overlapped with the $^5D_0 \rightarrow {}^7F_0$ transition ($\lambda \approx 580$ nm) of Eu^{3+}, the former is not affected by any spectral interference and is thus adopted as internal reference in the ratiometric pair.

Table 4.1. Photophysical data of $Eu^{3+} \subset$ **1** and $Dy^{3+} \subset$ **9**.

	$Eu^{3+} \subset$ **1**	$Dy^{3+} \subset$ **9**
λ_{max} (nm)	308	308
ε (M^{-1} cm^{-1})	24500	24500
τ_{H_2O} (ms)	0.60	0.012
τ_{D_2O} (ms)	2.35	0.028
Φ_{se} in H_2O[a]	0.07	0.008
Φ_{se} in D_2O[a]	0.29	0.020
q[b]	1.0	1.0[c]

[a] Quantum yield values obtained by using $[Ru(bpy)_3]Cl_2$ as standard (λ_{exc} = 350 nm).
[b] Number of water molecules in the first coordination shell estimated by the Horrocks formula: $q_{Eu} = 1.11\ (1/\tau_{H_2O} - 1/\tau_{D_2O} - 0.31)$.[38]
[c] The number of water molecules has been calculated for the corresponding europium complex for which Horrocks equation can be used.

In DPA free solutions, no appreciable differences are evidenced between the emission spectra (Fig. 4.2b) obtained by exciting the ratiometric couple at 270 nm (absorption band of DPA) and 310 nm, where only the acetophenone moiety is able to sensitize lanthanide emission (Fig. 4.2a). Upon addition of increasing amounts of DPA to a 10^{-5} M solution of $Eu^{3+} \subset$ **1** and $Dy^{3+} \subset$ **9** (1:1 molar ratio), relevant modifications in the emission spectra are observed under excitation at 270 nm (Fig. 4.3a).

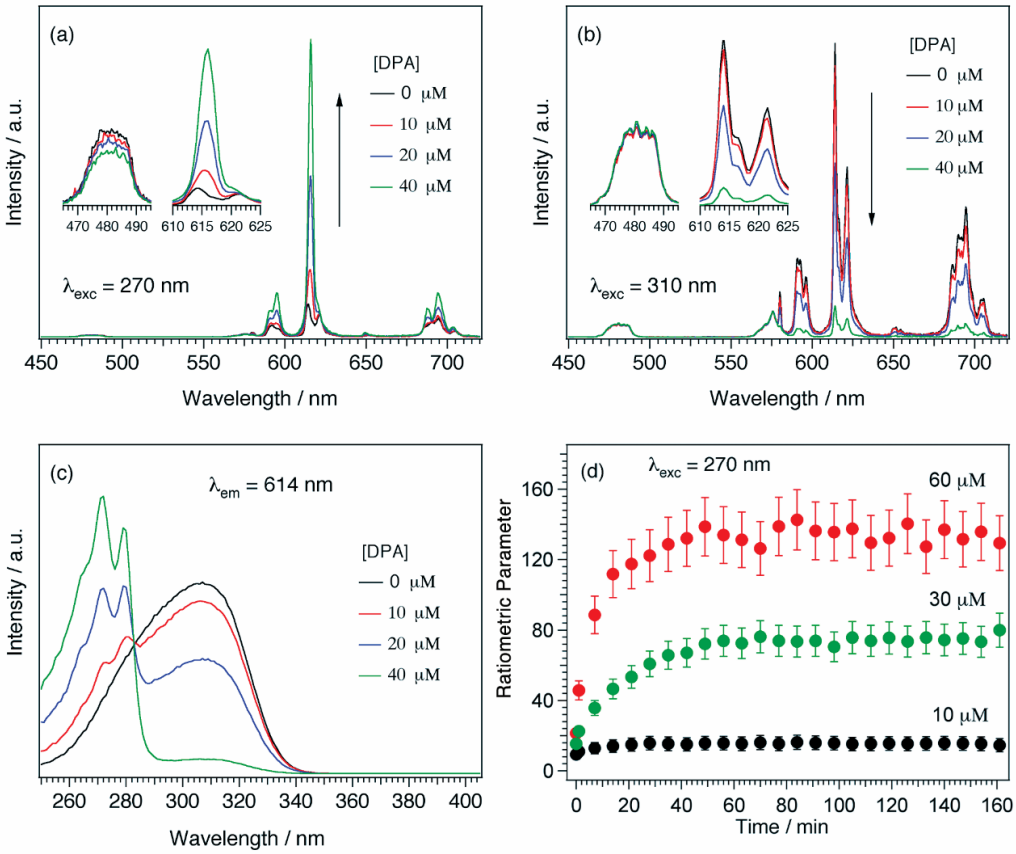

Fig. 4.3 Emission spectra of the ratiometric pair at different DPA concentrations excited at 270 (a) and 310 nm (b). The inset evidences details of the most intense emission bands of Dy^{3+} and Eu^{3+}. The arrows indicate the increase of DPA concentration. c) Excitation spectra monitored on the $^5D_0 \rightarrow {}^7F_2$ europium transition. d) Temporal response of the ratiometric sensor after addition of 10, 30 and 60 μM DPA solutions. Error bars (± 15%) have been determined by performing three different sets of experiments.

As for Dy^{3+} emission, a slight intensity decrease is observed at high DPA concentrations. Indeed, due to the overlap of the corresponding absorption spectra, dipicolinic acid competes with acetophenone at $\lambda_{exc} < 290$ nm acting as an internal filter (Fig. 4.2a). Accordingly, similar modifications in the Dy^{3+} emission spectra are not revealed (Fig. 4.3b) upon excitation at 310 nm. On the contrary we observed a significant variation on the relative intensity between the different $^5D_0 \rightarrow {}^7F_J$ multiplets of Eu^{3+} as function of DPA concentration (Fig. 4.3a). The transition J = 2 is remarkably increased compared to all the others and undergoes a moderate red shift. These changes indicate the occurrence of

structural rearrangements around the Eu^{3+} centres.[39-41] The behavior of the ratiometric pair is particularly interesting upon excitation at 310 nm, *i.e.* in the spectral region where DPA is not absorbing (Figg. 2a and 3b). In this case a decrease in the overall intensity of europium emission is observed at DPA concentrations higher than 10 μM. This trend can not be ascribed to coordinative rearrangements in $Eu^{3+} \subset$ **1** since the shape of Eu^{3+} emission bands is not modified by the presence of DPA. A similar behavior has been also evidenced for each of the $Eu^{3+} \subset$ **1** and $Dy^{3+} \subset$ **9** complexes (not shown). Taken together, all these observations suggest that DPA molecules are able to coordinate Eu^{3+} ions. Evidence of this mechanism is also supported by the excitation spectra of the complexes (Fig. 4.3c), where a new excitation pathway *via* dipicolinic acid is clearly discernible by increasing the DPA concentration in solution. The response toward the molecular recognition event is displayed in Fig. 4.3d for three DPA concentrations (10, 30 and 60 μM). The ratio between the integrated area of Eu^{3+} $^5D_0 \rightarrow {}^7F_J$ with J = 1-4 (583 – 715 nm) and Dy^{3+} $^4F_{9/2} \rightarrow {}^6H_{15/2}$ (456 - 505 nm) has been adopted as ratiometric parameter (R). Whereas the presence of DPA is revealed instantaneously, a longer time is required to reach equilibrium. In fact, R shows a continuous variation until reaching a constant value, that occurs *ca*. 60 min after DPA addition.

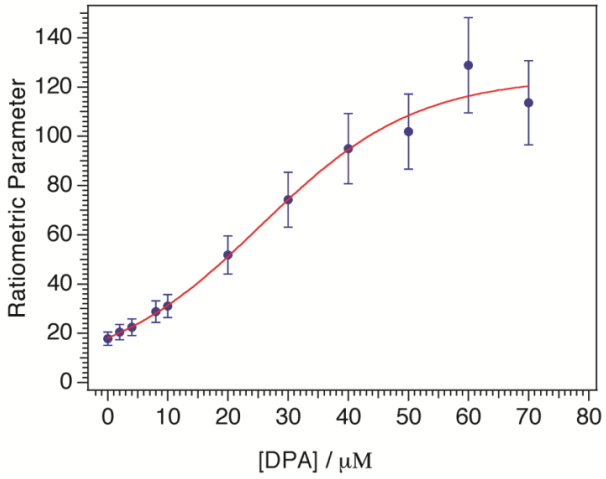

Fig. 4.4 Calibration curve of the sensor (λ_{exc} = 270 nm): experimental points and curve obtained from fitting by means of a sigmoid function. Error bars (± 15%) have been determined by performing three different sets of experiments.

The calibration curve of the ratiometric sensor (Fig. 4.4) is determined by evaluating the ratiometric parameter from the emission spectra excited at 270 nm and recorded 60 min after DPA addition. The whole curve can be well interpolated by means of a sigmoid function with a DPA limit of detection (LOD) of 2 μM.

4.2.3 NMR titration and mass spectrometry

NMR titration and mass spectrometry experiments were performed in order to get detailed information about the structure of the chemical species formed in the reaction of DPA with $Eu^{3+} \subset \mathbf{1}$.

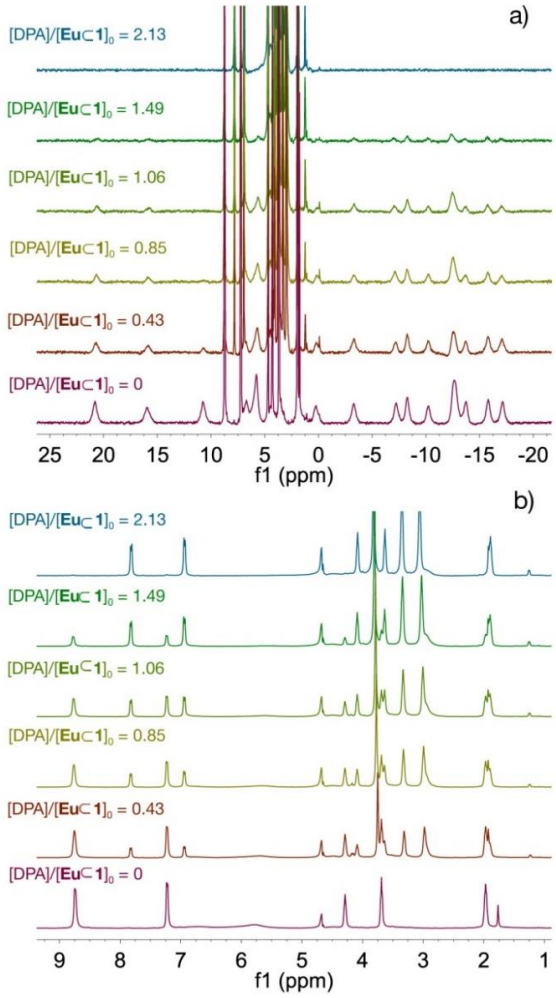

Fig. 4.5 ^{1}H NMR titration with water suppression of complex $Eu^{3+} \subset \mathbf{1}$ (2.8×10^{-3} M, D_2O) with aliquots of DPA (0.047 M in D_2O): a) full spectral width and b) expanded region 1.0 – 9.5 ppm.

Proton NMR titrations were performed by adding aliquots of a D_2O solution of DPA to a D_2O solution of the europium complex. We observed the interconversion of the signals of the pristine complex $Eu^{3+} \subset$ **1** into a new pattern of signals shifted in frequency (Fig. 4.5). In particular the AX spin system of $Eu^{3+} \subset$ **1** (8.75 and 7.25 ppm) gradually disappears, while a new AX spin system at 7.82 and 6.94 ppm becomes visible for increasing amounts of DPA. A similar situation occurs with respect to the signals of the propyl chain at 4.29, 3.69 and 2.11 ppm that are replaced by new signals at 4.08, 3.63 and 1.89 ppm, respectively, the latter being superimposed on another signal not well identified. Even low-field and high-field frequencies gradually decrease for increasing amounts of DPA in solution, disappearing entirely for [DPA]/$[Eu^{3+} \subset \mathbf{1}]_0$ ratios greater than 2.13. All these observations point to a slow exchange regime between two species. The second species is identifiable with free ligand **1**, in analogy with the spectrum of the benzyloxy protect ligand **1** (see ref.36); also the signals to 3.36 and 3.05 ppm are compatible with the protons of ethylenic groups of the free ligand. We assumed that the lack of stability of the complex $Eu^{3+} \subset$ **1** could be mainly due to the chelating ability of DPA towards the Eu^{3+} cation.

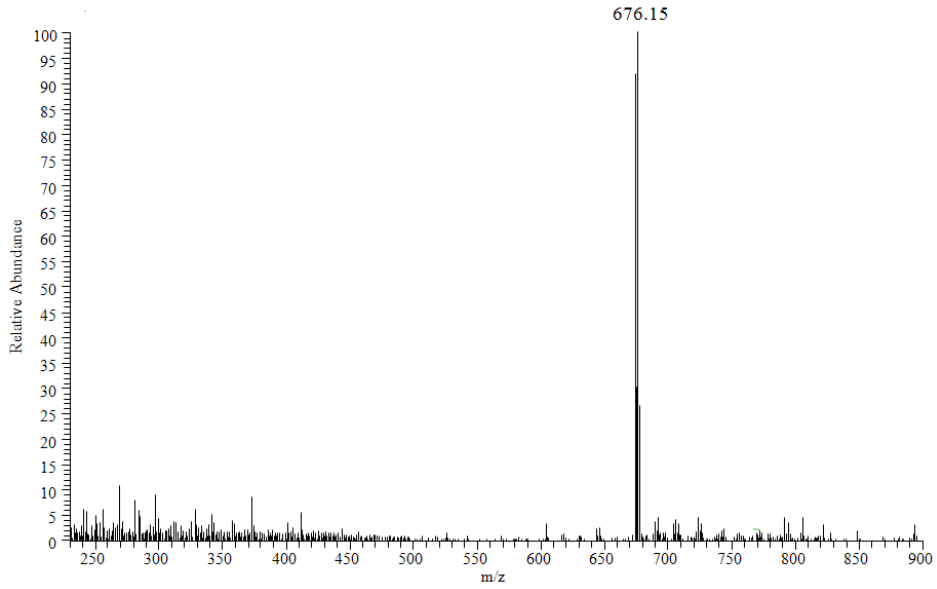

Fig. 4.6 Negative ion ESI mass spectrum of water solution of $Eu^{3+} \subset$ **1** (10^{-5}M).

In order to identify the species formed in water solution of $Eu^{3+} \subset$ **1** after the addition of DPA, electrospray mass spectrometry (ESI/MS) experiments have been performed on pure $Eu^{3+} \subset$ **1** (10^{-5} M) and in presence of DPA (60 μM). The negative ions ESI mass spectrum of the Eu^{3+} complex, reported in Fig. 4.6, shows only one peak due to an anion corresponding to $[M\text{-}Na]^-$, with an isotopic cluster in agreement with the presence of one Eu atom.

After the addition of DPA, ESI mass spectra have been recorded at different times and the results of these experiments are summarized in Fig. 4.7.

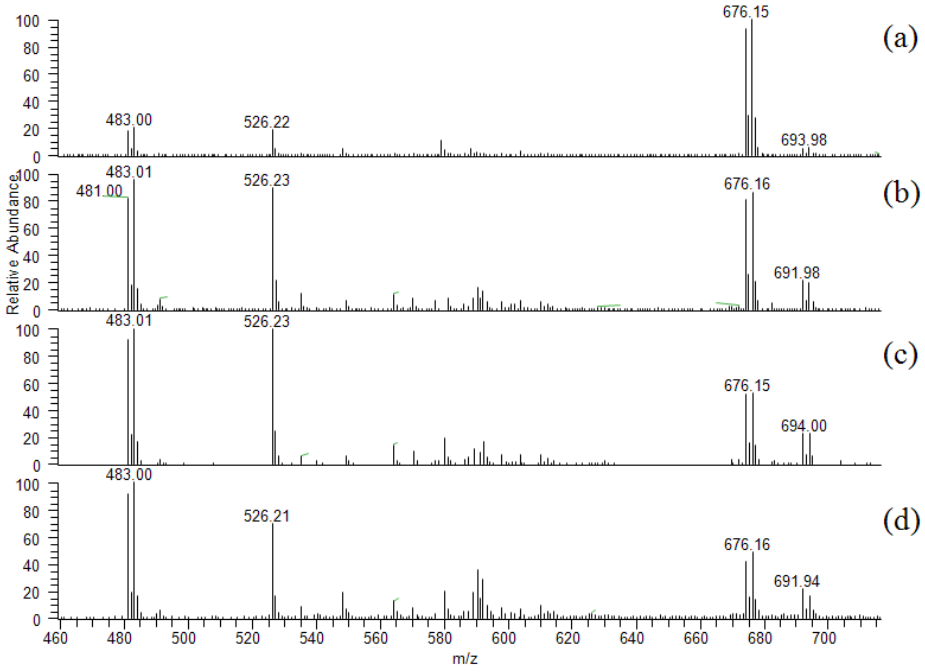

Fig. 4.7 ESI mass spectra of $Eu^{3+} \subset$ **1** (10^{-5} M in water) after the addition of DPA (60 μM) recorded at different times: (a) t = 2 min, (b) t = 35 min, (c) t = 60 min and (d) t = 180 min).

As it can be seen, the addition of DPA to $Eu^{3+} \subset$ **1** leads to the formation of other ionic species, well detectable just after 2 min. In particular, the signals at m/z 526 are related to the free ligand **1** and those at m/z 481, characterized by the isotopic cluster of europium, are in agreement with the presence of the $[Eu(DPA)_2]^-$ species. This indicates that DPA is able to replace **1** in the europium coordination

sphere thus forming a new stable complex. Signals ascribable to $Eu^{3+} \subset$ **1**-DPA adducts have not been detected.

4.3 Conclusions

In summary, we have studied the behavior in water solution of two luminescent lanthanide complexes, $Eu^{3+} \subset$ **1** and $Dy^{3+} \subset$ **9,** in presence of dipicolinic acid and their suitability to work as DPA ratiometric luminescent sensor. Both antenna complexes bear acetophenone as a common sensitization unit for lanthanide emission. The reference complex ($Dy^{3+} \subset$ **9**) contains a rigid DO3A macrocyclic ligand which prevents the bonding of DPA to the Dy^{3+} centres. In this way, $Dy^{3+} \subset$ **9** luminescence is not affected by the presence of DPA thus evidencing the inertness of the macrocyclic structure that, being constrained to its cyclic form, does not allow conformational freedom. On the other side, the recognition of the DPA target molecule was possible because of the properties of the coordination unit in $Eu^{3+} \subset$ **1**. In fact, the use of a flexible coordination site like DTTA allows the binding of DPA to Eu^{3+} centres, but Eu^{3+}-DPA interactions are so strong to induce a ligand exchange reaction with formation of free **1** and $[EuDPA_2]^-$, as evidenced by NMR and mass spectrometry. The observed modulation of the luminescence signal is therefore due to the decomplexation of $Eu^{3+} \subset$ **1** and the formation of new emitting species. The ratiometric pair allows the quantitative determination of DPA with very good approximation in the 10-40 μM concentration range. These results evidence the importance of the topology of the ligands in the stability and inertness of the complexes. In particular, the employment of macrocyclic ligands that have a preformed cavity in which the metal ions can be hosted insures a better stability over acyclic ligands having the same number and typology of coordination sites. This different behavior can be usefully exploited in analytical applications.

Moreover, these findings provide crucial information also for the future development of solid state sensors, realized by grafting suitable complexes on appropriate solid matrices.

4.4 Experimental.

Chemicals and characterization

All available chemicals and solvents were purchased from commercial sources and were used without any further purification. Thin layer chromatography (TLC) was conducted on plates precoated with silica gel Si 60-F254 (Merck, Darmstadt, Germany). Column chromatography was carried out by using silica gel Si 60, 230-400 mesh, 0.040-0.063 mm (Merck, Darmstadt, Germany). ^{1}H and ^{13}C NMR spectra were recorded on a Bruker Avance 400 spectrometer (400 and 100.6 MHz, respectively) equipped with a 5 mm ^{13}C-^{1}H dual probe; ^{1}H NMR spectrum of $Dy^{3+} \subset$ **9** was recorded on a Bruker Avance 400 spectrometer (400 MHz) equipped with a 4-mm double resonance (^{1}H, ^{13}C) gradient HR-MAS probe; spinning rates of 8 kHz and 10 kHz was used to reduce line broadening and presaturation experiments were performed in order to attribute spurious signals due to rotation. Chemical shifts are indicated in parts per million downfield from $SiMe_4$, using the residual proton ($CDCl_3$ = 7.26 ppm, $(CD_3)_2SO$ = 2.50 ppm, HOD = 4.80 ppm) and carbon ($CDCl_3$ = 77.0 ppm, $(CD_3)_2SO$ = 40.45 ppm) solvent resonances as internal reference. Coupling constants values *J* are given in Hz. Protons and carbon assignments were achieved by ^{13}C-APT, ^{1}H-^{1}H COSY, ^{1}H-^{13}C heteronuclear single quantum coherence (HSQC) and heteronuclear multiple-bond correlation (HMBC) experiments. 2D Exchange Spectroscopy (EXSY) experiments were collected by using the standard 90°-t_1-90°-τ_M-90° (noesyph) pulse sequence and a mixing time (d8) of 10 ms. High resolution mass spectra were obtained with an electrospray ion-trap mass spectrometer ICR-FTMS APEX II (Bruker Daltonics) by the Centro Interdipartimentale Grandi Apparecchiature (C.I.G.A.) of the University of Milano.

General procedure for NMR titrations experiments

A solution of $Eu^{3+} \subset$ **1** was prepared by weighing a solid sample of the complex (1.5 - 1.9 mg) in a 5mm NMR sample tube and by dissolving it in D_2O. A

reference spectrum with water suppression (zgpr pulse program) was collected at 297 K. Then aliquots of 10 – 20 μl of a solution of DPA were added; after each addition, the sample is manually stirred for about one minute prior to record the spectrum.

Photoluminescence sensing experiments

Sensing experiments were performed on 10^{-5} M water solutions of $Eu^{3+} \subset$ **1**, $Dy^{3+} \subset$ **9** and on their 1:1 mol mixtures by adding in the cuvette successive amounts (3 μL each) of 10^{-2} M DPA solutions with a Gilson® micropipette, up to a final DPA concentration of 70 μM. In this way dilution effects can be neglected. As ratiometric parameter (R) we have adopted the ratio between the integrated area of Eu^{3+} $^5D_0 \rightarrow {}^7F_J$ with J = 1-4 (583 – 715 nm) and Dy^{3+} $^4F_{9/2} \rightarrow {}^6H_{15/2}$ (456 - 505 nm). The temporal response of the sensor was studied for 10, 30 and 60 μM DPA solutions. The proper amount of DPA (10^{-2} M) was added directly into the cuvette. Subsequently, the emission spectra (λ_{exc} = 270 and 310 nm) were recorded at regular time intervals, every 7 min up to 3 h. Kinetic curves were determined by plotting R *vs* time for each concentration.

Optical properties

Absorption spectra in the UV-Vis were performed on water solutions using a double-beam CARY5E spectrophotometer with a spectral bandwidth of 1 nm. The luminescence spectra were recorded on water (or D_2O) solutions at room temperature with a Fluorolog-3 (Horiba Jobin Yvon) spectrofluorimeter.
Quantum yield determination was performed using air equilibrated $[Ru(bpy)_3]Cl_2$ water solutions as standard.[42] Three independent measurements were carried out on each complex with an estimated error Φ values of ± 10%. Quantum yield values are independent of the excitation wavelength in the investigated range.

Mass spectrometric analysis

Electrospray mass spectrometric measurements have been made by LCQ Fleet ion trap instrument (ThermoFisher Scientific, San Josè, CA, USA), operating in

negative ion mode. The entrance capillary temperature was 280 °C and the capillary voltage was 4 kV. $Eu^{3+} \subset$ **1** was firstly dissolved in MilliQ water at a concentration of 10^{-3} and then diluted 1 to 100 in the same solvent. This solution was introduced into the ESI ion source by direct infusion at a flow rate of 8 μL/min. The He pressure inside the trap was kept constant. The pressure directly read by ion gauge (in the absence of the N_2 stream) was $2.8 \cdot 10^{-5}$ Torr.

4.5 References

(1) Parker, D.; Dickins, R. S.; Puschmann, H.; Crossland, C.; Howard, J. A. K. *Chem. Rev.* **2002**, *102*, 1977.

(2) Butler, S. J.; Parker, D. *Chem. Soc. Rev.* **2013**, *42*, 1652.

(3) Bünzli, J.-C. G.; Eliseeva, S. V. In *Springer Ser. Fluoresc.*; Springer GmbH: **2011**; Vol. 7, p 1.

(4) Merbach, A.; Helm, L.; Tóth, E. In *The Chemistry of Contrast Agents in Medical Magnetic Resonance Imaging*; John Wiley & Sons, Ltd: **2013,** p i.

(5) Braddock, M. *Biomedical Imaging : The Chemistry of Labels, Probes and Contrast Agents*; Royal Society of Chemistry, **2011**.

(6) Pálinkás, Z.; Baranyai, Z.; Brücher, E.; Rózsa, B. *Inorg. Chem.* **2011**, *50*, 3471.

(7) Yantasee, W.; Fryxell, G. E.; Porter, G. A.; Pattamakomsan, K.; Sukwarotwat, V.; Chouyyok, W.; Koonsiripaiboon, V.; Xu, J.; Raymond, K. N. *Nanomedicine: Nanotechnology, Biology and Medicine* **2010**, *6*, 1.

(8) Caravan, P.; Ellison, J. J.; McMurry, T. J.; Lauffer, R. B. *Chem. Rev.* **1999**, *99*, 2293.

(9) Gültekin, A.; Ersöz, A.; Sarıözlü, N. Y.; Denizli, A.; Say, R. *J. Nanopart. Res.* **2009**, *12*, 2069.

(10) Cable, M. L.; Kirby, J. P.; Levine, D. J.; Manary, M. J.; Gray, H. B.; Ponce, A. *J. Am. Chem. Soc.* **2009**, *131*, 9562.

(11) Cable, M. L.; Kirby, J. P.; Sorasaenee, K.; Gray, H. B.; Ponce, A. *J. Am. Chem. Soc.* **2007**, *129*, 1474.

(12) Zhang, X.; Young, M.; Lyandres, O.; Van Duyne, R. *J. Am. Chem. Soc.* **2005**, *127*, 4484.

(13) Lee, I.; Oh, W.-K.; Jang, J. *J. Hazard. Mater.* **2013**, *252-253*, 186.

(14) Wang, L.; Han, Y.; Zhou, S.; Wang, G.; Guan, X. *ACS Applied Materials & Interfaces* **2014**, *6*, 7334.

(15) Tan, H.; Ma, C.; Chen, L.; Xu, F.; Chen, S.; Wang, L. *Sens. Actuators, B* **2014**, *190*, 621.

(16) Hurtle, W.; Bode, E.; Kulesh, D. A.; Kaplan, R. S.; Garrison, J.; Bridge, D.; House, M.; Frye, M. S.; Loveless, B.; Norwood, D. *J. Clin. Microbiol.* **2004**, *42*, 179.

(17) Chaoliang, T.; Qianming, W.; Cheng Cheng, Z. *Chem. Commun.* **2011**, 12521.

(18) Kim, D. J.; Park, H. C.; Sohn, I. Y.; Jung, J. H.; Yoon, O. J.; Park, J. S.; Yoon, M. Y.; Lee, N. E. *Small* **2013**, *9*, 3352.

(19) Barnes, L. S.; Kaneshige, K. R.; Strong, J. S.; Tan, K.; von Bremen, H. F.; Mogul, R. *J. Inorg. Biochem.* **2011**, *105*, 1580.

(20) Ai, K.; Zhang, B.; Lu, L. *Angew. Chem. Int. Ed.* **2009**, *48*, 304.

(21) Yilmaz, M. D.; Hsu, S.-H.; Reinhoudt, D. N.; Velders, A. H.; Huskens, J. *Angew. Chem. Int. Ed.* **2010**, *49*, 5938.

(22) Kirby, J. P.; Cable, M. L.; Levine, D. J.; Gray, H. B.; Ponce, A. *Anal. Chem.* **2008**, *80*, 5750.

(23) Pellegrino, P. M.; Fell, N. F. J.; Rosen, D. L.; Gillespie, J. B. *Anal. Chem.* **1998**, *70*, 1755.

(24) Smith, C. B.; Anderson, J. E.; Edwards, J. D.; Kam, K. C. *Appl. Spectrosc.* **2011**, *65*, 866.

(25) Rosen, D. L.; Sharpless, C.; McGown, L. B. *Anal. Chem.* **1997**, *69* 1082.

(26) Shafaat, H. S.; Ponce, A. *Appl. Environ. Microbiol.* **2006**, *72*, 6808.

(27) Yung, P.; Lester, E.; Bearman, G.; Ponce, A. *Biotechnol. Bioeng.* **2007**, *98*, 864.

(28) Lester, E.; Bearman, G.; Ponce, A. *Engineering in Medicine and Biology Magazine, IEEE* **2004**, *23*, 130.

(29) Beeby, A.; Bushby, L. M.; Maffeo, D.; Gareth Williams, J. A. *J. Chem. Soc., Dalton Trans.* **2002**, 48.

(30) Chattopadhyay, S. K.; Kumar, C. V.; Das, P. K. *J. Photochem.* **1985**, *30*, 81.

(31) de Sá, G. F.; Malta, O. L.; de Mello Donegá, C.; Simas, A. M.; Longo, R. L.; Santa-Cruz, P. A.; da Silva Jr., E. F. *Coord. Chem. Rev.* **2000**, *196*, 165.

(32) Carlos, L. D.; Ferreira, R. A. S.; de Zea Bermudez, V.; Ribeiro, S. J. L. *Adv. Mater.* **2009**, *21*, 509.

(33) Armelao, L.; Bottaro, G.; Quici, S.; Cavazzini, M.; Raffo, M. C.; Barigelletti, F.; Accorsi, G. *Chem. Commun.* **2007**, 2911.

(34) Quici, S.; Cavazzini, M.; Raffo, M. C.; Armelao, L.; Bottaro, G.; Accorsi, G.; Sabatini, C.; Barigelletti, F. *J. Mater. Chem.* **2006**, *16*, 741.

(35) Mato-Iglesias, M.; Roca-Sabio, A.; Pálinkás, Z.; Esteban-Gómez, D.; Platas-Iglesias, C.; Tóth, É.; de Blas, A.; Rodríguez-Blas, T. *Inorg. Chem.* **2008**, *47*, 7840.

(36) Mian, F.; Bottaro, G.; Seraglia, R.; Cavazzini, M.; Quici, S.; Armelao, L. *ChemPhysChem* **2016**, *17*, 3229.

(37) Lima, P. P.; Nolasco, M. M.; Paz, F. A. A.; Ferreira, R. A. S.; Longo, R. L.; Malta, O. L.; Carlos, L. D. *Chem. Mater.* **2013**, *25*, 586.

(38) Supkowski, R. M.; Horrocks Jr, W. D. *Inorg. Chim. Acta* **2002**, *340*, 44.

(39) Armelao, L.; Bottaro, G.; Bovo, L.; Maccato, C.; Pascolini, M.; Sada, C.; Soini, E.; Tondello, E. *J. Phys. Chem. C* **2009**, *113*, 14429.

(40) Reisfeld, R.; Zigansky, E.; Gaft, M. *Mol. Phys.* **2004**, *102*, 1319.

(41) Binnemans, K. *Coord. Chem. Rev.* **2015**, *295*, 1.

(42) Brouwer, A. M. *Pure Appl. Chem.* **2011**, *83*, 2213.

Appendix

A.1 Sol-gel method[1]

The sol-gel method belongs to the family of synthesis processes conducted in liquid phase and it represents a wet-chemical technique widely employed to create a great variety of materials and in particular metal oxides.[2-4] Compared to other synthesis methods commonly adopted to obtain oxide materials, such as solid state method, combustion method and hydrothermal method, the sol-gel technique is considered a soft chemical approach because it provides relatively low processing temperatures under atmospheric pressure conditions. The first step of the procedure consists in the preparation of a precursor solution which leads to the formation of the *sol* – i.e. suspension of colloidal particles in a liquid - after hydrolysis and condensation reactions. Subsequently, the gel formation results from the creation of a three dimensional solid network which surrounds and supports the liquid phase. Finally, the removal of the solvent by evaporation (or extraction) allows to obtain xerogels (or aerogels) and subsequent heat treatments lead to formation and consolidation of the final material. These technique is particularly versatile both to obtain a variety of different nanostructures (nanopowders, fibers and films) as well as compositions i.e. single or multi-component inorganic and inorganic-organic hybrid materials.[5] The versatility of the method resides in the high number of parameters which can be tuned to control the hydrolysis and condensation steps (e.g. kind of precursors, catalyst, concentrations, solvent, pH, T) as well as the subsequent gelation and aging of the system. In particular, the nature of precursors, their concentration and the relative ratio with the other components of the precursor solution (water, catalysts and/or stabilizing agents) are crucial to balance the competition between hydrolysis and condensation reactions. In this framework, when different metal precursors (M and M') are employed, the order in which they are combined may be fundamental to trigger their hydrolytic behaviour and control the formation of hetero (M-O-M') and homo (M-O-M) oxo-bridges through condensation reactions. Moreover, the removal of the solvent and the final thermal treatments may considerably affect

the morphology, composition and microstructure of the final product. Consequently, the optimization of all process parameters plays an essential role on the final properties of the material and, at the same time, constitutes a challenge which requires rigour and good vision of the whole procedure.

A.2 X-Ray Diffraction

Microstructural analysis has been performed by means of XRD. This technique is based on the coherent elastic scattering that an X-ray photon undergoes because of its interaction with the electrons of the material and the resulting interference pattern between scattered rays. The most common and simplest description of X-ray diffraction is given by Bragg's model which describes the phenomenon as a selective reflection of monochromatic radiation due to the presence of crystallographic atomic planes (Fig. A.1).[6]

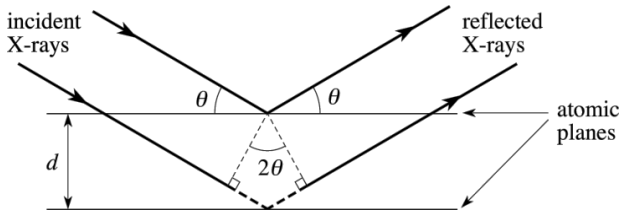

Fig. A.1: Bragg's law diagram.

Bragg's equation describes the condition for constructive interference of an X-ray photon scattered from parallel atomic planes as:

$$n\lambda = 2d_{hkl} \cdot \text{sen}\theta$$

where λ is the wavelength of the incident beam, d_{hkl} is the spacing between atomic planes which generate the reflection, θ is the incident angle between the X-ray beam and the lattice plane, and n represents the diffraction order. hkl are the Miller's indices which identify the lattice planes responsible of the diffraction.

Diffraction measurements consist in the irradiation of the samples with a collimated monochromatic X-ray beam and rays diffracted from the sample are then collected with an appropriate detector. Different geometries can be adopted

between source-sample-detector characterized by different incident angles or collected angles.

The XRD pattern contains all the structural information of a crystalline sample. The angular position is used to determine the inter-planar distances (d) and the crystallographic cell parameter, thus identifying the crystalline phase. The intensity of peaks contains information about the degree of crystallinity of the material.

A.2.1 XRD on bismuth oxychlorides and subcarbonate

XRD measurements on powders were collected with a Bruker D8 Advance diffractometer in Bragg–Brentano geometry with a Göbel mirror and a Cu Kα source (40 kV, 40 mA) in the 5-75° 2θ range.

A.2.2 XRD on $ZnGa_2O_4:Cr^{3+}$ thin films

Glancing incidence XRD measurements on films were carried out in the 15-50° 2θ range, by means of the same diffractometer described above and employing a fixed incidence angle of 1°.

In general, the width of a peak is inversely proportional to the average size of crystallites Φ along the direction normal to the plane hkl which gives rise to that specific reflection. The average crystallite dimensions were estimated from line broadening by means of the Scherrer's equation[7]:

$$\beta_{hkl} = \frac{K\lambda}{\Phi cos\theta}$$

where β_{hkl} is the full width at half maximum (FWHM) of the peak and K is a constant which depends on the shape of the crystallite and whose value ranges from 0.7 to 1.4, but it can be set at 1 within a good approximation.

Phase compositions were calculated by means of the reference intensity ratio method in the framework of MATCH! software and employing the ZnO and $ZnGa_2O_4$ CIF files deposited on the COD (Crystallography Open Database). This method is used for quantitative analysis by powder diffraction and is based upon scaling all diffraction data to the diffraction of standard reference materials.

A.3 X-Ray Photoelectron Spectroscopy[8]

XPS (also known as ESCA, Electron Spectroscopy for Chemical Analysis) exploits the photoelectric effect to obtain information on the chemical composition of surfaces. Surface analysis is accomplished by irradiating the sample *in vacuo* with monoenergetic soft x-rays and analysing the energy of the emitted electrons. Usually, Mg Kα (1253.6 eV) or Al Kα (1486.6 eV) X-rays are used because these photons have enough energy to interact with atoms in the surface region and provoke the emission of one or more electrons. The emitted electrons have measured kinetic energies given by:

$$KE = h\nu - BE - \varphi_s$$

where *KE* is the kinetic energy of the photo-emitted electron, $h\nu$ is the energy of the incident photon, *BE* is the binding energy of the photo-emitted electron and φ_s is the spectrometer work function. During an XPS experiment the kinetic energy of the photo-emitted electron is measured and the correlated binding energy provides an estimate of the bound energy of that particular electron. Since each element has a unique set of binding energies which depend of its chemical state, the kinetic energy of the emitted electron provide information regarding the type of atom from which it was emitted and its chemical environment.

XPS is a surface sensitive analysis technique because only electrons from the outer layers of a solid material can escape and reach the detector without significant loss of energy. Electrons emitted by layers below the surface (> 50 Å) lose most of their energy due to inelastic collision so that they are not able to escape the surface or, once they do, their kinetic energy is so low that they only contribute to the background of the spectrum.

All XPS measurements were performed on a Perkin-Elmer Φ 5600ci spectrometer at a working pressure lower than 10^{-9} mbar. The specimens, mounted on steel sample holders, were introduced directly into the XPS analytical chamber by a fast entry lock system. The sample analysis area was 800 μm in diameter. The reported Binding Energies (BEs, standard deviation = ± 0.2 eV) were corrected for charging effects assigned to the adventitious C1s line at BE of 284.8 eV. [9,10]

The analysis involved Shirley-type background subtraction and, whenever necessary, spectral deconvolution which was carried out by non-linear least-squares curve fitting, adopting a Gaussian–Lorentzian sum function. [11] The atomic composition of the samples was calculated by peak integration, using sensitivity factors provided by the spectrometer manufacturer (Φ V5.4A software) and taking into account the geometric configuration of the apparatus. The experimental uncertainty on the atomic composition values is within 10-20 %.[8]

A.3.1 XPS on bismuth oxychlorides and subcarbonate

A non monochromatized Mg-Kα radiation (1253.6 eV) was employed and survey scans were run in the 0–1100 eV range. Detailed spectra were recorded for the following regions: Bi4f, Cl2p, O1s and C1s.

A.3.2 XPS on $ZnGa_2O_4:Cr^{3+}$ thin films

A non mono-chromatized Al Kα radiation (1486.6 eV) was employed and survey scans were run in the 0-1350 eV range. Detailed spectra were recorded for the following regions: Ga2p, Zn2p, Cr2p, O1s, C1s and Si2p. No further element was detected.

Depth profiles were carried out by Ar^+ sputtering at 3.5 kV, with an ion gun emission current of 20 mA, argon partial pressure of 5×10^{-8} mbar and raster size of 2 x 2 mm^2.

A.4 Scanning Electron Microscopy

The morphological features of the samples were investigated by field emission SEM analysis (FE-SEM).

This microscopy employs as a probe an electron beam which interacts with the material giving rise to elastic and inelastic scattering events. The image of the sample is reconstructed by the electronics of the detectors that collect the out-coming signals which are usually secondary electrons and backscattered electrons. The formers are generated from inelastic scattering between the in-coming beam and electrons (from the core or the outer shells) of atoms in the sample and they have relatively low energies (< 50 eV). On the contrary, all electrons with

energies above 50 eV are classified as backscattered thus generated as a result of elastic scattering. When the atomic number Z of the atoms in the sample increases, the contribution of backscattered electrons is strongly favoured over the inelastically scattered ones. The incoming electrons are focused on the sample by a system of electromagnetic lenses so that the beam spot has variable size from a few nm to tens of nm. The area of analysis is then raster scanned and the out-coming signals are recorded as a function of the beam position to generate the image. Since their emission yield is highly sensitive to the orientation of the surface with the primary beam and to the presence of local electric fields and/or magnetic fields, secondary electrons are usually used in morphological investigation. Moreover, given their low energy (between 0 and 50 eV), it is possible to reveal only secondary electrons generated in the outer layers of the material.

SEM measurements were performed by a Sigma Zeiss instrument operated at an acceleration voltage of 5 kV using secondary electrons, after platinum electrodeposition on samples.

The morphology of thin films was evaluated on samples prepared by deposition on silicon substrates and after manual cut in order to get cross-sectional SEM images.

A.5 Optical measurements

Absorption spectra on films and water solutions were performed on a double-beam CARY5E spectrophotometer with a spectral bandwidth of 1 nm in the range 250-800 nm.

Spectra on powders were collected on the same instrument in diffuse reflectance.

The luminescence spectra were recorded at room temperature with a Fluorolog-3 (Horiba Jobin Yvon) spectrofluorimeter equipped with double-grating monochromator in both the excitation and emission sides coupled to a R928P Hamamatsu photomultiplier, and a 450 W Xe arc lamp as the excitation source. The emission spectra were corrected for detection and optical spectral response of

the spectrofluorimeter through a calibration curve supplied by the manufacturer. The excitation spectra were corrected for the spectral distribution of the lamp intensity using a photodiode reference detector. The luminescence lifetimes in the microsecond–second scales were measured using a pulsed Xe lamp with variable repetition rate and elaborated with standard software fitting procedures. The quality parameters (χ^2) for all the fittings were ~1. All luminescence measurements were performed in air at room temperature.

Luminescence experiments at variable temperature were performed using a Linkam THMS600 temperature controlled stage (-196 – 600 °C, Temperature stability < 0.1°C) coupled with an Horiba T6400 triple spectrometer working in a direct single spectrometer configuration (300 lines/mm grating). A 450 W Xe arc lamp and a Peltier cooled CCD (Horiba Synapse) were used as excitation source and detector, respectively. The emitted radiation was collected in a backscattering geometry through a 10x Olympus Plan Achromat Objective (0.25 NA).

A.6 X-Ray Absorption Near-Edge Spectroscopy

X-ray Absorption Spectroscopy (XAS) is an element specific technique that allows the study of electronic transitions from inner shells to unoccupied states. In particular, by tuning the X-ray energy of the incident beam it monitors the absorption coefficient providing electronic and structural information on absorbing sites. In this way it is possible to investigate a specific atomic species and explore its local environment in different systems. Below, a brief description of how this technique can be used in the characterisation of semiconductor nanomaterials is reported. Further information can be found in literature.[12]

When a core electron absorbs energy equal to or greater than its binding energy, an edge is observed. In particular, when an X-ray photon has sufficient energy it is able to excite the core electron into the bottom of the conduction band (CB) via dipole transition. As the photon energy continues to increase by tuning it across the edge core electron excitation threshold, the core electron will continue to probe the unoccupied densities of states (DOSs) in the CB and above. Usually, X-ray absorption spectra are usually produced over the range of 200 – 35,000 eV and

edges are labeled according to the shell of the core electron originates from, *e.g*. K- and L- edges. In solids, the investigated transitions are sensitive to the chemical environment of the absorbing atom band structures resulting in a change in the atomic absorption coefficient. In particular, since the photoelectron in the final state has a finite lifetime, the shape of the absorbing spectra depends mainly on the geometrical structure of a finite cluster of atoms around the photo-absorber. The size of this cluster depends on the systems under study, ranging from a single shell to several shells.

X-ray Absorption Spectroscopy (XAS) generates a spectrum in which it is possible to identify three main regions. The dominant feature, the "rising edge", is generally known as XANES (X-ray Absorption Near-Edge Structure) or NEXAFS (Near-Edge X-ray Absorption Fine Structure). The region is at energies lower than the rising edge is called pre-edge while the EXAFS (Extended X-ray Absorption Fine Structure) region encompasses energies above the rising edge. The combination of XANES and EXAFS is referred to as XAFS. As a function of the photon energy above the rising edge, the absorption coefficient shows a somewhat pronounced oscillatory structure. This structure reflects the presence of neighbours around the absorbing atom and corresponds to the scattering of the ejected photoelectron off neighbouring atoms.

The dominant physical process is one where the absorbed photon ejects a core photoelectron from the absorbing atom, leaving behind a core hole. The atom with the core hole is now excited. The ejected photoelectron's energy will be equal to that of the absorbed photon minus the binding energy of the initial core state. The ejected photoelectron interacts with electrons in the surrounding non-excited atoms. If the ejected photoelectron is taken to have a wave-like nature and the surrounding atoms are described as scattering points, it is possible to imagine the backscattered electron waves interfering with the forward-propagating waves. The resulting interference pattern shows up in the measured absorption coefficient, causing the oscillation seen in the EXAFS spectra.

A.6.1 XANES spectra of $ZnGa_2O_4$

XAS and XEOL experiments at the O K-edge, Zn $L_{3,2}$-edge and Ga $L_{3,2}$-edge were performed on the High Resolution Spherical Grating Monochromator (SGM) 11ID-1 beam-line (energy: 250-2000 eV, $\Delta E/E: < 2x10^{-4}$) while analogous experiments at the Cr K-edge were performed on the Soft X-Ray Microcharacterization Beamline (SXRMB), 06B1-1 (energy: 1700-10000 eV, $\Delta E/E: < 4x10^{-4}$). All the experiments were carried out at the Canadian Light Source (CLS), University of Saskatchewan.

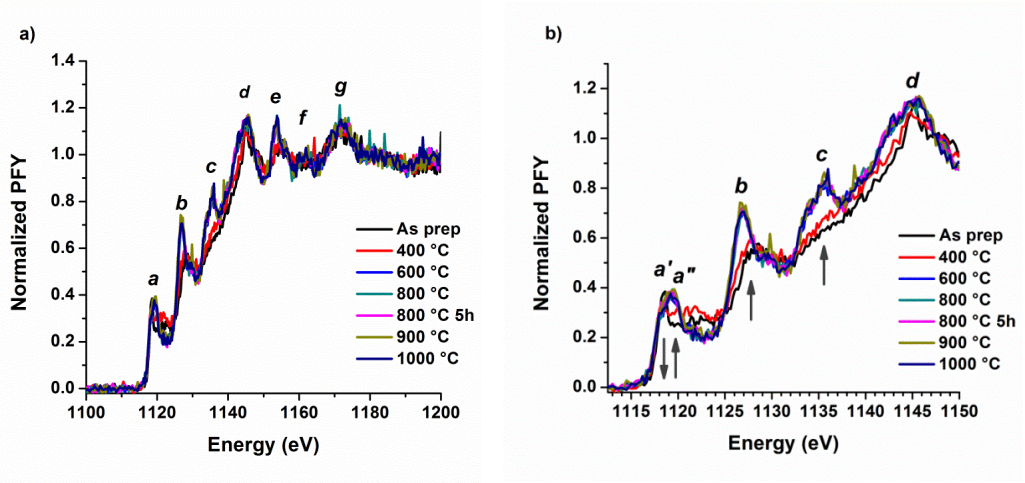

Fig. A.2 Effect of thermal treatments on PFY at Ga $L_{3,2}$-edge in $ZnGa_2O_4:Cr^{3+}$ samples: **a)** extended spectra, **b)** low energy spectra.

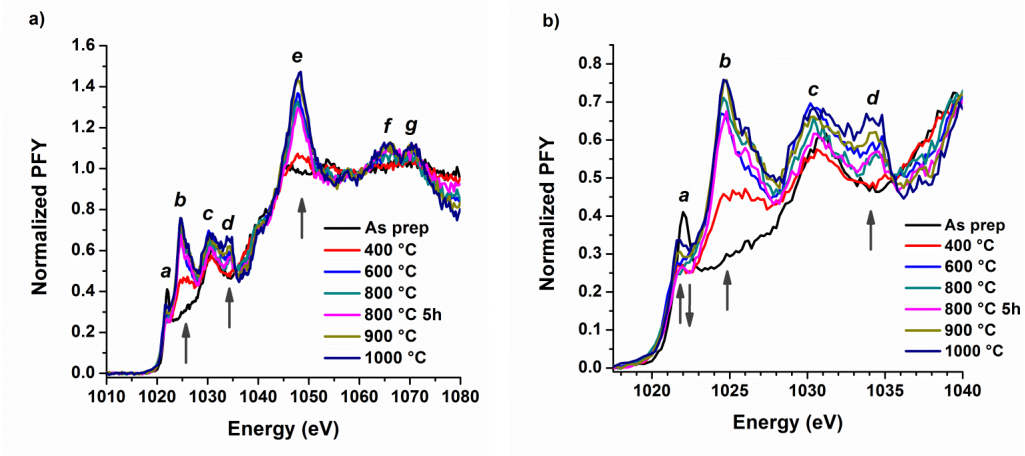

Fig. A.3 Effect of thermal treatments on PFY at the Zn $L_{3,2}$-edge in $ZnGa_2O_4:Cr^{3+}$ samples: **a)** extended spectra, **b)** low energy spectra.

A.7 References

(1) Schubert, U.; Hüsing, N. *Synthesis of Inorganic Materials*; Wiley, 2000.

(2) Livage, J.; Henry, M.; Sanchez, C. *Progress in Solid State Chemistry* **1988**, *18*, 259.

(3) Pierre, A. C.; Pajonk, G. M. *Chemical Reviews* **2002**, *102*, 4243.

(4) Corriu, R. J. P.; Leclercq, D. *Angewandte Chemie-International Edition in English* **1996**, *35*, 1420.

(5) Danks, A. E.; Hall, S. R.; Schnepp, Z. *Materials Horizons* **2016**, *3*, 91.

(6) Kittel, C. *Introduction to Solid State Physics*; 7th edition ed.; John Wiley & Sons, 1996.

(7) Klug, H. P.; Alexander, L. E. *X-ray Diffraction Procedures for Polycrystalline and Amorphous Materials* J. Wiley & Sons: Chichester UK, 1954.

(8) Moulder, J. F.; Stickle, W. F.; Sobol, P. E.; Bomben, K. D. *Handbook of X-Ray Photoelectron Spectroscopy*; Perkin Elmer Corporation Eden Prairies: MN, USA, 1992.

(9) Shirley, D. A. *Phys. Rev. B* **1972**, *5*, 4709.

(10) Briggs, D.; Seah, M. P. *Practical Surface Analysis*; Wiley and Sons: Chichester UK, 1983.

(11) Shirley, D. A. *Phys. Rev. B* **1972**, *5*, 4709.

(12) Mobilio, S.; Boscherini, F.; Meneghini, C. *Synchrotron Radiation - Basics, Methods and Applications*; Springer, 2015.

Acknowledgements

The following thesis contains material resulting from scientific collaborations with national and international groups. All scientist involved in such teamwork are gratefully acknowledged.

In particular, I would like to thank Dr. Marzio Rancan of ICMATE-CNR for XRD measurements and helpful discussion.

Dr. Simone Battiston and Dr. Monica Fabrizio of ICMATE-CNR performed SEM images and Dr. Roberta Saini of the University of Padova TGA analysis.

Adsorption and photodegradation experiments were performed in collaboration with Dr. Valentina Gombac and Prof. Paolo Fornasiero of the University of Trieste.

X-ray Absorption Spectroscopy (XAS) and X-ray Excited Optical Luminescence (XEOL) results arise from the international cooperation with Prof. Tsun-Kong Sham and Dr. Zhiqiang Wang from the University of Western Ontario London, Canada.

The study on luminescent antenna complexes was conducted by means of an intensive collaboration with Dr. Silvio Quici and Dr. Marco Cavazzini of ISTM-CNR, which performed the synthesis and NMR measurements. Dr. Roberta Seraglia of ICMATE-CNR contributed with mass spectrometry measurements.

I would like to express my deepest gratitude to Prof. Lidia Armelao and Dr. Gregorio Bottaro for their continous support and guidance throughout the research.